AcSIR

ACADEMY OF SCIENTIFIC AND INNOVATIVE RESEARCH

ATP Induced Conformational Flexibility in PcrA Helicase and Properties of Lipid Membrane in Presence of Nanoparticles and Surfaces: Molecular Simulations

by

Anil Ranu Mhashal

Registration Number: 10BB11J26124

Under the Guidance of

Dr. Sudip Roy

Dr. Rajnish Kumar

A thesis submitted in partial fulfillment for the
degree of Doctor of Philosophy

in the
Biological Sciences

CSIR-National Chemical Laboratory

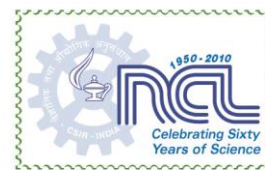August 2015

राष्ट्रीय रासायनिक प्रयोगशाला
(वैज्ञानिक तथा औद्योगिक अनुसंधान परिषद)
डॉ. होमी भाभा रोड, पुणे – 411 008. भारत

NATIONAL CHEMICAL LABORATORY
(Council of Scientific & Industrial Research)
Dr. Homi Bhabha Road, Pune - 411008. India

Certificate

This is to certify that the work incorporated in the Ph.D. thesis entitled **"ATP Induced Conformational Flexibility in PcrA Helicase and Properties of Lipid Membrane in Presence of Nanoparticles and Surfaces: Molecular Simulations"** submitted by Mr. Anil Ranu Mhashal to Academy of Scientific and Innovative Research (AcSIR) in fulfillment of the requirements for the award of the Degree of **DOCTOR OF PHILOSOPHY**, embodies original research work under our guidance. We further certify that this work has not been submitted to any other University or Institutions on part or full for the award of any degree or diploma. Research material obtained from other sources has been duly acknowledged in the thesis. Any text, illustration, table, etc., used in the thesis from other sources, have been cited and acknowledged.

Signed: _____

Anil Ranu Mhashal
(Research Fellow)
Physical and Materials Chemistry,
CSIR-National Chemical Laboratory, Pune
Date: 14/08/2015

Signed: _____

Dr. Sudip Roy
(Research Supervisor)
Physical and Materials Chemistry,
CSIR-National Chemical Laboratory, Pune
Date: 14/08/2015

Signed: _____

Dr. Rajnish Kumar
(Research Co-Supervisor)
Chemical Engineering and Process Development,
CSIR-National Chemical Laboratory, Pune
Date: 14/08/2015

". . . everything that is living can be understood in terms of the jiggling and wiggling of atoms."

Richard Feynman

ACADEMY OF SCIENTIFIC AND INNOVATIVE RESEARCH

Abstract

Biological Sciences

CSIR-National Chemical Laboratory

Doctor of Philosophy

by Anil Ranu Mhashal

In the present thesis, we have explored the properties of biomolecules, especially proteins and lipid membranes at the atomistic level using Molecular dynamics simulations. The thesis is mainly divided into two parts. Part A of the thesis focuses on understanding the mechanism of DNA unwinding by helicase while the part B of the thesis is on a lipid membrane interactions with nanoparticle and different surfaces.

In the part A of the thesis, we deal with enzyme PcrA helicase which is known to unwind the double stranded nucleic acid into its single stranded components. PcrA helicase breaks inter-strand base pairing using the energy released during the process of binding, hydrolysis and release of ATP. Therefore, understanding of ATP binding and unbinding from the active sites of the helicases is an important phenomena which can be related to their functionality in the process of unwinding of duplex DNA. In chapter 3, we have studied the unbinding of ATP from the active site of PcrA helicase and estimated the free energy for the transformation of helicase from the ATP bound state to the ATP free state. As a consequence of unbinding, the local conformational changes were observed amongst the protein residues which have been thoroughly analyzed in the same chapter. Further, in the thesis, chapter 4 highlights the global conformational changes of the protein domains after ATP unbinding by performing long run of all atomistic molecular dynamics simulations.

The part B of the thesis consist of the work on properties of lipid membrane under the influence of nanoparticles and surfaces. Chapters 5 and 6 of the thesis are focused on interaction of the lipid membrane with bare and passivated Gold nanoparticle while in chapter 7 investigates the interactions of self-assembled lipid membranes with model surfaces. In chapter 5 of the thesis, we emphasize on the interactions of different sized Gold nanoparticles with lipid membrane and have investigated the effect of perturbation on lipid membrane both locally and distantly from the nanoparticle adsorption site. We have elucidated how Gold nanoparticle induces deformation at the adsorption site and

affects the properties at a distant region from it. We have also shown that the hydrophilic Gold nanoparticle favorably interacts with the lipid headgroups and resides at the bilayer water interface. Therefore, further in chapter 6, we have estimated the free energy required to translocate the Gold nanoparticle from water to phase to the membrane. We have also investigated the effect of passivated nanoparticle on lipid membrane properties and the free energy required for permeation. The chapter 7 of the thesis deals with the interactions of solid surfaces with the lipid membrane. In this chapter, we have performed self-assembly simulations on flat solid hyrophilic and hydrophobic supports. This work also addresses the self-assembly mechanism of lipids on supports with varying strength of hydrophilicity and hydrophobicity and various parameters affecting lipid self-assembly. The properties of the self-assembled bilayers are also analyzed and reported in this chapter. Finally, we conclude the work in conclusion.

Acknowledgements

Research is a journey that combines various sciences together and the combination of whose yields a tool, to add those infinitesimal changes in the available knowledge domain to humankind, which result in betterment of human life or improvement in technology, or both. Towards the end of this long journey of small contribution of my research work in science through my doctoral studies, I hereby take opportunity to wish my sincere gratitude to all the members who have been part of it.

First of all, I would like to thank my adviser Dr. Sudip Roy for his patience, constant encouragement, and helpful guidance over the entire course. Apart from being an excellent teacher, he has been a great mentor. Thank you Sir, for considering each and every small idea that came into my mind and giving it a scientific approach that helped me learn and develop my research skills. Thank you for this unforgettable research experience.

I gratefully acknowledge members of my Doctoral Advisory Committee, Dr. Neelanjana Sengupta, Dr. Sarika Bhattacharyya and Dr. Anu Raghunathan for their guidance throughout the thesis work. Their suggestions were always enlightening on different aspects and helped me in improvements in my research work. I sincerely thank Dr. Rajnish Kumar for for his excellent Scientific Discussions and Encouragement over the course of time.

I acknowledge Dr. Sourav Pal, Director, NCL, for the availing the top class facilities for my research work.

Many thanks to Dr. Sangeeta Sawant, M. Sc. Project Guide, for patiently guiding me. It was her, who sowed the interest of research into me and directed me towards this excellent field to pursue my doctoral research.

I thank all my current and past lab-mates. Special thanks to Chandan Choudhury for exchanging his technical knowledge. Thank you Prithvi Raj Pandey, Swagata, Souvik, Sujit, Santu, Subhadeep, Nilesh, Pragati, Prajakta and Dr. Sheelan for keeping friendly environment in lab and improving my interest and efficiency of work. They have also been cheerful in technical and non-technical discussions during this course.

I would like to gratitude my other friends in NCL Campus: Shraddha, Avinash, Priyanka, Sucheta, Bharat, Dimpal and former member of NCL:Sucheta, for excellent coffee-session discussions. They all have been a good source of friendships as well as good advises and technical knowledge. I specially thank Nidhi for proof reading the thesis and Shubhada for improving my LaTeX skills, without which, this thesis writing wouldn't have been achieved flawlessly.

Contents

---

[1]This chapter is adapted from the publication Mhashal AR, Choudhury CK and Roy S (2015) Probing the ATP-induced conformational flexibility of the PcrA helicase protein using molecular dynamics simulation. Journal of Molecular Modeling (2016) DOI 10.1007/s00894-016-2922-3

List of Figures

List of Tables

Symbols

C_N	characteristic ratio
$C(t)$	correlation function at time t
D	diffusion coefficient
E	total energy
E_a	activation energy
F	free energy
$\boldsymbol{F}_i$	force on particle i
G	Gibbs free energy
k_B	Boltzmann's constant
k	force constant
K	kinetic energy
m_i	mass of particle i
M	molecular weight
N	number of particles
N_f	degrees of freedom
P	linear momentum
$\mathcal{P}$	instantaneous or microscopic pressure
P	macroscopic pressure
$P(q)$	Boltzmann distribution
$\boldsymbol{r}_i$	position vector of particle i
r	bond length
R	hydrodynamic radius
R	end-to-end distance
R_g	radius of gyration
S	entropy

T	temperature
$T(t)$	instantaneous temperature
T_g	glass transition temperature
T_m	melting temperature
t	time
δt	Molecular Dynamics time step
U	internal energy
$V(r)$	pair potential
V	volume
$\boldsymbol{v}$	velocity
Z	partition function
β	$\frac{1}{k_B T}$
γ	surface tension
η	viscosity
θ	angle
κ	isothermal compressibility
λ	velocity scaling factor
ν	polymer scaling coefficient
ρ	density
$\sigma_{\mathcal{A}}^2$	variance in dynamical variable $\mathcal{A}$
τ	temperature coupling parameter
τ_s	slow relaxation time
τ_f	fast relaxation time
ϕ	torsional angle
Ω	states available to the system
$\langle \cdots \rangle$	ensemble average
$\mathcal{O}(x^n)$	terms of order x^n or smaller

Dedicated to my parents. . .

Chapter 1

Introduction

The basic structural, functional, and biological unit of living organisms is cell. It functions with assistance of specialized units of bio-molecules consisting of proteins, lipids, and carbohydrates. Proteins involved in several cellular activities such as catalyzing the metabolic reactions, stimuli responses etc. Lipids are the major constituents of the cell membrane which acts as a selective barrier for the extra/intra cellular material, while carbohydrates serves as a source of energy and also as part of the nucleic acid.

Enzymes are the class of proteins that plays a crucial role as catalyst to control the rate of biochemical reactions. These are globular proteins with a specialized three dimensional structure designed to perform a specific function. In biochemical reactions, enzymes structurally modifying the micro-environment of substrate molecules and lowering the activation energy which trigger the reaction. However, there is considerable lack of understanding of the functional mechanism of enzymes. Based on the structure-function relationship, it is the structure that determines the function of the protein. In simple terms, structural changes cause the protein to function *i.e.* myosine, actine, F1 ATPase [1]. Therefore, it is crucial to envisage the structural and molecular details of such proteins. A perspective of these bio-molecules at the atomic level is crucial in understanding the nature of enzymatic reactions. Hence, in this thesis we have elucidated the properties of these proteins in the atomistic time and length scales to understand about the enzymes and their mode of action.

Lipid membranes are considered as a biologically relevant models to study nanomaterial-cell interactions as it is the first contact, nanoparticles (NP) have with any living organism. Understanding the interaction between NP and cell membrane has a two-fold importance in terms of the evaluation of designing therapeutic agents as well as a means of reducing NP toxicity. The membrane-NP interactions have widely been studied over the past few decades [2–10]. However, there is still a lack of knowledge about the influence of

NPs on physicochemical properties of lipid membranes. Hence, in this thesis, we have investigated the properties of the lipid membrane under the influence of nanomaterials.

To accommodate the protein and lipid membrane systems, the thesis is divided into two parts. Part A of the thesis, discusses the studies relating to the enzyme mechanism. Part B of thesis elucidates the properties of lipid membranes under the influence of NP and surface.

Part A

This part of the thesis focuses on the unwinding mechanism of DNA by enzyme helicase. DNA unwinding is a very essential process that unwinds duplex DNA to make single stranded nucleic acid available for replication, translation or repair. DNA helicases are the ubiquitous motor proteins are known to unwind the duplex DNA to yield the transient single stranded component utilizing free energy from ATP hydrolysis [11–15]. Different types of helicases have been investigated both experimentally and theoretically to understand the unwinding mechanism of DNA assisted by these enzymes. Previous studies reported that many helicases function as either hexamers, dimers [11] or monomers [16–18]. The monomeric plasmid reduced copy (PcrA) helicase from *bacillus stearothermophilus* is known to be best suitable model for understanding the helicase mechanism. It is single stranded DNA (ssDNA) translocase with helicase and ATPase activity [19, 20]. Reports in the literature elucidate the progressive translocation of PcrA protein on the double stranded region of DNA, which breaks the inter-strand hydrogen bonds with the rate of 50 nucleotide/sec [21]. This process destabilizes the DNA duplex, converting it into ssDNA. It is known that PcrA helicase utilizes the free energy from ATP hydrolysis for translocation over the DNA [22, 23]. At the structural level, the translocation of these protein motors is governed mainly by the change of conformation of protein which occurs because of ATP binding and hydrolysis. Previous studies have shown that these conformational changes are the key factors in the process of DNA unwinding by helicase [16, 22–24]. The well accepted inchworm model for PcrA helicase explains the series of events that occurs during the unwinding of DNA. It involves the binding of PcrA protein to ssDNA nick of the dsDNA followed by ATP binding to the enzyme active site [23]. The ATP binding causes proteins to undergo the compact closed substrate state which is followed by the hydrolysis of ATP. The free energy released after the hydrolysis is utilized in the conversion of closed domain state to structurally wider domain product state conformation which allows helicase translocation [25, 26].

Inchworm model suggests that binding and the hydrolysis of the ATP are crucial events for the protein to be functionally active [23, 25, 26]. Therefore, in this thesis we emphasized on one of the crucial event of ATP unbinding from the catalytic site and studied its effect on the protein conformations. We also have computed the free energy required for the

ATP binding to the catalytic site. We have also studied the effect of unbinding on the local conformational flexibility at residue level. We have also investigated the effects of ATP on global conformational flexibility of the ATP bound and ATP free protein.

Part B

The second part of the thesis elucidates the properties of lipid membranes in the presence of NPs and surfaces. The lipid membrane is a semi-permeable cell wall which allows selective of the ions and molecules in the cell. It surrounds the cytoplasm of a cell and separates the interior of the cell from the extracellular environment. The cell membranes are primarily composed of the lipids with proteins embedded in them. Lipids are the amphiphilic molecules with hydrophlic headgroups and hydrophobic tails of hydrocarbon chains arranged spontaneously to form lipid bilayer. These lipid bilayers have attracted a great deal of interest to researchers as a model object for studying the cell membrane properties. In recent years, it has acquired attention due to its importance in the areas of biological and pharmaceutical research [27–29], such as signaling and transport of molecules, drug discovery and delivery. The cell membranes have been extensively studied for many decades, both experimentally and theoretically [30–34]. The investigations have provided an extensive amount of information about the intriguing physicochemical aspects of membrane systems. However, the interaction of membrane with foreign materials has not yet been explored and properly understood. Therefore, this part of the thesis is dedicated to the investigation of the properties of the lipid membrane under the influence of the NP and surfaces. Several practical concerns have attracted the attentions to the problem of NP and cell membrane interactions. The toxic and beneficial effects of the NPs have been studied extensively as living bodies are often exposed to NPs [2–10]. NPs are widely being used in biotechnology, biomedical and pharmaceutical science [35, 36]. Their promising applications as bio-medicines such as drug and gene delivery vectors have attracted lots of attention. Gold NPs are widely used as drug-gene delivery agents, medical diagnostics and therapeutic agents [37–42]. The engineered NPs has been successfully proven to be a potential agent for targeting the cancer cells [43–46]. However, despite of their huge benefits, it is important to assess the potential risks associated with the NPs. The possible environmental and biological fate and toxic effects of the NP should be addressed. A number of reports are available in the literature overviewing the NP toxicity, still very little work has been conducted in this area so far [47–49]. The NPs emitted from various sources, e.g. automobiles, industrial processes and even cosmetics that imposes very serious health concerns because of their detrimental effect on living organisms. For example, the carbon NPs emitted into atmosphere from the combustion, can cause serious health damage. These NPs get absorbed through the process of respiration and deposits on the epithelial cells in the lungs which triggers a number of responses.

NPs are highly effective to penetrate the cell membrane which affects the cellular activities within the cell. Their mode of penetration is mainly through internalization mechanisms like physical rupturing, membrane mediated transport, pore formation. Common to all these routes of cell entry is the initial NP-membrane interaction. However the link between the NP membrane interaction and translocation in the cell is not yet understood. Lipid bilayers are considered to be biologically relevant models to study nanomaterial-cell interactions. The understanding of interaction between them is important in terms of nanosafety and the effectiveness of NPs in biomedicinal applications as well. Available studies highlight the role of physical and chemical properties of NPs and its effect on their interactions with lipid membrane. Properties of NP include size, shape, chemical composition, surface charge, morphology and surface coatings. For example, NP size can affect the specificity of uptake in cells, with potential to induce cellular responses [50–52]. The shape of a NP is equally crucial. Recent studies have investigated the effect of NP geometry on the transfer of NP across the membrane [53, 54]. The relationship between the NP shape and their translocation rate across the membrane as shown by Nangia *et al.* [53]. It has been observed that negatively charged NPs induce local gelation fluid bilayer whereas NPs of positive charge fluidize the lipid membrane locally [55]. NPs have also been used with the surface modifications with ligands attached to the NP surface for efficient transportation across the lipid membrane [56–58]. It has been observed that surface composition such as hydrophobic/hydrophilic surface patterning enhances the permeation of NPs [59]. The free energy profiles of carbon based NPs with different morphology [60] have also been investigated which suggest that the surface morphology of the NP plays an essential role in its permeation [56, 57, 61, 62].

Endocytosis and direct penetration (diffusion) are two main ways by which NPs pass through membranes [54, 56, 63]. Large particles of diameter varying from 10 ns to 100 ns usually cross the membrane by endocytosis. However, smaller particles of several nanometers or even smaller, penetrate the membrane via diffusion. The process of NP penetration by endocytosis can be divided into three parts: [64–66] adsorption of particles to the membrane, membrane wrapping, and finally the pinch-off (particlelipid complex detaching from the membrane). It has been observed that, NPs, when interact with lipid membrane, induces the perturbation at the adsorption site [55]. It causes the maximum perturbation by deforming the local lipids in contact with NP. However, part of lipid membrane away from the adsorption site is also expected to be getting perturbed. The properties of the lipid membrane far from the NP adsorption site are still poorly understood. Therefore, in the present thesis, we focus on the investigation of structural and dynamical properties of the lipids membrane both locally and at a distant region from the NP adsorption site to understand the effect of NP on lipid membrane. The

study also highlights the perturbation effect of different sized NPs on the lipid membrane at a various regions of the lipid membrane.

Since nanometer-sized particles (NPs) are capable of crossing cellular barriers can migrate into circulation, and therefore, attention is given to factors that influence the permeation process. NPs cannot cross the membrane on their own hence adding an external force on NP is required for their penetration [54, 63, 67–69]. Some of the commonly used approaches such as direct microinjection [70, 71], electroporation [72] and conjugation of natural cell-penetrating/-fusogenic chaperons to nanomaterials [73] are used in the transportation of the nanomaterials into the cell. Moreover, NPs are also functionalized with ligands like polyethelene-glycol (PEG), 11-mercapto-1-undecanesulphonate (MUS), tri-octyl-phosphene-oxide (TOPO) or octane-thiol (OT) to improve the penetration [56–58, 74–77]. NP surface properties such as hydrophilicity or hydrophobicity are also crucial in penetration as it can guide the location of the NPs on the surface or within a specific compartment of the vesicle [78, 79]. Several recent simulation studies focused specifically on the effect of hydrophobic and hydrophilic patterns on the ability of a nanoscale object to translocate through a lipid membrane. Scientists have investigated NPs designed with striped and random distribution of hydrophilic and hydrophobic groups [59, 80, 81]. They have found that the striped NPs experience a significantly lower free-energy barrier compared with the NP with a random distribution of hydrophilic and hydrophobic ligands [59]. Recent studies have reported the minimum driving force required for the penetration of different shaped NPs and estimated their penetrating capability [54]. During the penetration, NPs have to overcome a hydrophobic barrier in the membrane that is always present in biological systems. Therefore, one could target to reduce free energy barriers of NP permeation for their efficient transfer across the cell membrane. It is known that the NPs coated with suitable ligand molecules can be responsible for important properties such as cell membrane penetration free energy [59, 79, 81].

Gold nanoparticles (AuNPs) coated with a self-assembled monolayer of thiolated molecules, have multiple potential applications, such as sensing, catalysis, drug delivery and molecular recognition [37, 38, 81–84]. Experiments and theoretical calculations showed that amphiphilic AuNPs protected with a binary mixture of alkanethiol ligands were able to insert into and fuse with the hydrophobic core of lipid vesicles and suspended lipid bilayers [85, 86]. The interactions between monolayer-protected AuNPs and lipid bilayers have been a subject of investigation aimed to elicit the role of surface charge, ligand composition and particle size among other tuning parameters on nanobio interactions [5, 53, 79, 87–92]. Thus, the work in thesis emphasizes on the investigation of the free energy associated to the permeation of bare AuNP and alkane-thiol capped AuNP through the lipid membrane. The findings can be useful in designing more NPs. The

energies will guide whether a NP will cross the membrane energetically favorable to cross the membrane to reach the target.

Further, in the lipid section(Part B), we have investigated the supported lipid bilayers (SLBs). Experiments dealing with the cell membrane are oftenly carried out with the SLB. These bilayers provide an excellent model system for studying the cell membranes [93–95] with potential bio-technological and pharmaceutical applications [27–29]. SLBs are accessible to a wide variety of surface-specific analytical techniques [95–98]. Thus, it makes possible to investigate processes such as cell signaling, ligand - receptor interactions, enzymatic reactions occurring at the cell surface [99–102]. A large number of systems have been investigated, including solid-supported lipid bilayers [103–107], polymer-cushioned lipid bilayers [108–110], hybrid bilayers, [111, 112], tethered lipid bilayers [113], suspended lipid bilayers [114, 115], or supported vesicular [116, 117] layers.

The supported lipid bilayers are constructed on the solid substrate like silica based substrates (e.g. glass, aerogel and xerogels) [27, 118–120]. Langumuir-Blodgett [121, 122] and the vesicle fusion [123] are the most commonly used methods to construct the SLB. Although, it is a the excellent cell membrane model, SLB compromises many of the important properties of the membrane. It has been reported that, despite the existence of the water layer between the solid hydrophilic support and bilayer, the structure and the properties of the bilayer are affected by the physical and chemical properties of the solid substrates. Recent studies reported the effect of substrate on the properties of the supported bilayers, e.g. decoupled phase transition [54, 124–126], asymmetric molecular distribution between upper and lower leaflet of SLB, structural and dynamical heterogeneity in the leaflets [127–129]. It is difficult to control the bilayer membranes with functional substrate membrane systems on solid devices as the lipids and the proteins are more prone to get denatured. Therefore, it is important to understand the interaction between solid substrates and lipid bilayers to obtain the stable cell membrane with all the properties of bilayer intact.

Apart from the conventional methods, self-assembly of the lipids on the substrate can produce the SLB, which may be the alternative approach to construct the supported lipid bilayer. It requires proper understanding of the complex self-assembly process and lipid substrate interactions under the influence of external perturbation (i.e. substrate). The structure of the lipid assembly depends upon the nature of the material used as a substrate. The studies reported that hydrophobic carbon nanotube causes formation of the cylindrical micelle, where hydrophobic carbon NPs induces the adsorption of lipids in monolayer fashion. However, lipids maintain the bilayer (head-tail-tail-head) morphology when suspended over the hydrophilic supports. Hence, it is expected that the self-assembly of the lipids may vary depending upon the substrates used. Therefore, the

part of the thesis is dedicated to envisage the process of lipid self-assembly on different flat hydrophilic and hydrophobic support and the properties of the self-assembled lipid bilayer. The work mainly contributes to finding the best optimal support which can least affect the bilayer properties.

Molecular dynamics (MD) simulation is a useful tool to predict and understand experimental observables at the molecular level. It serves as a complement to the experiments and enables us to obtain microscopic molecular level details with reasonable accuracy. MD simulations act as a bridge between microscopic length-time scale and the macroscopic laboratory world. Nowadays, MD simulation is widely being used in understanding complex problems like protein folding, polymer dynamics, enzyme-substrate binding etc. Over the last two decades, molecular dynamics (MD) simulations have become one of the important tools to tackle many of the complex problems due to the highly efficient computers and simulation algorithms. MD simulations are now routinely used to understand structural and dynamical properties of soft materials ranging from polymer to bio-molecules.

In the present thesis (part A), we have employed MD simulations to understand the unwinding mechanism of DNA assisted by helicase. We have simulated the process of ATP unbinding from active and its effect on the catalytic site residues of enzyme PcrA helicase. The study also reports the binding free energy of the ATP to the active site. Steered molecular dynamics simulation is used to generate the configurations around a reaction coordinate and umbrella sampling simulation was used to calculate the free energy of the process. The enzyme was further studied for its structural flexibility by performing long run MD simulations.

In the part B, we have employed MD simulation on lipid bilayers which is used as a model to represent the cell membrane. This part mainly focuses on the interaction of lipid membrane with nanopartcles and surfaces. We have investigated the interaction of different sized nanopartcles on the lipid membrane. From simulation studies, we have examined the physicochemical properties of the lipid membrane under the influence of NPs. It is known that the NP can deform the membrane most on adsorption site whereas the effect of perturbation away from the adsorption site is still unknown. Therefore, in this work, we have investigated the perturbation effect locally as well as far away from the nanopartcle adsorption site. This work is continued by modifying the surface of NPs with a certain ligands. We have calculated the free energy required to cross the lipid membrane for above bare and surface modified NP.

Apart from lipid NP interactions, we have also studied the lipid bilayer formation on a solid surface. Lipid self-assembly over the solid substrate can be one of the approaches to construct the supported bilayers. The influence of external perturbation in the process

of self-assembly and the interactions between the lipids and support were studied in the final working chapter of the thesis. In this chapter, we have also studied the properties of the lipid bilayer on hydrophobic and hydrophilic surfaces.

The layout of the thesis is as follows.

In chapter 2, computational procedures are discussed in brief.

Part A,

In chapter 3, ATP unbinding free energy and the conformational flexibility of residues is discussed.

In chapter 4, conformational flexibility of protein domains is discussed.

Part B,

In chapter 5, Effect of AuNP on the fluidity of lipid membrane is discussed.

In chapter 6, permeation free energy of bare and capped AuNP is discussed.

In chapter 7, self-assembly of the phospholipids on the flat support is discussed.

In chapter 8, conclusions from above studies are discussed.

Chapter 2

Computational Methods

Molecular modelling spans over a wide range of fields from computational chemistry, drug design, computational biology and materials science for studying molecular systems ranging from small chemical systems to large biological molecules and material assemblies. It provides the atomistic level description of the molecular systems that can be used to model or mimic the behavior of molecules. The objective of these techniques is to predict and understand the experimental observable at the microscopic level. It may range from the more detailed and accurate electronic level to the atomistic, coarse grained level, mesoscale or macroscopic continuum level.

The properties of soft matter systems are determined by processes and interactions occurring over a wide range of length and time scales. Therefore, various simulation methods at various levels of time and length scale are developed in order to understand the properties of soft matter that are determined by a wide range of scales [130, 131]. Quantum mechanical methods solve Schrodingers equation for all of the subatomic particles in a system and is used to address electronic/energetic properties at a high-resolution microscopic level. However, the methos is limited to short length and time scales. In the classical mechanics, atoms are treated as classical particles connected via elastic sticks corresponding to bonds and the laws of classical mechanics which define the dynamics of the system. The classical all atom simulations can reach upto nanometer length and few microsecond time scales based on the computer hardware and simulation algorithms used in last two decades. The particle-based coarse grained approaches are capable of sampling microscopic to mesoscopic scales. Especially these methods are also able to access large conformational fluctuations, yet still fail to cover many macroscopic phenomena. To achieve this, one needs to go beyond (purely) particle based approaches and use the methods like Lattice Boltzmann [132] or DPD [133, 134] or other mesoscopic methods to include hydrodynamic effects such as continuum modeling.

In the present thesis, the protein simulations are performed with all atomistic MD simulations and the properties such as conformational flexibility of protein and the active site residues are studied. The interactions of nanoparticle with the lipid membrane are also investigated in the chapter 5 and 6 all atomistically. In chapter 7 of the thesis, we have employed coarse grained MD simulation to achieve the self-assembly of the lipid which is otherwise difficult using all atom model.

2.1 Classical all atom molecular dynamics

In the present study, we employed all atomistic classical molecular dynamics simulation in order to achieve the desired microscopic/macroscopic properties of the systems. The term classical refers to the use of Newtonian mechanics to define the physical basis of the model. The Newton's equation of motion for N interacting particles is given as below,

$$m_i \frac{\partial^2 r_i}{\partial t^2} = F_i, i = 1..N \tag{2.1}$$

where m_i and r_i represents the mass and the position of a particle and t is the time. The force (F_i) exerted on the particle is expressed as a negative gradient of potential energy from all the interacting particles in the system.

$$F_i = -\frac{\partial V(r_1, r_2, ..., r_N)}{\partial r_i} \tag{2.2}$$

The potential energy (V) between the particles is defined as a function of their positions r_i. For each timestep of the MD simulation these equations are solved and the particles are propagated in an appropriate ensemble coupled with thermostats and barostat. MD simulation generates a series of configurations with position and velocity of each particle written to an output file which is referred as trajectory. The trajectory can be used to visualize the evolution of the system as a function of simulation time, calculating the properties to compare with the experiments and also to compute the numbers which are not available experimentally.

MD simulation consists of three essential inputs such as coordinates, forcefield and simulation parameters. The coordinates are the set of the numbers to determine the position of every atom in a space which are derived from the experimental techniques such as X-ray crystallography or NMR etc. These model structures are deposited in the repositories such as protein data bank (PDB), PubChem and Chemspider etc. which serve as a starting structures for the simulation. These starting structure need to be energy minimized to bring them to the minima at the potential energy surface otherwise

the simulation may fail. The initial structure after solvation might have inappropriate geometry or steric clashes therefore it needs to be removed first to relax the structure. Steepest descent and conjugate gradient are the commonly used algorithms for energy minimization.

The *force fields* are the set of paramaters and the potential energy functions that defines the inter-actomic potentials. The parameter sets are empirical and consist of various information about the chemical model such as different types of atoms, chemical bonds, dihedral angles and so on. The force field defines connectivity between the atoms in molecule depending upon the inter-atomic potentials. The inte-ratomic potentials are of two types, bonded potentials and non-bonded potentials. Further the bonded interactions are divided into bond length, bond angle and dihedral while non-bonded interaction terms are taken care by Lennard Jones and Coulomb. The energy functions in MD simulation are expressed as,

$$V = V_{bonded} + V_{nonbonded}$$

$$V_{bonded} = \sum_{bonds} \frac{1}{2} K_b (b - b_0)^2 + \sum_{angles} \frac{1}{2} K_\theta (\theta - \theta_0)^2 + \sum_{dihedrals} K_\phi (1 + cos(n\phi - \lambda))$$

$$V_{nonbonded} = \sum_{LJ} 4\epsilon_{ij} \left[\left(\frac{\sigma_{ij}}{r_{ij}} \right)^{12} - \left(\frac{\sigma_{ij}}{r_{ij}} \right)^6 \right] + \sum_{coulomb} \frac{q_i q_j}{4\pi\epsilon_o r_{ij}}$$

(2.3)

The bonds and angles are commonly treated with the hormonic potentials, however cosine periodic functions are used in case of the dihedral angles. K_b, K_θ and K_ϕ represents the bond, angle and dihedral angle force constants and values b, θ and ϕ are the values at time t deviating from equilibrium values b_0, θ_0 and ϕ_0. The dihedral potential function is defined with multiplicity n and phase λ. However, improper dihedrals are used to maintain the planar geometry of the planar molecules (*e.g.* aromatic rings) or sometimes to avoid the flipping at the chiral centers in a molecule. The nonbonded interactions have three terms which include a repulsion , dispersion and a Coulomb term. The repulsion $(-\frac{1}{r^{12}})$ and dispersion $(-\frac{1}{r^6})$ between particle i and j term can be taken care with Lennard-Jones. The ϵ_{ij} signifies negative well depth and a steep repulsive wall at a distance r $< \sigma_{ij}$. However, charged contributions are computed from the Coulomic term where q_i and q_j are the charges on the corresponding particle separated by distance r_{ij}.

In terms of bonded interactions, values of bond, angle and dihedral constants, and the corresponding equilibrium values are available in a force field, and hence are input to MD simulation. Similarly, for nonbonded interactions such as σ_{ij}, ϵ_{ij}, and charges for all the particles are provided as input to MD simulations. All the parameters available in a force

field (also called force field parameters), are calculated empirically. The tedious process of force field development involves calculation of these empirical force field parameters. Commonly used force fields are OPLS [135, 136], AMBER [137], CHARMM [138, 139], and GROMOS [140]. They include force field parameters for different class of complex chemical moieties.

Along with with starting structure and force field, a set of instruction or parameters are needed to run the simulation. The MD simulation algorithm involves successive calculation of force at each timestep followed numerically solving Newtons equations of motion. However, for the initiation of the MD simulation position and the velocities are always needed. The initial velocities for every atom are generated from Maxwell-Boltzmann velocity distribution by following equation,

$$p(v_i) = \sqrt{\frac{m_i}{2\pi kT}} exp\left(- \frac{m_i v_i^2}{2kT} \right) \tag{2.4}$$

where k is Boltzmanns constant. It computes a distribution of velocities generated from random numbers. However, all velocities are scaled so that the total energy corresponds exactly to T (input parameter).

In MD simulation the forces are used to integrate Newtons equations of motion, and hence propagate the particles in the system. Among many integration algorithms available leaf-frog algorithm [141] is commonly used. It updates the positions and velocities using the forces at time t according to the following relations

$$v(t + \frac{1}{2}\Delta t) = v(t - \frac{1}{2}\Delta t) + \frac{\Delta t}{m}F(t)$$
$$r(t + \Delta t) = rt + \delta t v(t + \frac{1}{2}\Delta t) \tag{2.5}$$
$$r(t + \Delta t) = 2rt - r(t - \Delta t) + \frac{1}{m}F(t)\Delta^2 + O(\Delta t^4)$$

The Δt is the timestep chosen to integrate the Newton's equation of motion. Timestep is generally used as 1 fs, while in some case 2 fs also used to enhance the performance in simulation time by keeping bond vibration constant. Such bond constraints are incorporated in MD simulation using LINCS [142] or SHAKE [143] algorithms.

Calculation of the nonbonded terms is the most time consuming part of MD simulation. It is pair additive. Hence, in principle, the energy between every pair of atoms is computed so that the number of steps increases as the square of the number of atoms (N^2). Therefore, to speed up the computation, a cut-off radius is defined separately for LJ and Coulombs interactions and the calculation of the non-bonded energies beyond this

distance cut-off are ignored. The LJ interactions are truncated using a shift and switch function which sets the interaction potentials to zero after the cut-off distance [144]. The long range electrostatic interactions are important in terms biomolecular process hence, they must be modeled accurately. However, as we use larger cut-offs to treat a long range Coulombic interactions, the computational cost will dramatically increase. Therefore, such interactions are treated with the reation field, Ewald sum, or particle mesh Ewald method. In reaction field the electrostatics are taken care with a uniform dielectric constant beyond the short-range cutoff value. Ewald sum [145] method computes the long-range interactions in an infinitely periodic systems and summation of interaction energies (long range) is done in fourier space.The periodicity is taken care of by the periodic boundary conditions.

In PME [145, 146], direct summation method of the Ewald summation method is replaced by summation over point particles (particle part of PME). Ewald summation takes advantage and reduces the complexity and scales up to $N^{\frac{3}{2}}$, though impractical while dealing with larger biological systems. PME is a faster algorithm that uses fast fourier transform to bring down the complexity to NlogN and thus substantially reduces the computational time needed. However, the speed and accuracy depends on the mesh size, interpolation scheme etc.

The thermodynamic ensembles are essential in order to obtain the desired properties out of the system. Microcanonical (NVE) ensemble can be used if the total number of atoms N and the volume V(of the unit cell) are kept constant along with the energy (E). However, one can chose the canonical ensemble to maintain the number of atoms (N), volume (V) and temperatute (T) of the system constant. The temperatute of the system is kept constant by coupling of the system with the thermostat. Most commonly used thermostats are V-rescale, Berendsen and Nose-Hoover. Isothermal-Isobaric (NPT) ensemble is used to maintain the constant pressure in the system. Berendsen and Parrinello-Rahman barostat are used to keep maintain the system pressure constant.

With these inputs molecular dynamics algorithm integration of the equations of motion for each timestep (given as input) for a desired simulation time (calculated as $\Delta \times$ number of steps) then yields a trajectory that describes the positions, velocities and accelerations of the particles as they vary with time. In the present thesis, all the simulations are performed using Gromacs simulation suit [147–149]. Gromacs is a fast and flexible parallel code to perform MD simulations. The analyses reported in the thesis are obtained using the Gromacs analysis tools however, we also have written some codes for special cases. Details of such analysis codes are provided as they appear in the different chapters.

2.2 Free energy calculation

In a molecular dynamics simulation, one often wishes to explore the macroscopic properties of a system through microscopic simulations such as calculation of solvation free energy, binding free energy of a particular drug, or to examine the energetics and mechanisms of conformational change. There are several free energy calculation methods based on MD simulation are available, such as MM-PBSA [150], thermodynamic integration [151], free energy perturbation [152] and umbrella sampling [153–155] which can calculate the free energy of the system.

The umbrella sampling, biased MD simulation, is the one of the efficiently used technique to calculate the free energy of the system changing from one thermodynamic state to another (e.g. reactant and product) as a function of the reaction coordinate. This method involves simulation of systems with a biasing umbrella potential to reach the conformational phase space which is not possible with the conventional MD simulation. The sampling windows along the reaction coordinate are generated and simulated independently. The sampled distribution of the system along the reaction coordinate are used to calculate the free energy change in each window and then combined together to generate the continuous smooth energy profile.

The bias potential w_i of window i is an additional energy term, which depends only on the reaction coordinate.

$$E^b(r) = E^u(r) + w_i(\xi) \tag{2.6}$$

The term E^b, $E^u(r)$ and $w_i(\xi)$ are the biased, unbiased energy functions and umbrella potential added to the system respectively.

The free energy is related to the probability distribution of the system along given reaction coordinate . In umbrella sampling, the distribution of the system along given reaction coordinate is calculated with probability distribution function.

Assuming the ergodic system, the probability distribution biased system along a reaction coordinate P_i^b can be computed as,

$$P_i^b(\xi) = \frac{\int exp[-\beta[E(r) + w_i(\xi'(r))]]\delta[\xi'(r) - \xi]d^N r}{\int exp[-\beta E(r) + w_i(\xi'(r))]d^N r} \tag{2.7}$$

The unbiased free energy $A_i(\xi)$ can be obtained from the unbiased distribution,

$$P_i^u(\xi) = \frac{\int exp[-\beta E(r)]\delta[\xi'(r) - \xi]d^N r}{\int exp[-\beta E(r)]d^N r} \tag{2.8}$$

As the bias depends only on ξ and the integration in the enumerator is performed over all degrees of freedom but ξ,

$$P_i^b(\xi) = exp[-\beta w_i(\xi)] \times \frac{\int exp[-\beta E(r)]\delta[\xi'(r) - \xi]d^N r}{\int exp[-\beta[E(r) + w_i(\xi'(r))]]d^N r} \tag{2.9}$$

$$\begin{aligned} P_i^u(\xi) &= P_i^b(\xi) \, exp[\beta w_i(\xi)] \times \frac{\int exp[-\beta[E(r) + w_i(\xi(r))]]d^N r}{\int exp[-\beta E(r)]d^N r} \\ &= P_i^b(\xi) \, exp[\beta w_i(\xi)] \times \frac{\int exp[-\beta[E(r)]exp[-\beta w_i[\xi(\overrightarrow{r})]]d^N r}{\int exp[-\beta E(r)]d^N r} \\ &= P_i^b(\xi) \, exp[\beta w_i(\xi)] \, \langle exp[-\beta w_i(\xi)]\rangle \end{aligned} \tag{2.10}$$

Using Eq. (2.10), $A_i(\xi)$ can be evaluated. As $P_i^b(\xi)$ is obtained from an MD simulation of the biased system, $w_i(\xi)$ is given analytically, and $F_i = -\frac{1}{\beta}ln\langle exp[-\beta w_i(\xi)]\rangle$ is independent of ξ which is a constant,

$$A_i(\xi) = -(\frac{1}{\beta}) \ln P_i^b(\xi) - w_i(\xi) + F_i \tag{2.11}$$

Therefore, by this way, the free energy $A_i(\xi)$ for every sampling window is calculated. However, the free-energy curves $A_i(\xi)$ of more windows are needed to be combined together to get one global $A(\xi)$. Therefore, the Fi have to be calculated as they are associated with the bias potential and connect the free-energy curves $A_i(\xi)$ obtained in the different windows:

The F_i can be calculated as,

$$\begin{aligned} exp(-\beta F_i) &= \langle exp(-\beta w_i(\xi))\rangle \\ &= \int P^u exp[-\beta w_i(\xi)]d\xi \\ &= \int exp[-\beta[A(\xi) + w_i(\xi)]]d\xi \end{aligned} \tag{2.12}$$

with $P^u(\xi)$ being the global unbiased distribution. The F_i cannot directly be obtained from sampling. It can be done with the weighted histogram analysis method.

2.2.1 Weighted histogram analysis method

This method is used to calculate the global distribution by weighted average of distribution obtained from the individual sampling windows. It aims to minimize the statistical error of $P^u(\xi)$.

$$P^u = \sum_i^{windows} p_i(\xi)P_i^u(\xi) \tag{2.13}$$

The weights p_i are chosen in order to minimize the statistical error of P^u:

$$\frac{\partial \sigma^2(P^u)}{\partial p_i} = 0 \tag{2.14}$$

under the condition $\sum p_i = 1$. This leads to

$$p_i = \frac{a_i}{\sum_j a_j}, a_i(\xi) = N_i exp[-\beta w_i(\xi) + \beta F_i] \tag{2.15}$$

where N_i is the total number of steps sampled for window i. The F_i are calculated by Eq. (2.12)

$$exp(-\beta F_i) = \int P^u(\xi)exp[-\beta w_i(\xi)]d\xi \tag{2.16}$$

Because P^u enters Eq. (2.16) and F_i enters Eq. (2.13) via Eq. (2.15), these have to be iterated until convergence. For many bins, this convergence can be slow.

2.3 Coarse graining molecular dynamics

One of the major problems in atomistic simulation is the limited sampling of the phase space. The atomistic simulations are practically limited to simulation times and system up to 1 μ and 10 nm, respectively. With the current computational facilities, one cannot fill the time-scale and length-scale gap between computational and experimental methods of studying biological systems. Therefore, coarse graining of the systems to represent it with reduced (comparison with atomistic systems) number of degrees of freedom is a possible way to extend molecular modeling and bridge it with experimental techniques. Coarse grained (CG) models, in which small groups of atoms are represented by single interaction sites, are becoming increasingly popular to study systems of lipids and surfactants [156–158]. The overall aim of the coarse graining approach is to provide a

model that is computationally fast and able to reporoduce the experimentally observable properties.

In the present thesis, chapter 6 and 7 includes the self-assembly of the lipids, which is typically limited in terms of detailed atomistic simulations. Therefore, alternatively we employed CG graining simulations in order to explore the large length and longer timescale. We used Martini forcefield which is widely used for the biomolecular simulations. It is a very simple yet fast model developed by the groups of Marrink and Tieleman [158–160]. Martini model provides transferable potentials that describe the effects of hydrophobic, van der Waals, and electrostatic interactions between sites as a function of their polarity and charge. These potentials have been optimized and calibrated to reproduce the partitioning of model compounds between aqueous and hydrophobic environments [159].

The Martini model is based on the four-to-one mapping where a cluster of four heavy atoms is represented by a single interaction site (bead). The mapping is chosen as the best compromise between the computational efficiency and chemical representibility. Martini force field consists of beads that are divided into four types based on the chemical nature of the underlying structure. Polar (P), non-polar (N), apolar (C) and charged (Q). The charged and non-polar beads are further divided as hydrogen bond donor (d), accepter (a), donor-accepter (da) and none (0). While polar and apolar beads are subdivided on the basis of the degree of polarity in a increasing order from 1 to 5.

TABLE 2.1: Interaction energies (ϵ_{ij}) between martini beads.

		Q				**P**					**N**				**C**				
	sub	da	d	a	0	5	4	3	2	1	da	d	a	0	5	4	3	2	1
Q	da	O	O	O	II	O	O	O	I	I	I	I	I	IV	V	VI	VII	IX	IX
	d	O	I	O	II	O	O	O	I	I	I	III	I	IV	V	VI	VII	IX	IX
	a	O	O	I	II	O	O	O	I	I	I	I	III	IV	V	VI	VII	IX	IX
	0	II	II	II	IV	I	O	I	II	III	III	III	III	IV	V	VI	VII	IX	IX
P	5	O	O	O	I	O	O	O	O	O	I	I	I	IV	V	VI	VI	VII	VIII
	4	O	O	O	O	O	I	I	II	II	III	III	III	IV	V	VI	VI	VII	VIII
	3	O	O	O	I	O	I	I	II	II	II	II	II	IV	IV	V	V	VI	VII
	2	I	I	I	II	O	II	II	II	II	II	II	II	III	IV	IV	V	VI	VII
	1	I	I	I	III	O	II	II	II	II	II	II	II	III	IV	IV	IV	V	VI
N	da	I	I	I	III	I	III	II	II	II	II	II	II	IV	IV	V	VI	VI	VI
	d	I	III	I	III	I	III	II	II	II	II	III	II	IV	IV	V	VI	VI	VI
	a	I	I	III	III	I	III	II	II	II	II	II	III	IV	IV	V	VI	VI	VI
	0	IV	IV	IV	IV	IV	IV	IV	III	III	IV	IV	IV	IV	IV	IV	IV	V	VI
C	5	V	V	V	V	V	V	IV	IV	IV	IV	IV	IV	IV	IV	IV	IV	V	V
	4	VI	VI	VI	VI	VI	VI	V	IV	IV	V	V	V	IV	IV	IV	IV	V	V
	3	VII	VII	VII	VII	VI	VI	V	VI	IV	VI	VI	VI	IV	IV	IV	IV	IV	IV
	2	IX	IX	IX	IX	VII	VII	VI	VI	V	VI	VI	VI	V	V	V	IV	IV	IV
	1	IX	IX	IX	IX	VIII	VIII	VII	VII	VI	VI	VI	VI	VI	V	V	IV	IV	IV

The nonbonded interactions in the Martini are described by Lennard-Jones (12-6) potentials. The interaction strength between the beads is determined by the LJ well-depth

ϵ_{ij} depends on the particle i and j interacting with each other. The effective size of the particle is governed by σ_{ii} is 0.47 for all normal particle types except for the two special classed of rings (σ_{ii}=0.43) and antifreeze particles (σ_{ii}=0.62). Based on the interaction strength energy, each type of interaction is classified into a interaction level described as follows, O, $\epsilon = 5.6\ kJ/mol$, I $\epsilon = 5.0\ kJ/mol$, II $\epsilon = 4.5\ kJ/mol$, III $\epsilon = 4.0\ kJ/mol$, IV $\epsilon = 3.5\ kJ/mol$, V $\epsilon = 3.1\ kJ/mol$, VI $\epsilon = 2.7\ kJ/mol$, VII $\epsilon = 2.3\ kJ/mol$, VIII ϵ = 2.0 kJ/mol, IX $\epsilon = 2.0\ kJ/mol$ (σ=0.62 nm). The level of all inter-bead interactions are summarized in Table 2.1

Level O depicts highly polar interaction between the beads, is used to model the strong hydration shell of charged groups. Level I interaction also represents the strong polar interaction, but relatively lesser than of O level. Level II and III mimics ethanol or acetone in water, whereas IV models water-aliphatic chain interactions. Interactions V-VIII represents the hydrophobic nature of the interactions, however IX depicts the most apolar medium.

In the chapter 7 of the thesis, we have constructed the hydrophilic-hydrophobic model solid supports based on these interaction energies and have studied the effect of support hydrophilicity and hydrophoncity on the self-assembly of the lipids.

Chapter 3

ATP Induced conformation flexibility in PcrA helicase[1]

3.1   Introduction

The process of binding and hydrolysis of adenosine-triphosphate (ATP) of a protein/enzyme may result in the change in conformations of residues at the active site, which drives enzymatic reactions. This process is associated with a penalty in total energy. ATP hydrolysis is the source of energy, which facilitates many biologically important reactions where the chemical energy stored in the form of the chemical bonds is used to do work. The unwinding of duplex DNA by the enzyme helicase is a known example of such enzymatic reaction. These enzymes are motor proteins which translocate along nucleic acid unwind DNA in reaction that are coupled to the binding and hydrolysis of ATP [16]. Helicase transduces the chemical free energy change of ATP hydrolysis into the mechanical energy and translocate along the DNA. As a result helicase opens the duplex DNA (dsDNA) and converts it into single stranded DNA (ssDNA). The translocation is essentially driven by the conformational changes in the enzyme which assists DNA unwinding. The activity of these enzymes is coupled with the free energy of ATP binding and hydrolysis, which is intimately linked to the translocation of the protein along the DNA with a specific rate of approximately 50 nucleotides per second [21]. Therefore, understanding the helicase catalyzed unwinding process at the molecular level requires information about the coupling of ATP binding, its hydrolysis and the resultant protein translocation during the unwinding reaction. Helicases are grouped into 3 super-families SF1, SF2, and SF3 depending upon the conserved motif and structural

organization [161, 162]. SF1 superfamily consists of monomeric enzyme [19, 20], which acts as ssDNA 3-5 translocates. The members of SF1 superfamily, binds at 3 of the ssDNA and move towards the double stranded region progressively [163–165]. Rep, UvrD and PcrA are members of SF1 while RecG, PriA and HSV NS3 belong to SF2 superfamily and these are dsDNA translocates [162]. The DNA unwinding mechanism catalyzed by helicase is often explained by two popular models a) active rolling model [16, 24] and b) inchworm model [16, 23, 24, 166–168]. The active rolling model proposed by Lehman and Wong suggests that the dimeric helicase binds alternatively to dsDNA and ssDNA and the DNA unwinding is governed by conformational changes in the protein due to ATP binding and its hydrolysis. The entire process results in the breakage of inter-strand hydrogen bonds, leading to the destabilization of the DNA helix and finally separation of strands. In inchworm model, it is proposed that helicase binds to the ssDNA and then translocate unidirectionally along the DNA (with the help of ATP binding and hydrolysis), which results into the continuous breakage of the hydrogen bonds of the duplex [22]. Different families of DNA helicases were studied and addressed experimentally [16, 24, 166, 169] and theoretically [24–26, 162] to explain the unwinding process and the role of protein domains. Betterton et al. [170] addressed the function of helicases by using mathematical models. They investigated the coupling between ATP hydrolysis and translocation of the protein to describe the unwinding mechanism of DNA. Tuteja *et al.* [162] reviewed the protein sequence and performed sequence analysis of different DNA helicases and correlated experimental findings to understand the mechanism. Dittrich *et al.* [23] reported large scale conformational changes at the active site coupled with ATP hydrolysis using quantum mechanics and molecular mechanics (QM/MM) studies. Molecular dynamics (MD) simulation approaches were also used to investigate the structural properties of the helicase, mechanism of ATP hydrolysis, ATP binding, and conformational changes of the protein [24, 25, 171, 172]. PcrA (plasmid reduced copy) helicase from B. stearothermophilus has been crystallized and resolved at high resolution, in substrate state complex with ATP (3PJR) and a product state without ATP/ADP bound (2PJR) state which are available in protein data bank [173, 174]. The enzyme also crystallized in apo form (isolated protein) complex with ATP (1QHH) and without ATP (1PJR)(See Figure 3.1). PcrA helicase is a monomeric protein with four functionally important domains 1A, 2A, 1B and 2B. It is an ATP driven 3-5 helicase which binds to the 3 end of DNA and translocate towards the duplex region and open the dsDNA as proposed by the proposed inchworm model [168]. The whole mechanism is directed by the binding and hydrolysis of ATP which causes structural changes in the protein. The domains 1A and 2A of the protein are considered to be the functionally important domains which plays an important role in unwinding. These domains forms ATP binding site and are also involved in the translocation of helicase. The domains 1A and 2A undergo the conformational changes upon ATP binding and hydrolysis which

leads to the unidirectional motion by creating separation of domains referred as closed (ATP and DNA bound substrate) state and opened (DNA bound product) state, respectively [20, 25]. Binding of ATP freezes the domain to move closer to each other and ATP hydrolysis results in the domain separation, thus mediate translocation. Moreover, other domain, i.e., the 2B subdomain of PcrA helicase also shows significant movement by rotation about a hinge region emerging from the 2A subdomain [169]. The 2B subdomain of Rep monomer of same SF1 family can rotate by at least 130 form open and closed conformations [175–177]. So it is observed that every helicase domain plays an important role in the unwinding mechanism. Experimental and theoretical works till date lack of the understanding in many facets of the DNA unwinding mechanism. PcrA helicase domains exhibit translocation in absence of ATP (after hydrolysis and unbinding) [25, 26]. Therefore, the role of ATP unbinding in conformational change of the protein, which finally mediates the DNA unwinding, is an imperative problem to address. However, aiming the mechanism of ATP hydrolysis is beyond the scope of the conventional classical MD simulation. Therefore, in the present study, we have focused our investigation on the ATP release from its binding site of PcrA helicase. We have addressed the following questions. What is the energetic and the mechanism of ATP unbinding process from the binding site? What are the residues that actively take part in hydrogen bonding with the ATP molecule? Conformational change of the residues at the active site of the protein while unbinding of ATP? From the MD simulations, we have analyzed the structural changes of the protein domains when it goes from the substrate to the product state. In this work for the first time, we have explored the energetics of ATP unbinding from the substrate to the product state by calculating free energy of this process.

The work is organized in the following order with computational methods followed by results and discussions. We have reported the free energy of unbinding of ATP from the binding site of 1QHH and quantified the related local interactions and concluded the findings.

3.2   Computational Methods

All atomistic MD simulations were performed using GROMACS version 4.5.5 [147–149] with amber03 force field [137]. The crystal structure of 1PJR and 1QHH were obtained from the RCSB database (http://www.rcsb.org) [174]. We have considered and performed three different types of the simulations; a) equilibrium MD simulation to investigate the domain flexibility, b) steered MD simulation to pull the ATP molecule from the binding pocket of the protein, and c) umbrella sampling simulations on the reaction coordinate

(a)

(b)

(c)
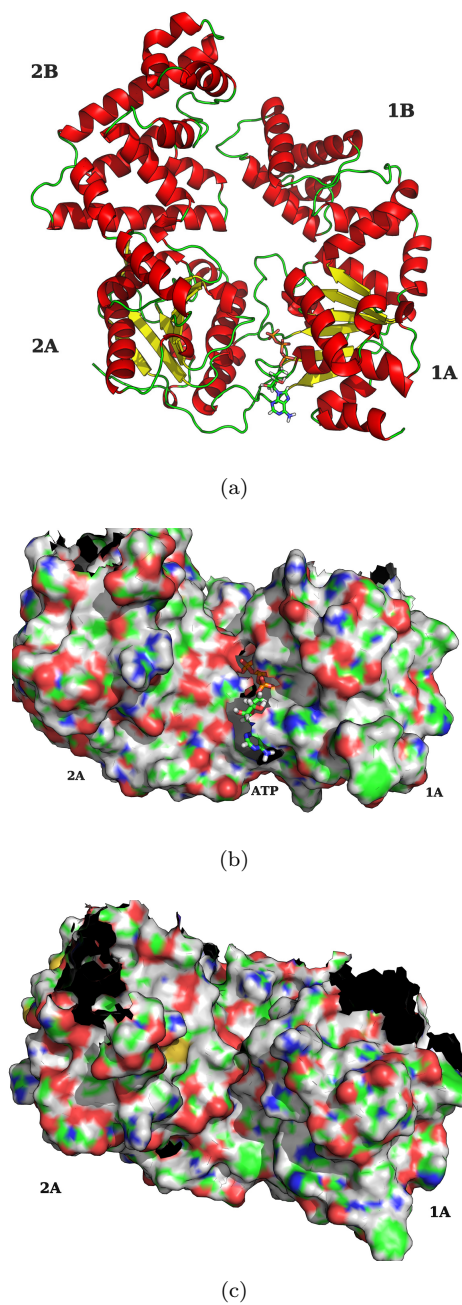
FIGURE 3.1: Crystal structures of PcrA helicase (a) 1QHH (ATP bound, cartoon view) (b) ATP bound to binding site, surface view, and c) ATP free binding site (1PJR, surface view).

of steered MD simulations, to determine the potential of mean force (PMF) of the ATP unbinding.

3.2.1   Equilibrium MD simulations

The helicase structure (1QHH) was solvated with explicit SPC [178] water molecules. Periodic boundary conditions were used in all the directions. Energy minimization of the starting structures was performed by the steepest descent method [179] as implemented in GROMACS. After minimization, the protein (excluding water molecules) was positioned restrained with a force constant 1000 kJ mol-1 for 5 ns in isothermal-isobaric (NPT) ensemble. The simulations were performed at 300 K and 1 bar. The v-rescale thermostat [180] with coupling time constant 0.1 ps and Berendsen barostat [181] with coupling time constant of 1 ps. The simulation time of 5 ns was enough for water molecules to equilibrate around the protein structure and penetrate to the solvent accessible areas. It was followed by steered molecular dynamics run simulations.

3.2.2   Steered MD simulation

Steered MD simulations (SMD) were performed to pull the ATP molecule from the binding pocket of the protein. The equilibrated structure of (after 5 ns of equilibration) 1QHH from the above MD simulations was used as a starting structure for SMD. During the SMD simulations, structure 1QHH (excluding water molecules and ATP) was position restrained with a force constant 1000 $kJmol^-1$. The ATP was pulled along the z axis with the force constant of 1000 $kJ/mol/nm^2$ and pull rate of 0.005 nm/ps for 2 ns with the pull code as implemented in GROMACS 4.5.5 [147–149]. The electrostatic and van der Waals cut-offs of 0.9 nm and 1.4 nm, respectively, were used. The simulation trajectory was written after every 1 ps. Initial 1 ns SMD trajectory was used for analysis. The same SMD trajectory was then used to generate configurations, which served as the starting coordinates for umbrella sampling simulations along the reaction coordinate. We have repeated the SMD simulations in total three times with the same reaction coordinate to check the reproducibility and better statistics. The center of mass (CoM) distance between ATP and protein from the three SMD runs were similar and are reported in Figure 3.2, which indicate that the system has followed the similar path of unbinding and the interactions of protein residues with ATP are similar during pulling.
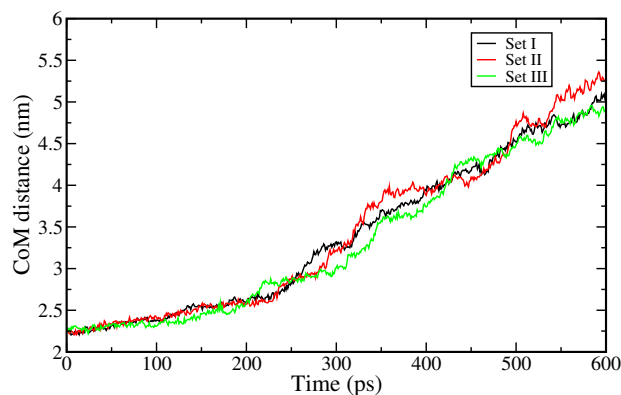
FIGURE 3.2: CoM distance between ATP and protein as a function of simulation time. Black, red and green lines represent SMD simulation set 1, 2 and 3 respectively.

3.2.3 Umbrella sampling simulation

To calculate the free energy of unbinding of ATP from 1QHH, PMF was calculated by using umbrella potential [153–155]. We have extracted the frames (configurations) from SMD trajectory from initial 450 ps along the reaction coordinate (description of the reaction coordinate is given in the results section). The reaction coordinates were considered (CoM distance) for umbrella sampling simulation till the separation of distance between protein and ATP reaches 4.2 nm the ($\approx 450ps$). We have taken windows (configurations) till 450 ps from 2 ns SMD trajectory, as the PMF reaches plateau within this time. For umbrella sampling simulations, an asymmetric distribution of sampling windows was used with spacing in sampling windows from 0.1 nm to 0.5 nm depending upon the separation. An umbrella potential of 1000 $kJmol^{-1}nm^{-2}$ was used for each window to hold the pulling group at the window positions. For small molecules, a force constants of 1000 $kJmol^{-1}nm^{-2}$ is found to be reasonable for producing the reliable PMFs. [182, 183] If the force constant is too small, the restrain force will not be sufficient to create a structure ensemble in a desire reaction coordinate. On the other side, too strong force constants restricts the sampling in a small region and hence the more number of sampling windows are required which would increase the computational cost. The protein (reference group) was position restrained using force constant of 1000 $kJmol^{-1}$. The position restraints enforce to prevent the complex from tumbling. This also allows to restrict the bias in the system to a given direction or path of unbinding otherwise, there might be chances of getting incorrect reaction coordinates. We simulated 30 sampling windows in total, each for 2 ns with umbrella potential. Thereafter, the weighted histogram analysis method (WHAM) [184] was used to calculate the PMF and finally Gibbs free energy. Number of bins and boot-strapping [185] steps were chosen to be 200 and 25 respectively to compute the statistical errors of the PMF. The umbrella sampling simulations were repeated two more times with the same reaction coordinate
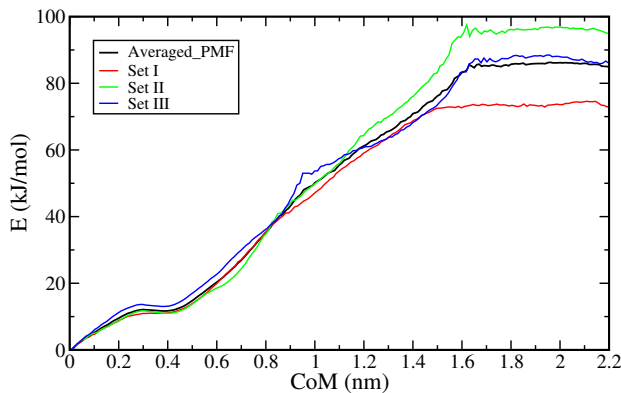
FIGURE 3.3: Potential mean force profile for ATP unbinding for three different set. Colors red, green and blue represents PMF for sampling set I , II and III respectively and black line shows average PMF profile.

to check the consistency of PMF obtained (Figure 3.3). However, we report here the average of the PMF taken from the 3 sets.

3.3   Results

3.3.1   Free energy for unbinding of ATP

Binding of the ATP at the active site transforms the helicase into closed substrate state with a minimum separation between protein domains. However, the hydrolysis of ATP in the substrate state induce the conformational changes in the protein domains, which rescues of the frozen domain (less mobile) state [24, 25, 171, 172] into the more mobile state. The free energy released as a result of ATP hydrolysis is then converted to mechanical energy used to translocate the protein domains. It converts ATP bound substrate state protein to the ATP free product state. Therefore it is expected that binding/unbinding of ATP is a crucial event in the DNA unwinding mechanism by PcrA helicase and plays a significant role in the domain motion by its presence and absence in 1QHH and 1PJR respectively. Hence, it is important to address the course of ATP binding or unbinding, the energetics of the process and the effect of it on PcrA helicase, particularly on protein domains 1A and 2A, which are important in the unwinding process. The process of unbinding of ATP can be understood by slowly detaching the ATP from its binding site. Therefore, we have separated the ATP and protein from each other as a function of their CoM distance by using MD simulation with pull force. The increase in CoM distances between protein and ATP as a function of simulation time during the SMD simulation is shown in Figure 3.4a (red line).

Thereafter, a series of configurations was generated along the pulled direction (z axis). The pulling direction or the reaction coordinate is schematically represented in Figure
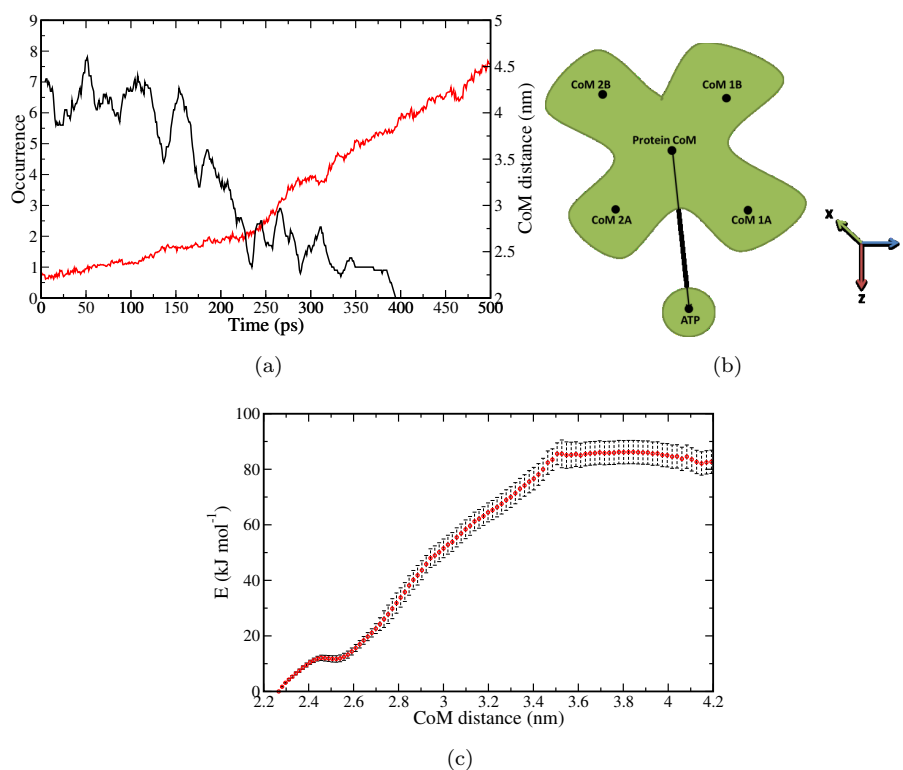
FIGURE 3.4: (a) H-bond count (black line) and distance between CoM of protein and ATP (red line) as a function of time. (b) Schematic representation of 1QHH after ATP is pulled along the Z direction. (c) PMF for ATP unbinding, X-axis represents the separation of ATP (CoM) from protein (CoM of domains 1A, 1B, 2A, and 2B) .

3.4b. The reaction coordinate and its direction are represented as the vector connecting the CoM of the whole protein and CoM of ATP. We have used a pull rate of 0.005 nm/ps and force constant 1000 $kJmol^{-}1$ to detach ATP molecule from the binding site of the protein. From the SMD simulation trajectory, we have extracted various configurations of the system based on the distance of the ATP from the protein along the reaction coordinate. These configurations were considered as starting structures and simulated for 2 ns by incorporating an additional umbrella potential. Umbrella sampling [186] was performed to calculate the change in free energy of unbinding of ATP from the active site. The WHAM [184] method was used to compute the potential of mean force for the unbinding of ATP and is plotted in Figure 3.4c. We have ensured a sufficient overlap between histograms of configuration of the adjacent windows, which is necessary to obtain continuous smooth PMF from WHAM along the reaction coordinate (Figure 3.5).

The free energy change described by the PMF includes average effects of the separation between the two entities and explicit solvent molecules. The PMF was plotted against the separating CoM distance between ATP and protein in Figure 3.4c. The statistical errors of PMF were computed using the bootstrap analysis and plotted in the same figure. From
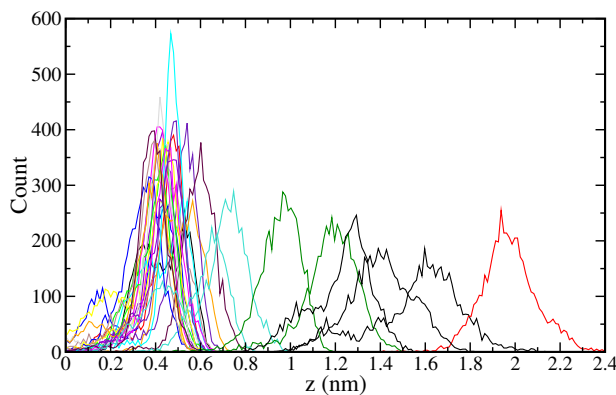
FIGURE 3.5: Histogram of configuration in each sampling window along the reaction coordinate (z axis).

the PMF plot, the estimated free energy for the unbinding of ATP from the active site of 1QHH is $\sim 85kJmol^-1$ (i.e., the binding free energy is -85 $\pm 5kJmol^-1$). The binding free energy estimated in the current work is in good agreement with the free energies reported for small molecules (e.g., oxime drugs) and ATP, which ranges in between -70 to -90 $kJmol^{-1}$ [187–189]. However, the contribution to the free energy from the long time scale domain motion could not be accounted, as this time scale is out of reach for the all atomistic MD simulation. This time scale can be achieved by the coarse-grained methods where we lose the atomic details hence the important degrees of freedom i.e., local conformation changes of the residues at the active site. In fact, the calculated free energy includes mainly comes from conformational changes of residues of protein near to the binding site and hydrogen bonds between ATP and protein. Therefore, we have further investigated the details of local interactions between ATP and the residues of the protein at the binding site.

To make sure the consistency of the PMF results, we also carried out the SMD even slower pulling velocity of 0.001 nm/ps which resulted in the production of nearly identical trajectory as for pulling velocity of 0.005 nm/ps. We also carried out the umbrella sampling simulation and generated the PMF. The potential of mean force obtained for the smaller velocity does not deviate much from the free energy reported with pulling velocity of (0.005 nm/ps) (see Figure 3.6). In consistence with our findings, we also obtained the stationary phase with much slower pulling rate which is very similar with the previous one.

3.3.2 Effect of ATP unbinding

The ATP bound state (1QHH) is the most stable conformation and thus has a minimum energy (Figure 3.4c). During the unbinding process of ATP, we observe that the system acquires stability (plateau) in the PMF at the reaction coordinate between 2.42 nm
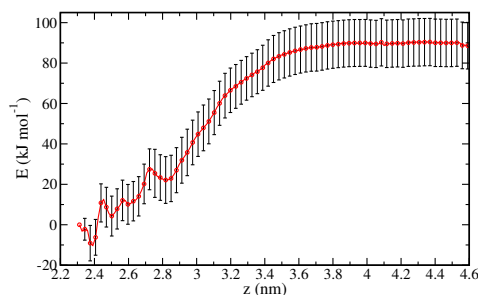
FIGURE 3.6: Potential mean force profile for ATP unbinding with slower pull rate of 0.001 nm/ps.

(a)

(b)

(c)
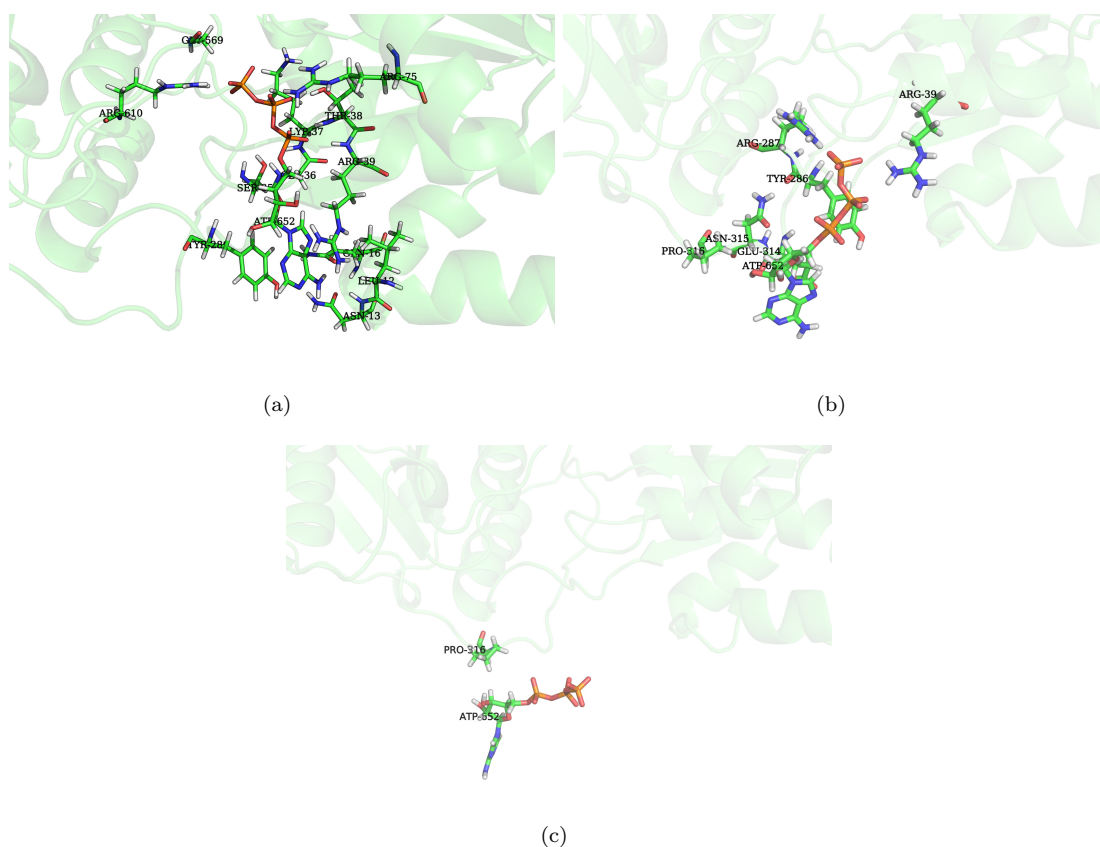
FIGURE 3.7: Snapshots representing ATP at CoM distance a) 2.3 nm b) 3.5 nm and c) 4.1 nm from CoM of protein.

and 2.52 nm, thereafter a steep rise in the energy profile is seen (Figure 3.4c). While unbinding, ATP has to overcome local interactions arising from the residues near the binding site. Therefore, the stability near the binding site may occur due to the favorable interactions of ATP with the nearby residues (interactions schematically represented in Figure 3.7).

However, the presence of stable region may be also a result of the local re-arrangement or change in the orientation of the residues at the active site of the protein that enhances the interactions. The interactions between protein and ATP are mainly non-bonded

interactions e.g. hydrogen bond. Therefore, we investigated it further by calculating the variation in the number of hydrogen bonds (H-bonds) between the protein and ATP during the process of unbinding (plotted in Figure 3.4a, black line). The hydrogen bonds were computed based on the donor-acceptor distance of $3\mathring{A}$ or less and the H-donor-acceptor angle of $20°$ or less. All the H-bond donor and acceptor atoms of protein residues and ATP were taken into consideration for the hydrogen bond calculation.

3.3.3 Variation of Hydrogen bond as the ATP is pulled

In an ideal scenario, the interaction between the two moieties decreases as the separation between them increases. From Figure 3.4a, we have observed a gradual decrease in the hydrogen bonding between protein and ATP with the increase in the CoM distance between them. This decrease vanishes as the separation between ATP and protein is approximately 4 nm. Interestingly, we notice a slight increase in the number of H-bonds at the early stage of unbinding (50 ps or $\sim 2.4nm$). Also, we have observed a significant number of H-bonds till 180 ps (i.e., at a separation of 2.52 nm). Thus the initial increase and a significant number of H-bonds between ATP and protein till 180 ps illustrates favorable interaction, which may give rise to the stationary phase in the PMF plot (at the CoM distances between ~ 2.42 to ~ 2.52 nm) in Figure 3.4c. It suggests that during the unbinding process, initially, ATP tries to attain a relatively stable configuration. Therefore, we have explored the reason for such stability further in the thesis.

The formation of the hydrogen bonds may be enhanced by the change in the conformations or local fluctuation of the nearby residues during unbinding of ATP. We have examined the fluctuations of the protein residues during ATP unbinding. Root mean square fluctuations (RMSF) of the protein were computed from the first 500 ps of the SMD trajectory and are shown in Figure 3.8a.

It is observed that, some residues of the domain 1A and 2A are fluctuating at higher extent amongst all. These are mainly the conserved residues of the helicase family, which forms the inter-domain cleft necessary for ATP binding. Tuteja et al. [162] and Dittrich et al. [23] revealed that amongst 1A and 2A domain, residues Gly34, Gly36, Lys37, Thr38, Arg39, Arg75 (domain 1A) and Gln254, Tyr286, Arg287, Gly569, Leu570, Glu571, and Arg610 (domain 2A) are known to be highly conserved residues in the helicase family and are found at the active sites of the protein and involved in DNA and ATP binding. The spatial arrangement of these residues at the active binding site is depicted in Figure 3.8b with ATP (1QHH). The nature of the interaction of these residues with ATP is mainly non-bonded, especially governed by hydrogen bonds (H-bonds). Thus, we have calculated the percentage occupancy of H-bond (the percentage of time that various

(a)

(b)
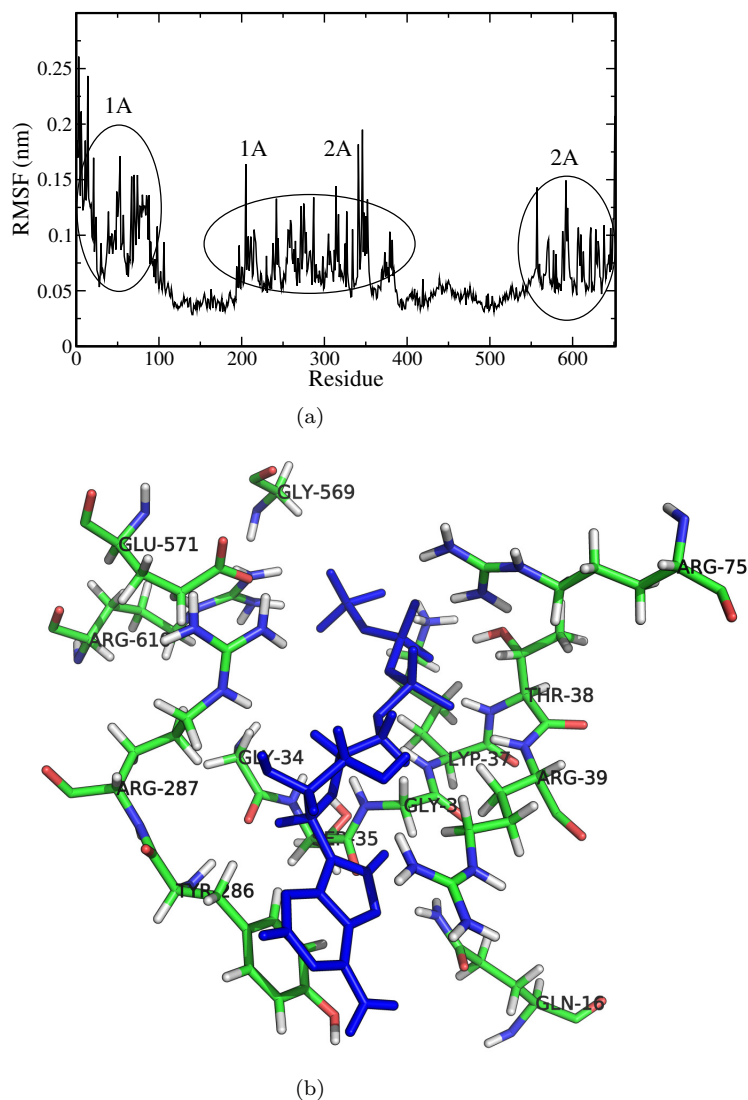
FIGURE 3.8: (a) Root mean square fluctuation (RMSF) of protein residues during the unbinding of ATP from 1QHH. (b) snapshot of the crystal structure of 1QHH. It shows the residues at the active site of 1QHH. ATP is represented as blue sticks.

hydrogen bonds observed during the simulation) during the SMD simulation and are tabulated in Table 3.1. For example, if a particular H-bond remains intact during 30% of the simulation time, then its occupancy is 30%. These are averaged values from three sets of independent SMD simulations. It shows that Arg (Arg610, Arg75, Arg39, Arg287) from both the domains and Thr38 from domain 1A have higher occupancies than other residues. So these residues contribute more in forming H-bond interaction with the ATP molecule.

We have also carried out two more independent (of previous direction) sets of SMD simulations with different unbinding pathway to check the effect of different pulling direction. ATP was pulled in the tilted direction toward x and y directions (of the box, away from the protein) with respect to the z direction (termed as xz and yz respectively)

TABLE 3.1: Shows percent occupancies of hydrogen bonds between ATP and various active site residues of 1QHH system during SMD runs. Here side refers to the side chain atoms and main refers to the main chain atoms.

Donor	Acceptor	Occupancy (%)
ARG610-Side	ATP652-Side	31.10 ± 5.96
THR38-Side	ATP652-Side	29.31 ± 6.58
ARG287-Side	ATP652-Side	13.54 ± 6.16
THR38-Main	ATP652-Side	12.84 ± 4.11
ARG75-Side	ATP652-Side	12.61 ± 4.59
ARG39-Side	ATP652-Side	11.51 ± 3.02
ARG39-Main	ATP652-Side	10.91 ± 3.24
LYP37-Side	ATP652-Side	9.65 ± 7.16
GLY34-Main	ATP652-Side	5.49 ± 2.32
GLN16-Side	ATP652-Side	4.06 ± 2.73
GLY36-Main	ATP652-Side	1.20 ± 0.98
LYP37-Main	ATP652-Side	0.67 ± 0.98

TABLE 3.2: Percentage occupancies of hydrogen bonds between ATP and various active site residues of 1QHH system during SMD runs along xz and yz direction.

Set 2 (xz)			Set 3 (yz)		
Donor	Acceptor	Occupancy	Donor	Acceptor	Occupancy
THR38-Side	ATP652-Side	66.07%	ARG39-Side	ATP652-Side	36.93%
ARG287-Side	ATP652-Side	48.70%	THR38-Side	ATP652-Side	35.13%
LYP37-Side	ATP652-Side	38.52%	ARG287-Side	ATP652-Side	28.94%
ARG75-Side	ATP652-Side	37.72%	ARG75-Side	ATP652-Side	26.15%
ARG610-Side	ATP652-Side	35.33%	LYP37-Side	ATP652-Side	23.95%
ARG39-Main	ATP652-Side	32.73%	ARG39-Main	ATP652-Side	23.35%
ARG39-Side	ATP652-Side	20.16%	ATP652-Side	GLN16-Side	13.97%
THR38-Main	ATP652-Side	17.96%	THR38-Main	ATP652-Side	13.57%
ATP652-Side	HID11-Main	15.57%	GLN16-Side	ATP652-Side	7.19%
ATP652-Side	GLN16-Side	12.38%	ARG610-Side	ATP652-Side	5.59%
SER35-Main	ATP652-Side	9.78%	GLY36-Main	ATP652-Side	2.20%
GLY36-Main	ATP652-Side	7.39%	ATP652-Side	ALA10-Main	1.80%
LYP37-Main	ATP652-Side	4.79%	-	-	-

to check the effect of the different pulling direction on the conformational changes at the binding site(Schematically shown in Figure 3.9a). We have plotted the occurrence of the hydrogen bonds as a function of simulation time (Figure 3.9b) and reported the residues involved in the hydrogen bond formation (Table 3.2). We have noticed the same residues as above contribute more toward hydrogen bond formation.

Further to visualize hydrogen binding, we have computed the Non-Covalent Interaction (NCI) by using NCIPlot developed by Garcia et al. [190] between the active site residues and ATP. NCI characterizes the non-covalent interactions such as van der Waals interactions (vdW), steric clashes (SC), and hydrogen bonds (HBs) based on pairwise distances

(a)

(b)
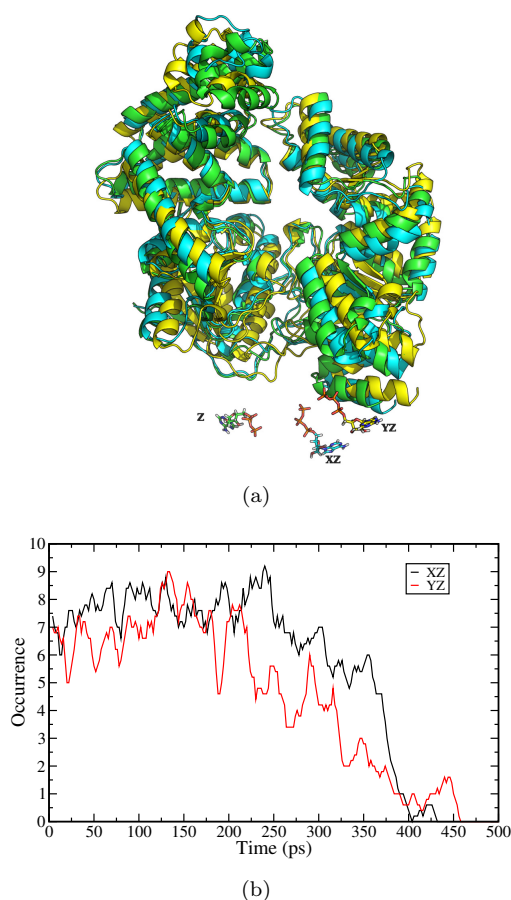
FIGURE 3.9: a) Schematic representation of the pulling direction of ATP b) occurrences of hydrogen bond as a function of simulation time.

between atoms according to their vdW radii and electronic density. We investigated the interactions between active site residues and ATP by plotting the reduced density gradient versus electron density multiplied by sign of second Hessian eigen value [190] in Figure 3.10. It is computed for the binding cleft residues (Gly34, Gly36, Lys37, Thr38, Arg39, Arg75, Gln254, Tyr286, Arg287, GLY569, Glu570, and Arg610) and ATP. We have compared the NCIplot of ATP bound conformation with the four different configurations extracted from the SMD trajectory at different simulation time e.g. the bound state 0 ps and 70 ps (Figure 3.10a), 90 ps (Figure 3.10b), 110 ps (Figure 3.10c) and at unbound state 500 ps (Figure 3.9d). The low-density, low-gradient spike at negative side signifies the stabilizing interactions. The large negative values of sign $(\lambda_2)\rho$ indicates attractive interactions such as dipole-dipole interactions or hydrogen bonding. While, large and positive sign $(\lambda_2)\rho$ depicts repulsive interaction. The values near zero indicates weak interactions and 0 signifies no interactions. From Figure 3.10, the low-density low-gradient spikes observed for both the ATP bound and SMD configurations clearly depicts the existence of hydrogen bonds between ATP and active site residues. However, SMD configurations shows low-density and low-gradient spikes more towards the negative
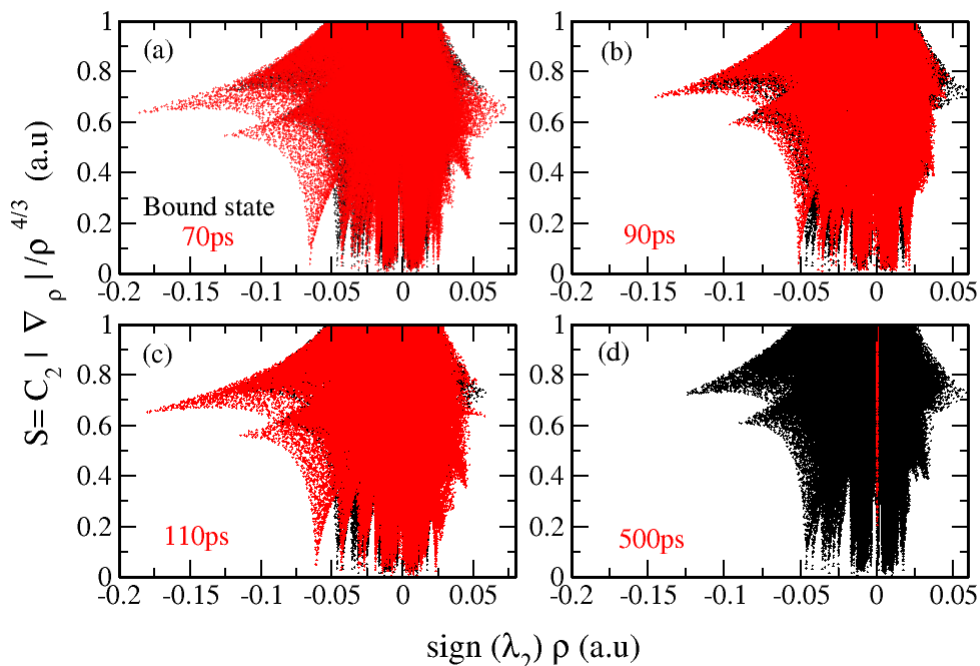
FIGURE 3.10: Reduced density gradient vs sign $(\lambda_2)\rho$. Color black and red represents ATP bound and SMD configurations respectively.

scale which signifies attractive interactions and more number of H-bonds Figuer 3.10 a b and c.

It is clearly evident from the figure that as we move the ATP from the binding pocket the interaction increases and thus stabilizes the PMF. As we move ATP further, the interactions eventually get weakened and then vanished (Figure 3.10d). We also observed some van der Waals and repulsive interactions from the spikes near 0 and positive side respectively for ATP bound, 70 ps, 90ps and 110ps configurations.

Thereafter, we have plotted the density gradient isosurface to visualize these interactions. In Figure 3.11 we have shown the gradient isosurface of non-covalent binding at different time of SMD simulation (described above). We have used gradient cutoff of s = 0.35 au and the color scale is $0.04 < \rho < 0.04$ au. The colors ranging from blue to red indicates the strength of interactions according to values of sign $(\lambda_2)\rho$. Blue indicates strong attractive interactions and red indicates strong non-bonded overlap (repulsion). The higher density portions of the isosurface correspond to hydrogen bonds between active site residues and ATP. We have used the same value of s and same range of ρ for all the snapshots. Therefore, From Figure 3.10 (a-c) and 3.11 (b-c), it is clearly evident that, the interactions between the binding site residues and ATP increase after initial

a) ATP bound state   b) 70th ps frame

c) 110th ps frame   d) ATP unbound state
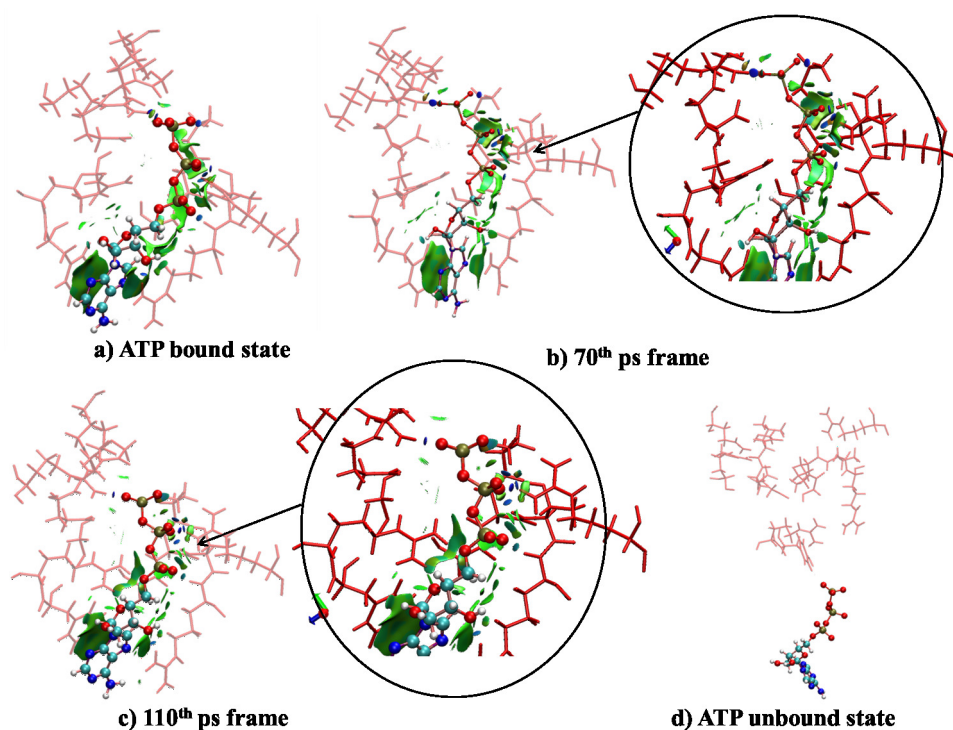
FIGURE 3.11: NCI isosurface around ATP in the active site of PcrA helicase protein. The gradient cut-off is s=0.35 au, and the color scale is -0.04 $< \rho <$ 0.04 au. Active site residues are explicitly shown in red color.

unbinding. This confirms that when ATP unbinds from the active site, residues reorients and stabilizes the interaction by the formation of hydrogen bonds with the ATP molecule.

3.3.4 Distance distribution between the H-bonding atoms of residues in the binding site with ATP

From Table 3.1, it is evident that ATP primarily acts as the H-bond acceptor (also seen from Figure 3.11). Thus, the H-bond can be formed between the donor atoms of residues at the active site with the acceptor atoms of the phosphate moiety of ATP. So, we have calculated the distribution of distances between H-bond donor atoms of active site residues and the oxygen atoms of α, β and γ phosphate groups of ATP. These distributions are depicted in Figure 3.12.

The distributions were computed from the ATP bound and ATP pulling (SMD) trajectories and they represent the possibility of the formation of H-bond between enzymatically active residues and ATP in bound state and during unbinding. The distance distribution from the ATP bound simulation trajectory was computed and termed as bound. In case of SMD trajectories, the distributions were generated in the successive interval of 100 ps, e.g (0-100 ps) and termed as 0-100 ps. Similarly, the distributions 100-200 ps, 200-300
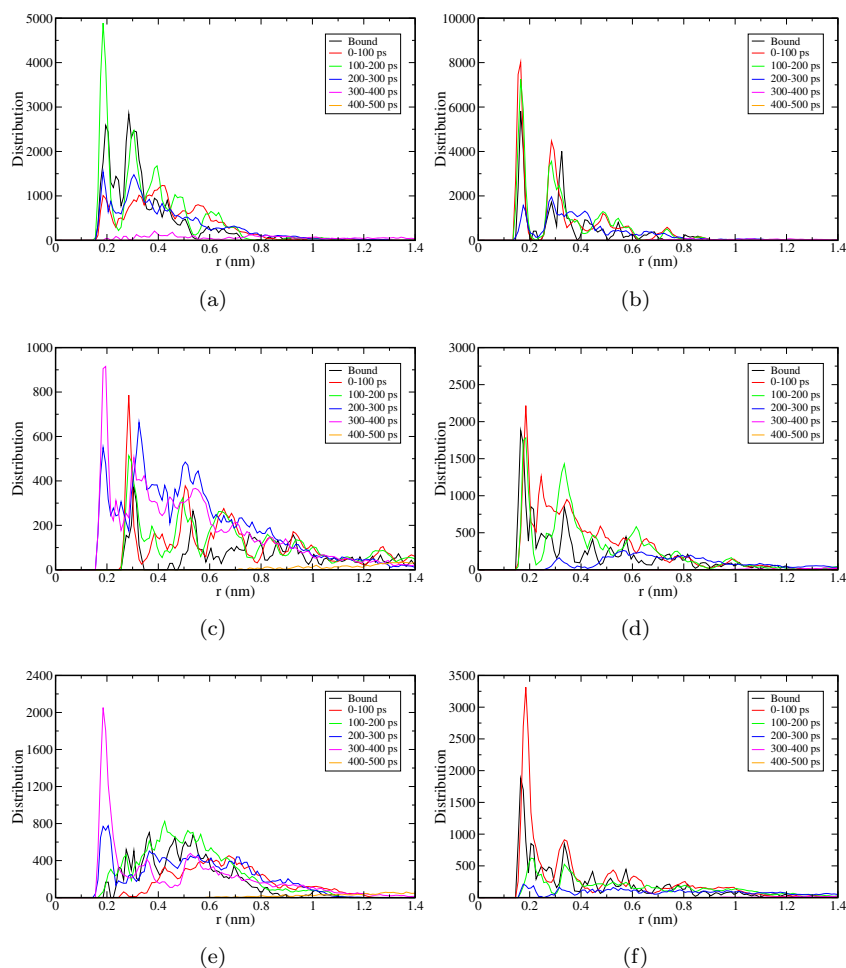
FIGURE 3.12: Distribution of the distances between H-bond donor atoms of residues (a) Lys37, (b) Thr38, (c) Arg39, and (d) Arg75, (e) Arg287, (f) Arg610 and oxygen atoms of , and phosphate group of ATP of domain 1A. Bound refers to the simulation trajectory where ATP was not pulled. 0-100 ps, 100-200 ps, 200-300 ps represent time intervals..

ps, 300-400 ps and 400-500 ps were generated from the SMD simulation trajectory in the time window of 100-200 ps, 200-300 ps, 300-400 ps, 400-500 ps respectively. Figure 3.12 (a, b, c, d, e and f) represents these distributions for Lys37, Thr38, Arg39, Arg75, Arg287 and Arg610 respectively. The minima of the first peak of the distributions at 0.3 nm or less are the H-bonding distances. Since, ATP bound state is the most stable configuration, we can assume that the interactions would be higher and it would fade away as it was pulled out from the active site. However, in all the cases, the distributions for the H-bonds formation are not at maximum for bound state (black line). These distributions attain the maxima at the intervals of 100-200 ps for Lys37, 0-100 ps for Thr38 and Arg610 and 300-400 ps for Arg287. This suggests that these residues come near to the proximities of ATP during the process of unbinding and therefore show greater peak heights at the hydrogen bonding distance between donor and acceptor atoms (≤ 0.3 nm). For Lys37 (in Figure 3.12a), at the ATP bound state the H-bond

(a)   (b)
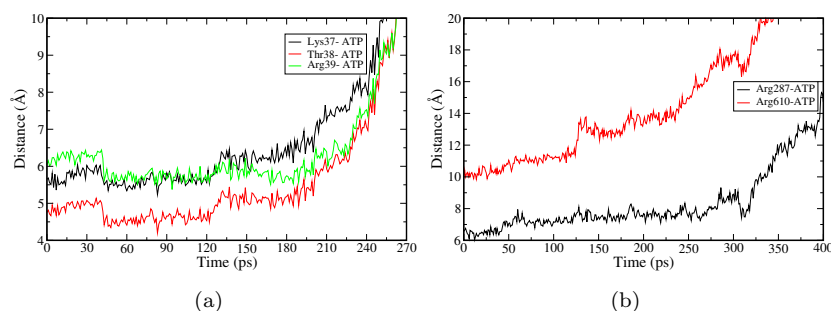
FIGURE 3.13: CoM distance between ATP and (a) Lys37, Thr38 and Arg39 of domain 1A. (b) Arg287 and Arg610 of domain 2A.

interactions are weak as compared to the 100-200 ps plots. When ATP is pulled from the active site, the CoM distance between Lys37 and ATP should increase; but rather it has decreased after $\sim$ 40 ps (Figure 3.13a, black line).

We have used a pull rate of 0.005 nm/ps to detach ATP from the binding site, therefore in an ideal scenario; at 200 ps ATP should have moved a distance of 10 $\mathring{A}$ from its initial state (the ATP bound state). However for Lys37, from Figure 3.13a, it is evident that ATP has moved only 6 $\mathring{A}$. This shows that there are interactions, which indeed tries to hold ATP and as the pull force overcomes the binding energy, ATP moves away. Similar observations are seen for Thr38 and Arg39 (Figure 3.12a). Figure 3.13 shows that in the region of 40-140 ps time, a decrease in the CoM distance between the residues and ATP is noted. This eventually gives rise to the greater peak heights in distance distribution for Lys37, Thr38, and Arg39 (Figure 3.12a, b and c respectively) in the time interval of 0-100 ps and 100-200 ps. Even the CoM distance between ATP and residue do not change (Figure 3.13a) when the ATP was pulled. The interactions, which hold the ATP can also re-orientation the residues (see section on conformation change, section c) i.e., induce local conformational changes. In case of Arg39 (Figure 3.12c) we observe a significant distribution at the distance of 0.3 nm till 200 ps. However, beyond 200 ps, we also observed a finite distribution of H-bond distances (at 0.2 nm separation between ATP and Arg39) even though there is a gradual increase in the CoM separation between Arg39 and ATP (Figure 3.13a) at that time. From Figure 3.14a (and visualizing the trajectory), we have observed a head-on orientation of Arg39 (guanidine moiety) with ATP (Phosphate group).

Primarily, within 0 to 200 ps of time, ATP interacts prominently with the main chain N atom. However, beyond 200 ps, the interaction of ATP gradually increases with the side chain N atoms of guanidine (schematically showed in Figure 3.14a). Thus to investigate it further , we have computed the CoM distance of the arginine main chain atoms and guanidine moiety with the phosphate group of ATP and plotted in the Figure 3.14b. It shows that till 220 ps, the ATP and main chain atoms of Arg39 are closer
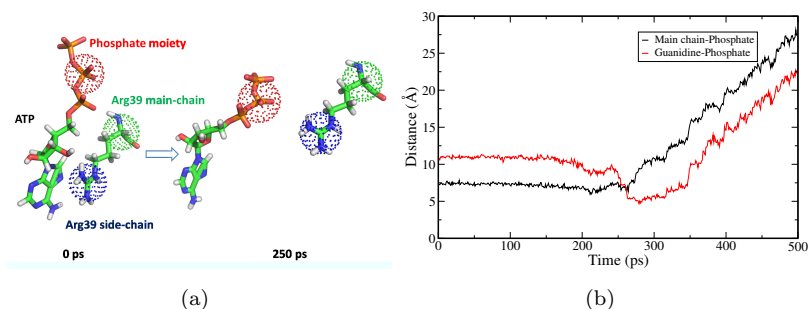
FIGURE 3.14: (a) Schematic representation of residue Arg39 and ATP at time 0 ps and 250 ps.(b) CoM distance between ATP phosphate group and Arg39 main chain (black) and Arg39 side chain (red).

than guanidine moiety of Arg39. After 220 ps, ATP-main chain distance increases and ATP-guanidine moiety comes closer. This proves that ATP interacts with the Arg39 via main chain atoms in the early stage of unbinding and beyond 220 ps, it moves apart and comes near to the side chains of Arg39 (guanidine moiety). We have also observed that there is a change in the conformation of Arg39 residues and it is discussed later in the thesis (section 3.3.5). This also leads to a shorter separation between hydrogen bond donor atoms of Arg39 and acceptor atoms of ATP. Figure 3.12d shows that the distance distribution between the Arg75 (H-bond donor atoms) and ATP (H-bond acceptor atoms) has prominent peaks in the bound state, 0-100 ps and 100-200 ps. Then at subsequent time there is a shift and decrease in the peak height. Further distance distributions of Gly34, Gly36 and Gln254 were computed and are depicted in Figure 3.15 and these residues do not show any distribution at the H-bonding distance but long range weak interactions.

For Arg287 (Figure 3.12e), there are hardly any occurrences at the H-bonding distance for the ATP bound trajectory. The occurrence at the H-bonding distance starts appearing after 200 ps and in the 300-400 ps interval, a prominent peak at the H-bonding distance (at ~ 0.2 nm) is observed which faints away after 400-500 ps. Interestingly, we observed a similar head-on interaction between Arg287 and ATP as seen for Arg39 which leads to a peak in distribution of H-bond distance at 0.2 nm (i.e. 200 ps) in Figure 3.12e even though the CoM separation between ATP and Arg287 (see Figure 3.13b) increases as a function of time. This observation is also seen on visualizing the SMD trajectory where we observed that the H-bond acceptor atoms of ATP and H-bond donor atoms of Arg287 come close due to attractive interaction, while the remaining part of the ATP move away. Visualization of trajectory also reveals that there are some conformational changes in the residues and ATP. This is discussed in section c. For Arg610, we observed peaks at the H-bonding distance for the ATP bound state. As the ATP is pulled, we found a significant interaction between Arg and ATP at the H-bonding distance (Figure 3.12f) in

(a)

(b)

(c)
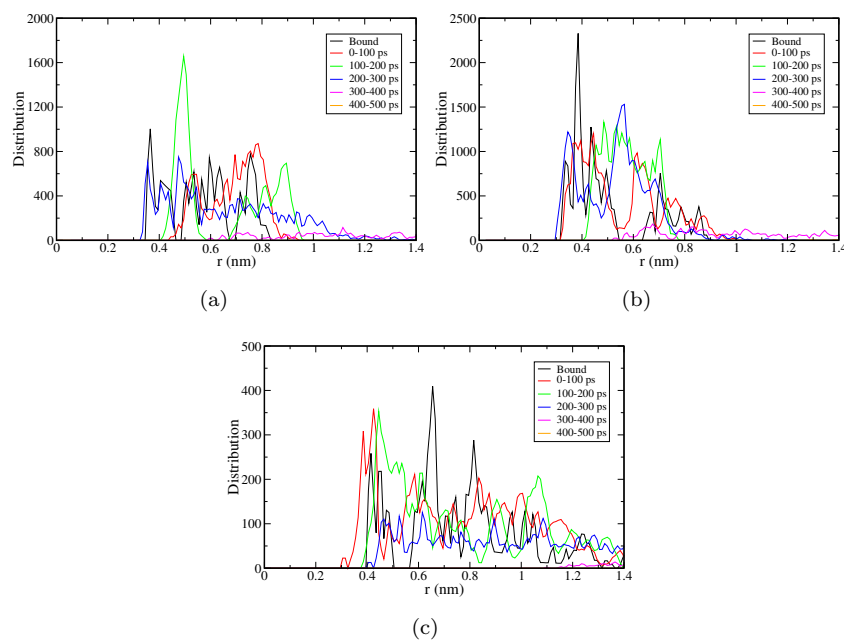
FIGURE 3.15: Distribution of the distances between hydrogen bond donor atoms of residues (a) Gly34 (b) Gly36 and (c) Gln254 and oxygen atoms of , and phosphate group of ATP.

the time interval of 0-100 ps, thereafter, the distribution fades away when ATP moves far from the binding site. Other residues from the same domain are shown in Figure 3.16 and they do not show any distribution at the H-bonding distance but weak long range interactions are present.

3.3.5   Conformation changes among the residues and ATP

There are some distance dependent interactions, which get strengthened as ATP is pulled from the active site of the protein. These interactions may have resulted due to the change in the conformations or re-orientation of residues and/or ATP. In this section we have discussed these changes both qualitatively and quantitatively. The conformational flexibility of residues at the molecular level can be studied by monitoring the change in torsional angle as a function of simulation time. For the protein residues there can be torsional motions in the main chain atoms and in the side chain atoms. As the main chain atoms are linked with the previous and subsequent residues, we did not observe significant deviation in the dihedral rotation. The main chain dihedral angles are plotted in Figure 3.17. Here, we have observed that the dihedral angle between the residues fluctuates in a small range and do not change to any other conformation. We have also calculated and plotted the dihedral angles of the side chains as a function of time in Figure 3.18.
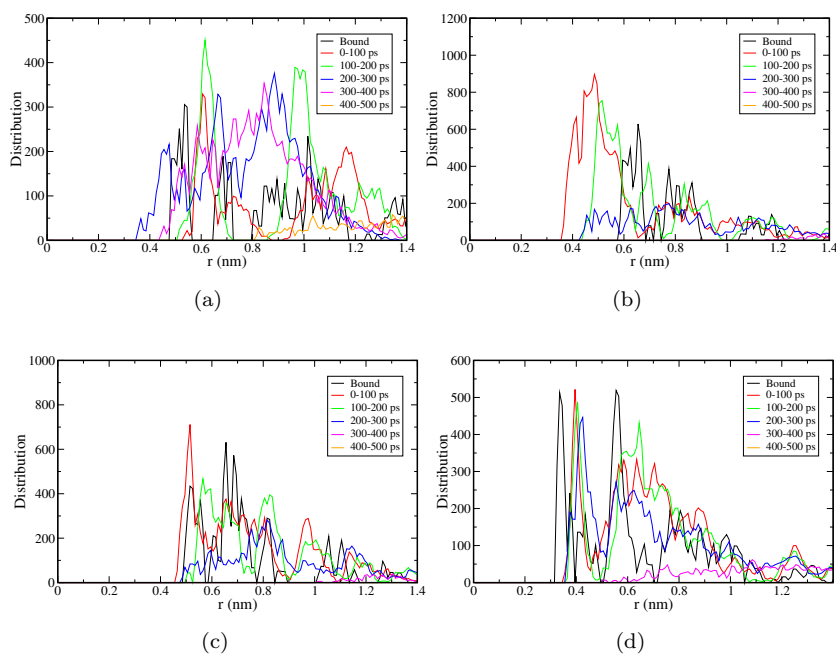
FIGURE 3.16: Distribution of the distances between hydrogen bond donor atoms of residues (a) Tyr286, (b) Gly569 (c) Leu570 and (d) Glu571 and oxygen atoms of , and phosphate group of ATP.
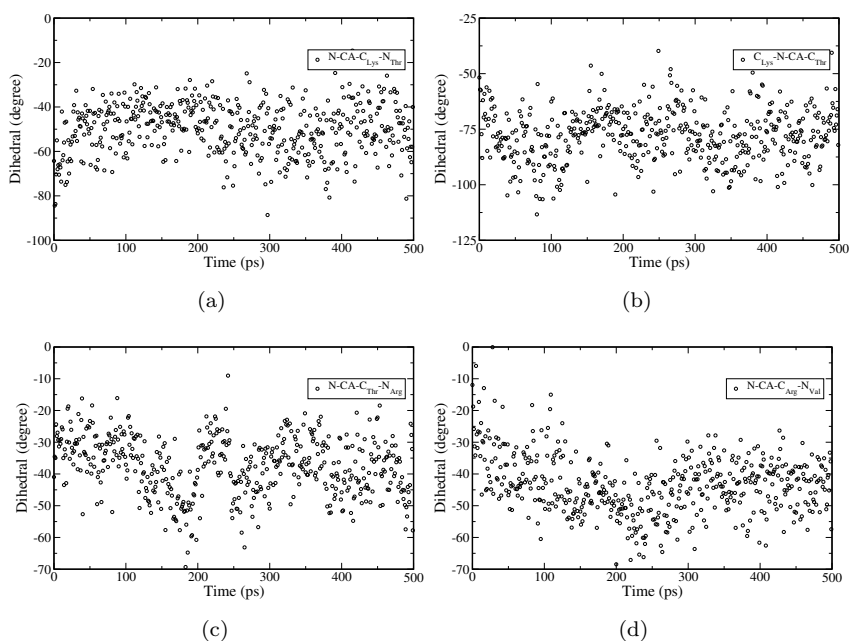
FIGURE 3.17: Main chain dihedrals of the residues Lys37-Thr38-Arg30-Val40 in the active sites of the domain 1A. (a) N-CA-C$_{Lys}$-N$_{Thr}$ (b) C$_{Lys}$-N-CA-C$_{Thr}$(c) N-CA-C-N$_{Arg}$ and (d) N-CA-C$_{Arg}$-N$_{Val}$.
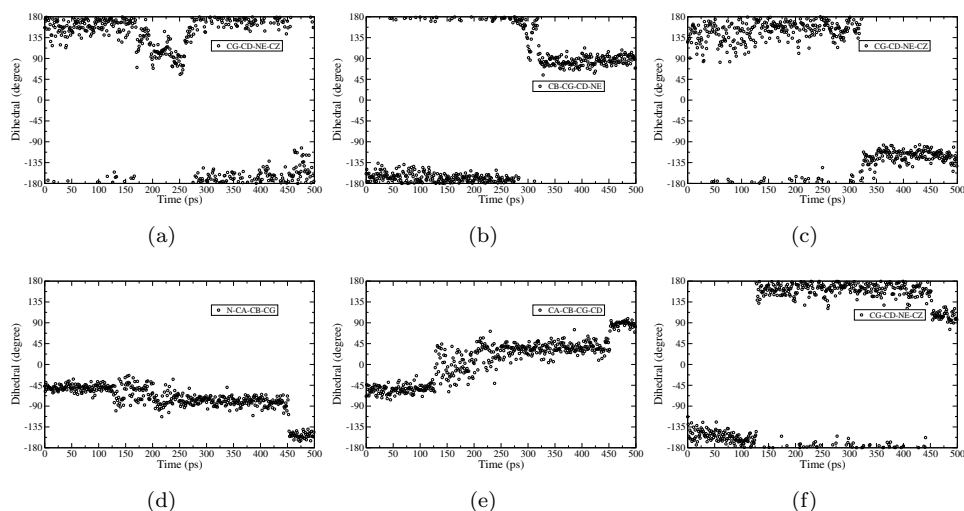
FIGURE 3.18: Variation in the side chain dihedrals angle of Arg39 (a), Arg287 (b,c) and Arg610 (d, e and f).
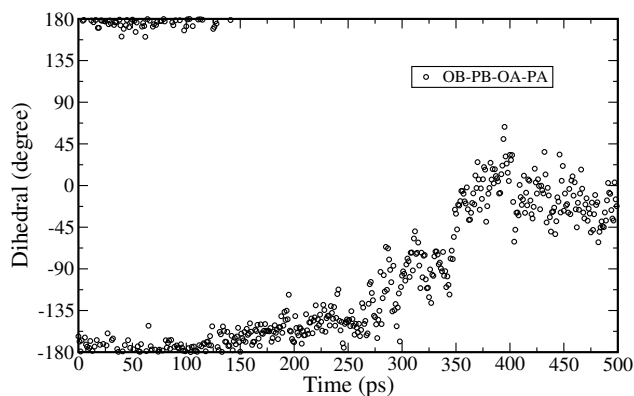
FIGURE 3.19: Dihedral angles variation (OB-PB-OA-PA) of ATP with the function of simulation time.

We observed (Figure 3.18a) Arg39s CG-CD-NE-CZ dihedral changed from $+180°$ (at 0 ps) to $+50°$ (at 180-280 ps) and then it stayed around $180°$. Similarly, side chain dihedral angles CB-CG-CD-NE and CG-CD-NE-CZ of Arg287 also got changed (shown in Figure 3.18b and c) as a function of time. Dihedral CB-CG-CD-NE (Figure 3.18b) of Arg287 adopted an angle of $90°$ at 300 ps from $180°$. While dihedral CG-CD-NE-CZ changed to $-135°$ at 300 ps from $135°$ (Figure 3.18c). As ATP was pulled, Arg287s guanidine moiety got reoriented towards the phosphate group of ATP. As evident from Figure 3.12d, that the interaction of ATP with Arg610 is prominent in time range of 0-100 ps, thus the dihedrals (N-CA-CB-CG, CA-CB-CG-CD, and CG-CD-NE-CZ) of Arg610 in this time range did not change significantly (Figure 3.18d, e and f). However, these dihedrals eventually got shifted to another value with time, i.e., as ATP was pulled out from the active site.

In addition to the conformational changes in the residues, we have calculated and plotted
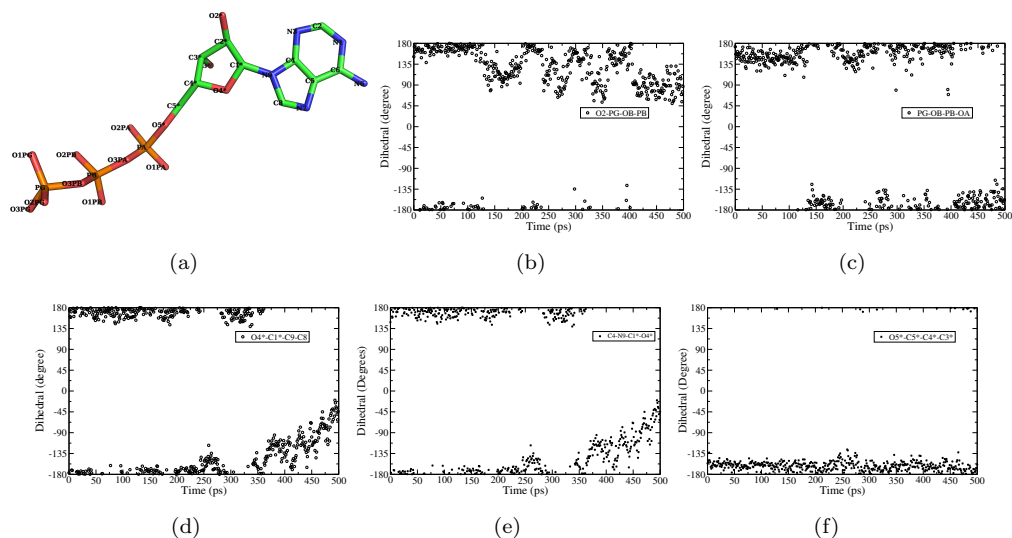
FIGURE 3.20: Dihedral behavior of ATP with the function of simulation time a) schematic representation of ATP molecule. Dihedral angle represents b) O2-PG-OB-PB, c) PG-OB-PB-OA, and d) O4*-C1*-C9-C8 e) C4-N9-C1*-O4* and f) O5*-C5*-C4*-C*.

the dihedral angles for ATP as a function of simulation time. It was observed that the dihedral OB-PB-OA-PA of ATP stayed at anti conformation ($180°$ or $-180°$) till 130 ps and gradually changed to syn conformation (Figure 3.19). In this way, by changing its conformations ATP tries to maximize the interaction with binding site residues i.e., Arg39 and Arg287. In Figure 3.20 we have plotted dihedral angles O2-PG-OB-PB, PG-OB-PB-OA, O4*-C1*-C9-C8, C4-N9-C1*-O4*, and O5*-C5*-C4*-C3* as a function of time, which do not show significant rotation (predominantly stay as anti conformation).

Arg39, Arg75, Arg287 and Arg610 surround ATP, at the Arginine finger region, which results into the stable bound state. When ATP was pulled, the residues surrounding to it and ATP itself reorients, such that the interactions get maximized. The orientation of guanidine moiety of Arg changes its orientation to facilitate such interactions and a stationary stable phase is formed (Figure 3.4c) in potential of mean force of unbinding process. This process of stabilization by reorientation of Arg residues and ATP are observed from real time trajectory.

3.4   Conclusion

We have performed SMD simulations to pull ATP from the binding site of the protein and the configurations generated while pulling was used for umbrella sampling simulations. The free energy required to pull ATP from the active cleft was computed to be $\sim$ $85 kJmol^{-1}$ ($\pm 5 kJmol^{-1}$). This energy is mainly due to the change in conformation of residues of protein near to the binding site and breaking (and reformation) of hydrogen

bonds between ATP and the helicase. The ATP unbinding process from the binding site was facilitated by application of a constant force of pulling. Therefore, the long time scale (μS) domain motion energy is not accounted in the calculated free energy value. Hence, the value is slightly higher than expected. There is a formation of stable stationary phase, which is a result of H-bond formation and stabilization of interaction between the ATP and the active site residues. This results in the conformational change of ATP and reorientation of the residues. ATP is surrounded with residues in the binding site. When it is pulled, the positive charged residues (Arg) reorient themselves to maximize the interactions. This also leads to the formation of stable stationary phase. The guanidine moiety of Arg, reorients towards the phosphate group of ATP, to facilitate such stationary phase. This study elaborated the atomistic details of the ATP unbinding and the effect of ATP unbinding on local conformational flexibility.

Chapter 4

Domain Motion Studies of PcrA Helicase[1]

4.1 Introduction

Binding of ATP to the PcrA helicase induces the protein to undergo small separation between the domains. The geometrical constraints due to the ATP at active site of protein hinder the conformational flexibility of the protein. Therefore, in previous chapter we have detached the ATP by steered molecular dynamics simulation (applying force) from the binding site and computed the free energy. However, in this chapter we have reported the results base on our investigation on the global conformational flexibility of the protein domains in substrate and product state (after ATP unbinding) of the proteins.

Helicase is crystallized in two different conformations termed as substrate (closed) state complexed with DNA and unhydrolyzable analog of ATP and a product (open) state without ATP. Experimental results have showed that the binding of ATP at active site of the protein transforms it into closed substrate state. Thereafter, hydrolysis of ATP at the catalytic site convert it into a product state which mediate helicase to translocate on DNA strand. As a result of this, helicase moves unidirectionally along single-stranded DNA (ssDNA) [163–165] and opens junctions of duplex DNA. The basis of this mechanism is the conformational changes of PcrA because of ATP binding and hydrolysis. Therefore, we investigated such global conformational changes in the protein and demonstrated the domain motion of helicase protein.

---

[1]This chapter is adapted from the publication Mhashal AR, Choudhury CK and Roy S (2015) Probing the ATP-induced conformational flexibility of the PcrA helicase protein using molecular dynamics simulation. Journal of Molecular Modeling (2016) DOI 10.1007/s00894-016-2922-3

We selected PcrA helicase as model structure from *B. stearothermophilus* which has been crystallized and resolved at high resolution [16, 174], in substrate (with ATP bound) (1QHH and 2PJR) and a product (without ATP/ADP bound)(1PJR and 2PJR) state. In the present work, we used the apo (without DNA) helicase enzyme complexed with ATP (1QHH) and without ATP (1PJR) for the simulations. It is a very simple helicase model composed of four domains (1A, 2A, 1B, and 2B) in their monomeric form. The domains 1A and 2A of this protein are considered to be the functionally important domains which play an vital role in unwinding as reported by the experimental and theoretical investigations [16, 24, 24–26, 162, 166, 169]. These domains form a cleft which serves as ATP-binding site lined with a number of conserved sequence motifs, however, are also involved in the process of translocation. The mode of translocation of the PcrA helicase by inchworm model [16, 23, 24, 166–168]. The model suggests that the binding of ATP at the inter-domain cleft between 1A and 2A facilitate a narrower separation between the domains 1A and 2A which results into closed state. ATP hydrolysis and release from cleft result into a wider separation between these domains which is the product state [20, 25]. A successive ATP binding and its hydrolysis results into the unidirectional translocation of protein.

Therefore, it is expected that protein domains 1A and 2A in product state exhibit more flexibility compared to the ATP bound substrate state. However, flexibility may be restricted in ATP bound state due to the various interactions between ATP and active site residues situated in the inter-domain cleft. Hence, the goal of this chapter is to identify the conformational flexibility of ATP bound substrate state and ATP free product state protein. For this study, we have taken the apo form PcrA helicase enzyme with ATP and without ATP. We refer the systems as ATP bound substrate state (1QHH) and ATP free product state (1PJR). Thereafter, we have investigated the structural properties and the movement of protein domains by performing few hundred nanoseconds of all atomistic MD simulation.

4.2   Computational details

All atomistic MD simulations were performed using GROMACS version 4.5.5 [147–149] [147–149] with amber03 force field [137]. The crystal structure of 1PJR and 1QHH were obtained from the RCSB database (http://www.rcsb.org) [174]. MD simulations of 1QHH and 1PJR were performed separately. The helicase structures were solvated with explicit SPC [178] water molecules. Periodic boundary conditions were used in all the directions. Energy minimization of the starting structures was performed by the steepest descent method [179] as implemented in GROMACS. After minimization, both

the structures 1QHH and 1PJR (excluding water molecules) were positioned restrained with a force constant 1000 kJ mol-1 for 5 ns in isothermal-isobaric (NPT) ensemble. The simulations were performed at 300 K and 1 bar. The v-rescale thermostat [180] with coupling time constant 0.1 ps and Berendsen barostat [181] with coupling time constant of 1 ps were used. The simulation time of 5 ns was enough for water molecules to equilibrate around the protein structure and penetrate to the solvent accessible areas. The position restraints were taken off and it was then followed by the production run simulation in canonical (NVT) ensemble at 300 K. The electrostatic and van der Waals cut-offs were 0.9 nm and 1.4 nm, respectively. Particle Mesh Ewald summation [191] was used for accounting long-range electrostatic interactions. The integration time-step was 2 fs as all bonds were constrained. Independent simulations of both the protein structures were performed for 300 ns with explicit water. 1QHH consisted of 10533 atoms of protein, 43 atoms of ATP and 34945 water molecules and 1PJR system consisted of 10533 atoms of protein and 36843 water molecules. Counter ions (Na+) were added to neutralize the system. The trajectory was recorded at a frequency of 5 ps.

4.3 Results

Prior studies reported that the domains 1A and 2A of PcrA helicase involved in the binding and helicase translocation along the DNA. The translocation of the protein is aided by the binding and hydrolysis of ATP at the protein active site. Domains 1A and 2A of PcrA helicase undergo narrower configuration (less separation between 1A and 2A) upon binding of ATP at the active site. As a result of this protein domains come closer to each other and decreases the distance between domains 1A and 2A. However, after ATP hydrolysis these domains achieve a wider conformation (higher separation) using the free energy released from the ATP hydrolysis. As this protein is crystallized in both ATP bound and ATP free state, we expect that the ATP free protein domains would be more flexible as compared to the ATP bound state. Hence, we have investigated this by calculating the domain displacement as a function of center of mass (CoM) distance between them from the 300 ns production run trajectory of both substrate (1QHH) and product state (1PJR) protein (Figure 4.1). We have schematically shown the CoM distance calculated between domain 1A and 2A in Figure 4.1a. It is observed from figure 4.1b that, 1QHH protein domains have relatively lesser displacement between 1A and 2A and the CoM distance fluctuates around the CoM distance of initial structure with smaller deviation. On the other hand, 1PJR, the ATP free state shows slightly higher fluctuation from the CoM distance. It is then further quantified by calculating the distribution of these CoM distances which is depicted in Figure 4.1c. ATP bound state exhibit higher peak height and lesser width than the ATP free state. This suggests

that the protein is less flexible when it is bound to ATP. In case of 1QHH, the domain distance fluctuates around the distance as observed in the crystal structure [16]. In Figure 4.1d we have plotted the root mean square deviation of the 1QHH and 1PJR from its crystal structure. It is evident that the 1PJR (ATP free state) is fluctuating slightly more than the 1QHH (ATP bound state)

(a)

(b)

(c)

(d)
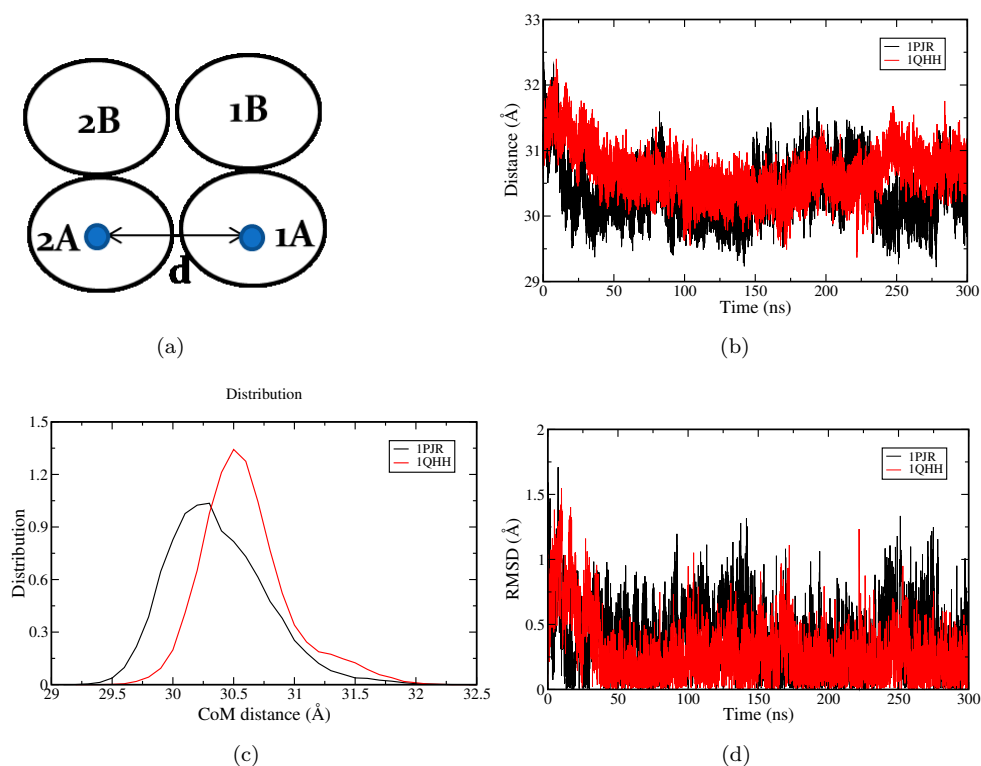
FIGURE 4.1: a) Schematic representation of protein domains and CoM distance, b) CoM distance as a function of time c) distribution of CoM distance and d) root mean sqaure deviation of CoM distance from reference CoM distance value.

In addition to domain displacement, the hinge angle between the two domains was calculated (Figure 4.2). The collective CoM of domains 1B and 2B is used as a hinge point (schematically shown in Figure 4.2a). The angle between the CoM of domain 1A, hinge point and CoM of domain 2A was calculated and plotted in Figure 4.2b. We observe that the hinge angle for 1PJR is fluctuating more as compared to the ATP bound state (1QHH). The domains 1B and 2B were found to have less movement as compared with the domains 1A and 2A, therefore, choice of hinge point is justified.

From Figure 4.2b we observe the decrease of this angle initially for first 35 ns in case of 1PJR, which corresponds to the CoM distance plot in Figure 4.1b. It is clear from both the distance and angle between the domains that existence of significant domain motion in 1PJR. The angle remains fluctuating around a value similar to initial value for 1QHH which also correlates well with CoM distance between between 1A and 2A domains. We have also plotted the distribution of these angles in Figure 4.2c. This shows

that the distribution of the angle values shift to the lower side and distribution curve for 1PJR system exhibits wider distribution compared to 1QHH system. The distribution correlates with the results obtained from the distance plot in Figure 4.1c.

(a)   (b)

(c)
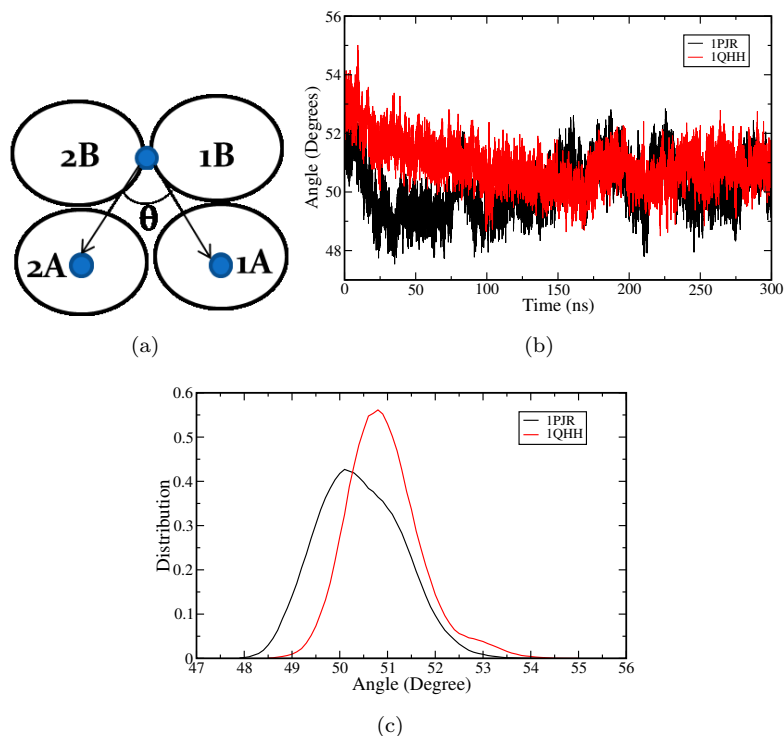
FIGURE 4.2: (a) Schematic representation of domain angle (b) Angle between domains 1A, 1B+2B and 2A as a function of simulation time (c) distribution of angle between domains 1A, 1B+2B and 2A. Colors red and blue represents 1PJR and 1QHH systems respectively.

The inward and outward displacement of domains was investigated by calculating in/out of plane motion of domains. We have calculated the angles that define the outward or inward plane motion of the domains. We have taken a midpoint (mid) along the vectors joining CoM of domain 1B and 2A (Figure 4.3a). Angles ∠mid-1A-2B, and ∠mid-2B-1A were calculated as a function simulation time and plotted for both the system in Figure 4.3b and 4.3c respectively. From the figure it is evident that the angles ∠mid-1A-2B (Figure 4.3b) and ∠mid-2B-1A (Figure 4.3c) gradually decreases for 1QHH and 1PJR as a function of time but from 70 ns onwards the angles become constant. Thus, we do not find any significant in or out plane domain motion either for 1QHH or 1PJR.

Protein is a dynamic entity, which fluctuates in response to the physical and chemical environment. Root mean square displacements (RMSD) of protein atoms with respect to the initial structure can provide the flexibility of the protein in product state and substrate state. Thus, we have calculated and plotted RMSD in Figure 4.4 for PcrA; for backbone atoms and used initial positions (crystal structure) as reference. It is observed that there is a gradual increase in the RMSD for the product state; while for

(a)

(b)

(c)
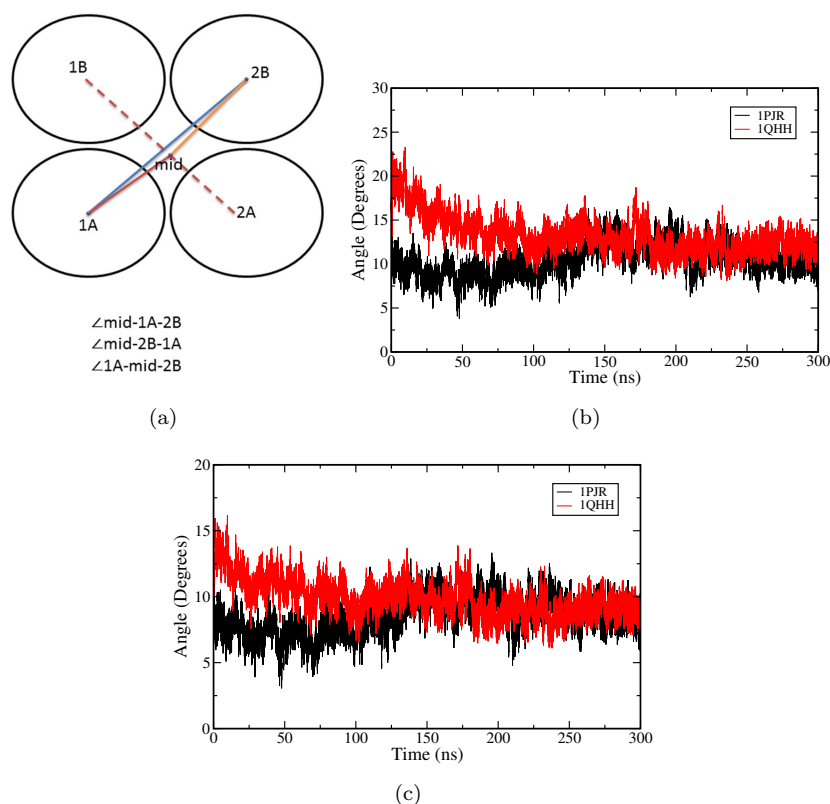
FIGURE 4.3: (a) Schematic representation of the domain plane angles (b) ∠mid-1A-2B and (c) ∠mid-2B-1A. Colors red and blue represents 1PJR and 1QHH system respectively.

the substrate state (1QHH), RMSD values were less than 1PJR. This suggests greater degree of freedom (more flexible) of product state domains than substrate state.
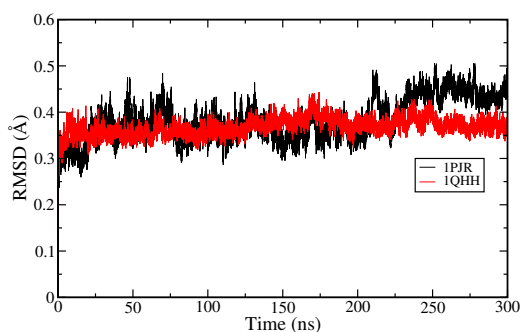
FIGURE 4.4: Root mean square deviation of backbone atoms. Black and blue lines represents systems 1PJR and 1QHH respectively.

Distance between CoM of two domains (1A and 2A) may also change due to changes in the compactness of each domain. It is also probable that one of the domains can deform in a way so that the position of center of mass gets altered. Therefore, to eliminate such chances we have also examined the compactness of each domain by calculating the radius of gyration (Rg) as a function of simulation time. Rg is widely used for elucidation of

structural properties of protein, e.g., protein folding, conformational fluctuations and compactness of the three dimensional structures of proteins. In Figure 4.5a we have depicted distribution of the the Rg for domain 1A and 2A collectively and individually in Figure 4.5b. It can be observed from the collective graph the product state is more flexible than the substrate. However the individual Rg plots for domains 1A and 2A shows almost no change distribution curve. Therefore, we can infer that the domains of the product state are moving towards each other due to absence of ATP in the binding state and then moves to a half closed state.
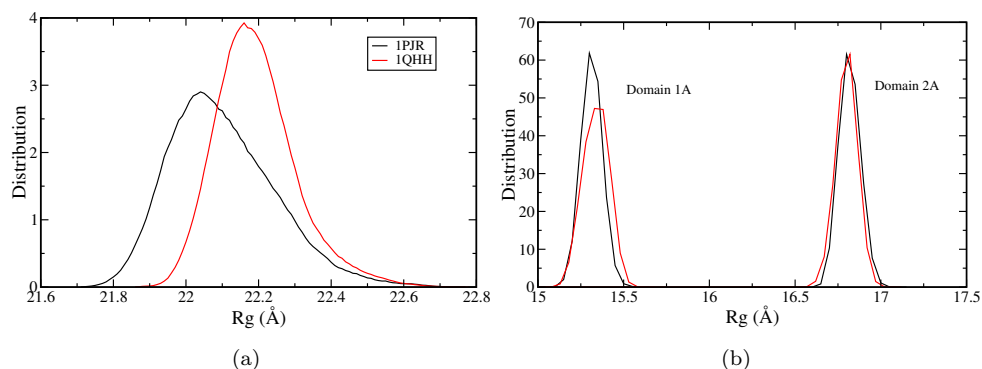
FIGURE 4.5: Distribution of radius of gyration (Rg) for PJR and QHH shown in color black and red respectively b) R(g) distribution of domain 1A and 2A separately. Colors black and red represents 1PJR and 1QHH systems.

We have conducted the principal component analysis (PCA) analysis on the trajectory between 50-200 ns to filter the large-amplitude collective motions from local, fast motions. This was done by building a covariance matrix of the atomic fluctuations followed by the diagonalization of this matrix, which gave a set of eigenvectors and eigenvalues. This describes collective modes of fluctuations of the protein. The eigenvectors corresponding to the largest eigenvalues are called principal components. Finally, we have filtered the original trajectory by projecting it along a selected eigenvector and, we are able to extract the functionally relevant motions from the trajectory. The time scale of investigation, in the present study, is of the order of nanoseconds (300 ns), which is smaller as compared to the Yu *et al.* [25, 26] Thus we are not able to see large scale fluctuations or domain shift. Yu et al. had shown that the domains are much fluctuating for ATP free product state [25]. They have performed a stochastic dynamics simulation on coarse grained systems, and so the time scales accessed by them were large. The 2B subdomain of PcrA helicase also shows significant movement by rotation about a hinge region emerging from the 2A subdomain which was reported earlier [169].

At the smaller time scale, we do find movement in the 1A and 2A domains for 1PJR (ATP free state), analyzed from CoM distance distribution and PCA. This can be extended to

large time scale simulations where we can distinctly visualize the domain motions, as illustrated by Yu et al. [25].

4.4 Conclusions

We have simulated ATP bound substrate state 1QHH and ATP free product state 1PJR structures of PcrA helicase in water. From the calculations, we have shown the displacement of the domains in both with ATP (substrate) and ATP free (product state) using long molecular dynamics trajectories. The results revealed that the domains 1A and 2A show displacement of in absence of ATP i.e. in case of product state. The individual domains of the product state are not flexible, but considerable domain displacement has been observed. However, in case of the substrate state, the geometrical constraints due to the interactions between ATP and active site residues hinder the flexibilty of the domains in substrate state enzyme. The PCA analysis does show the domain motion for 1PJR (ATP free state). This is an indication that after the hydrolysis of ATP, the product state becomes more flexible can attain some domains motion *in vivo* and hence can translocate toward the double stranded fork of the DNA.

DNA unwinding mechanism by helicases is difficult to probe with all atom molecular dynamics simulations. However, we have tried to bridge a small part of mechanism by addressing the local structural change due to the ATP unbinding from the active site of the helicase (in chapter 3) and subsequently its effect on the global conformational flexibility of the motor protein in this chapter using long time all atomistic MD simulations. The time and length scale of motion is limited by the level of theory. However, one can achieve the longer time and larger length scale using different methods e.g. stochastic dynamics or coarse grained simulations but with the lack of atomistic details.

Chapter 5

Effect of Gold Nanoparticle on Membrane Fluidity[1]

5.1   Introduction

The part B of the thesis is essentially focused on the fundamental understanding of the properties of biological membranes and their interactions with the nanoparticles (NPs) and surfaces from the atomic point of view. It is undoubtedly of great biochemical, biophysical, and medical interest. The knowledge of the structural and dynamical behavior of membranes and associated membrane proteins can contribute to the development of pharmaceuticals, anesthetics and drug delivery agents.

The lipid membranes serve as a barrier and selectively allow molecules to the interior of the cell. As the cell is the central part of life, the understanding of the functionality of cell wall, i.e. lipid bilayer membrane under the influence of foreign material is a major challenge in biology. Living bodies are always exposed to the NP of different size, which inevitably leads to experimentation to understand the risk and hazard associated with NPs. Cytotoxic effects of NPs are well known and mostly depend on the size of NPs [192, 193]. Any foreign particles, e.g. NPs, polymers, etc. enter the cell membrane by two different ways, either by endocytosis or by diffusing through the membrane [193, 194], which is vastly dependent on the size of the particle. Computer simulations showed that NPs with small size (2-8 nm) get embedded into the bilayer and it is thermodynamically favorable [195]. On the other hand, the hydrophobic and hydrophilic nature of the NP also plays significant role in the embedding process of NPs in the bilayer. Hydrophilic NPs generally get adsorbed and assembled at the bilayer-water

---

[1]This chapter is adapted from the publication Mhashal AR, Roy S (2014) Effect of Gold Nanoparticle on Structure and Fluidity of Lipid Membrane. PLoS ONE 9(12): e114152.

interface, whereas hydrophobic NPs get accumulated easily in the hydrophobic region of the bilayer, which facilitate higher loading of the NPs in the bilayer. However, the process of insertion of hydrophobic NP in the bilayer is difficult [76, 78]. One more important parameter, in case of penetration, is the charge on the surface of the NPs. Li and Gu [196] studied the adsorption of charged NPs by coarse grained molecular dynamics simulations. They reported that the electrostatic interaction between NP and bilayer facilitates adhesion of the charged NP to the membrane, which induces local transitions in fluid bilayers. The shape of the NP also plays a vital role, which directs the insertion mechanism. Yang *et al.* investigated the physical translocation of NPs with different shapes like spheres, ellipsoids, rods, discs and pushpin-like particles in the lipid bilayer [197]. The study also showed that the volume of the particle plays significant role in penetration process and rotation of particle in the interface complicates the process of insertion. Computer simulations of interaction of graphene [198] and fullerene [199] are also being investigated to understand the translocation process of these low-dimensional systems. Gold nanoparticles (AuNP) are being used as drug delivery agent [37], medical diagnostics [38] and as therapeutic agents [39, 40]. AuNPs are successfully tested as gene delivery agent [41] and in cancer therapy [42]. Small sized hydrophobic AuNP (less than 2nm, coated with dodecanethiol for hydrobhobicity) can enrich hydrophobic areas of lipid bilayer by hydrophobic interactions. Rasch *et al.* [200] has explained how this enrichment of capped hydrophobic AuNP occurs in the bilayer. The hydrophobic NPs can unzip the lipid bilayers and get loaded in the hydrophobic part of the membrane. The loading of NPs in bilayer can change in the phase diagram of a lipid bilayer. Bothum [201] showed experimentally that augmentation of decanethiol-capped AuNPs into liposomal membrane decreases the melting temperature at high concentration of NPs. Similarly Sung-Sik Han *et al.* [202] also showed entrapped silver NPs in 1,2-dipalmitoyl-sn-glycerol-3-phosphocholine (DPPC) liposome fluidifies the membrane, which might be because of interactions between the DPPC lipid molecules and silver NPs. To understand the interactions between NP and lipid molecules, molecular dynamics (MD) simulation of a coarse grained model of AuNP and model lipid membrane was performed by Zheng *et al.* [91]. They observed coarse grained NPs of size 2.2 nm with different signs of the charges and densities of surface charge naturally adsorb to the model bilayer surface or penetrate into the bilayer. However, all the experimental and theoretical studies mentioned above are mostly deal with the local interactions of the NP with the bilayer molecules and thereby penetration mechanism of the particles in the bilayer. The missing link to all these investigations is the effect of the NPs on the lipid molecules, which are not directly interacting with the NPs. In this present study, we aim to simulate neutral AuNPs of different size with lipid bilayer using all atomistic MD to address the effect of non-passivated NP on the lipid molecules (which are not directly interacting) for the first time to the best of our knowledge. In this work we intend to understand the

effect non-passivated NP, however, most of the work on AuNP has been carried out by surface capping agents. These surface passivating agents then change the chemical nature of the AuNP. Merga *et al.* recently synthesized naked AuNP by reducing Au2O3 by molecular hydrogen [203]. Zopes *et al.* synthesized small size naked AuNP by hydrolysis of Gold complex [NMe4][Au(CF3)2] [204]. Caprile *et al.* studied the interaction of naked AuNP with L-cysteine using high resolution XPS [205]. Therefore, interaction of non-passivated AuNP with lipid bilayer is an important aspect to address from molecular level simulation. We have considered bilayer made of lipids with unsaturation in one of the aliphatic tail because of the higher fluidity in a such assembled membrane. Therefore, possibly, the change in magnitude of the fluidity of such membrane interacting with AuNP will be higher than bilayer composed of saturated lipid molecules. The fluidity in membrane is directly related to the structural arrangement of the lipid molecules. However, this structural arrangement of lipid may differ for adjacent to and far from the NP adsorption site (interaction site). Therefore, we have correlated fluidity in different parts of membrane (adjacent and far from the NP) to the ordering of the lipids. Apart from fluidity, we have also analyzed the local structure of lipids near to AuNPs, the diffusivity of lipid molecules in presence of AuNP and densities of water around AuNP, which has deeply penetrated the bilayer.

5.2   Computational method

We have performed all atomistic MD simulations of 1-arachidonyl-2-oleoyl-sn-glycero3-phosphocholine (AOPC) with different size of AuNPs separately. To set up the simulations, we have used three consecutive processes, which includes a) self-assembly of lipid, b) construction of AuNP followed by its simulation in vacuum and water c) simulation of self-assembled lipid and AuNP systems.

5.2.1   Self-assembly of lipid

Poger D. *et al.* [206] studied the lipid model with mixed acid phosphatidylcholine (PC) and developed parameter sets for various such lipid molecules. In the present study, we have used a united atom model of AOPC (the structure of AOPC is shown in Figure 5.1) extracted from the parameter set for PC [206].

The lipid model system contains monounsaturated oleoyl (18 Carbon atoms in aliphatic chain) with slightly longer saturated arachidoyl (20 Carbon atoms in aliphatic chain, Figure 5.1). It is experimentally shown that lipid rafts with one saturated fatty acid chains are involved in signaling [207] and transport of molecules [208]. It is also found
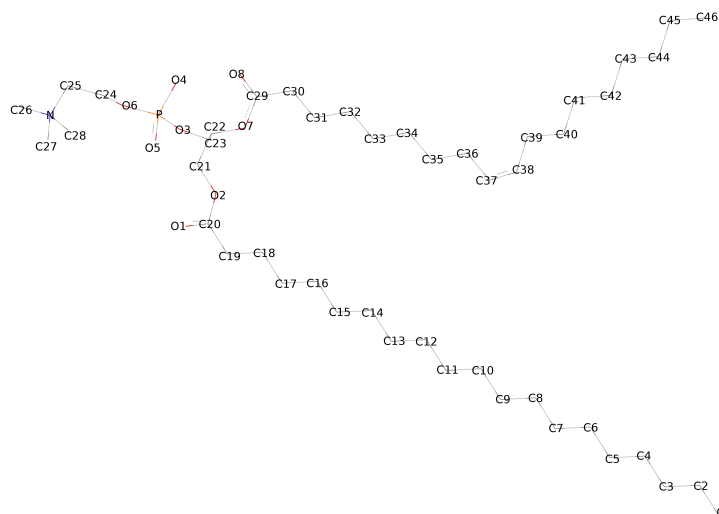
FIGURE 5.1: Chemical structure of the AOPC lipid.

that raft phospholipids contain longer saturated fatty acid chains [209, 210] e.g., palmitic, stearic, and arachidic acid when compared to unsaturated fatty acids. We have performed self-assembly simulation of AOPC lipids starting from 128 randomly distributed AOPC molecules in water. We have used SPC water model [178] for all the simulations. The simulations were performed using the GROMACS 4.5.1 [147, 211] MD code. Isobaric-isothermal (NPT) ensemble with periodic boundary conditions (PBC) was used for simulations. Phase transition temperature of AOPC is 284.9K [212]. Therefore, we have used 300K and 1 bar pressure for self-assembly simulation. Temperature coupling was used with v-rescale algorithm [180] with a coupling constant of 0.1 ps. The isotropic pressure coupling was applied by using Berendsen barostat [181] only for the self-assembly simulation. The pressure coupling time constant was 2.0 ps in order to maintain a constant pressure of 1.0 bar. Bonds were constrained with LINCS algorithm. The Lennard-Jones interactions were taken care with cut-off of 1.4 nm. For electrostatic interactions Particle-Mesh Ewald (PME) [146] method was used with a cut-off of 1.4 nm. After 50 ns of MD simulation, we have obtained the self-assembled bilayer of AOPC.

5.2.2 Construction of AuNP

The initial structures of AuNPs were constructed from fcc lattice of Gold. In crystalline lattice the center of the NP was set on a Gold atom, then a radius 1 nm, 1.75 nm and 2.5 nm was considered. Gold atoms fall into this radius were taken as part of NPs of different sizes of diameter 2 nm (2nm_AuNP), 3.5 nm (3.5nm_AuNP) and 5 nm (5nm_AuNP). The initial structures of AuNP are shown in Figure 5.2. These AuNPs were further energy optimized and subjected to MD simulation in vacuum and in water for 5 ns to

check the stability and structural relaxation. Gold atoms in the NP interact only via Lennard-Jones (LJ) potential.
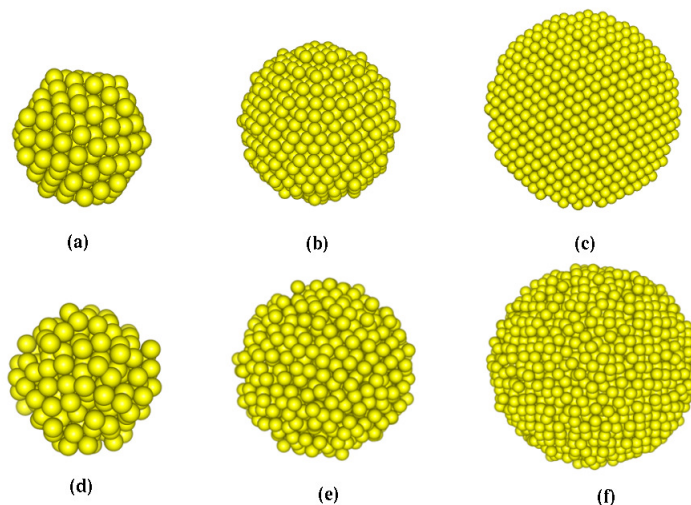
FIGURE 5.2: Initial and final structures of AuNP (a,d) 2nm_AuNP,(b,e) 3.5nm_AuNP and (c,f) 5nm_AuNP respectively.

These LJ parameters are obtained from the paper of Heinz *et al.* [213]. The parameters suggest that the AuNPs are hydrophilic is nature. The final snapshots after 5 ns of MD run of NP in water are shown in Figure 5.2. Distance distribution plots for Gold atoms in a vacuum and water from last 1 ns of MD trajectories are shown in Figure 5.3. The structures of the NP were retained intact and stable throughout the simulations (see Figure 5.4a). In Figure 5.4b, the radial distribution function (RDF) between Gold and Oxygen atom of water shows the hydrophilic nature of AuNP. As the head-group of lipid membrane is hydrophilic, it is expected that hydrophilic AuNP will interact favorably with the lipid head-groups. Note that in the present study, AuNPs do not possess any charges on the surface.

5.2.3   Lipid-nanoparticle system

We aim to study the interaction of AuNP with AOPC lipid bilayer and its effects on the bilayer properties, therefore, we have assembled the NPs of different sizes on the surface of the bilayer and constructed following three systems. The smallest sized NP 2nm_AuNP was placed initially on the self-assembled AOPC bilayer of 128 molecules ($\tilde{6}4$ molecules on each leaflet). For the second and third system with 3.5nm_AuNP and 5nm_AuNP particles, we have replicated the above bilayer in x and y direction (in each
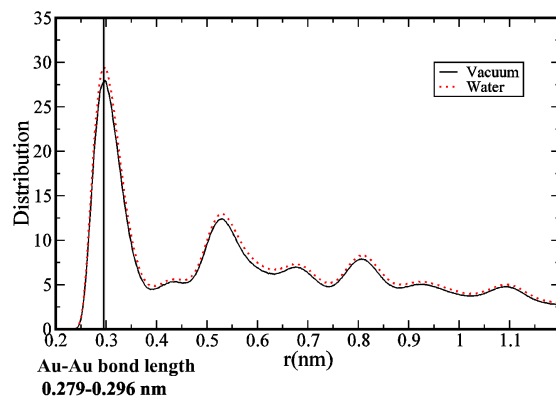
FIGURE 5.3: Distance distribution between Gold atoms in water and in vacuum. Black and red line shows Au-Au distance distribution in vacuum and water respectively.
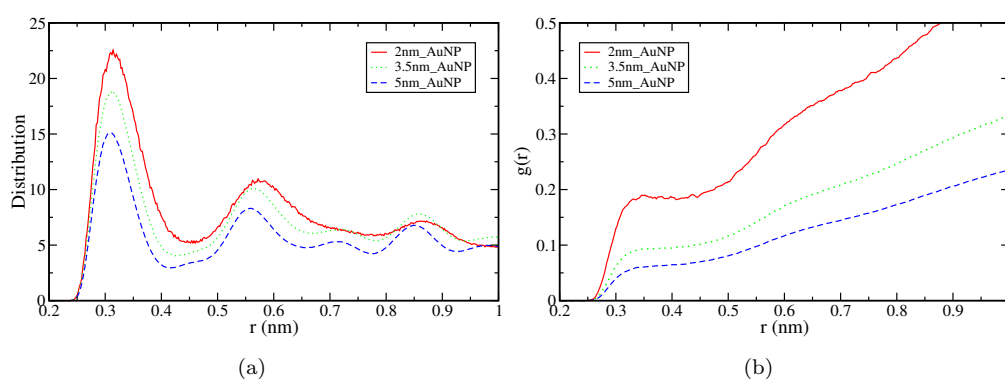
FIGURE 5.4: (a) Distance distribution between Gold-Gold atoms and (b) RDF between Gold and Oxygen atoms of water. Colors red, green and blue represents 2nm_AuNP, 3.5nm_AuNP and 5nm_AuNP systems.

bilayer direction). Before placing the AuNP, the replicated bilayer was subjected to equilibration run for 10 ns. Thereafter, the NPs were placed on the surface of the leaflet of bilayer (in water phase) in such a way that surface atoms of both NP and lipids fall in the range of van der Waals cut-off. The non-bonded interactions between the AuNP atoms and bilayer atoms are calculated by using the combination rule of geometric mean for all C(6) and C(12) parameters. To compare the effects of NP on bilayer, we have also simulated AOPC bilayer of 512 lipid molecules without a NP for 100 ns and termed as reference lipid bilayer. The snapshots of self-assembled bilayer with 128 lipid molecules and a replicated bilayer with 512 lipid molecules without AuNP are shown in Figure 5.5.

All the three systems described above with AuNP in their initial positions are depicted in Figure 5.6a, b, and c and the number of atoms of each component, i.e., Gold, AOPC and water, and equilibrated simulation box size are given in Table 5.1. These systems were solvated with SPC water [178] and simulated for 100 ns with semi-isotropic pressure coupling using Berendsen barostat [181] with separate coupling to xy-plane and z-direction (the bilayer normal).
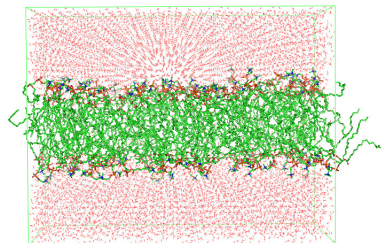
(a)
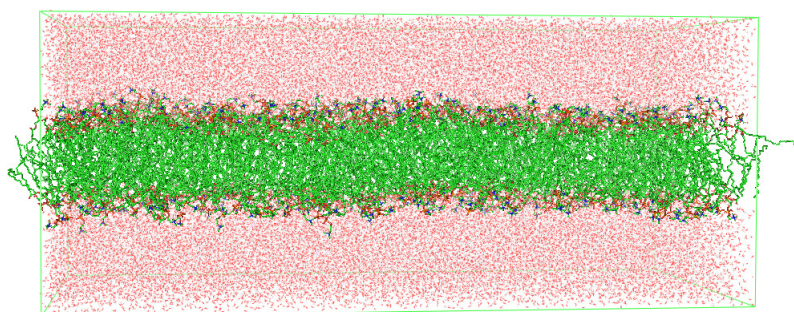
(b)

FIGURE 5.5: Snapshots of AOPC lipid bilayer after equilibration run (a) 128 AOPC lipid system,(b) 512 AOPC lipid system.

The remaining parameters for MD were kept same as used in self-assembly simulation. The simulation trajectories were written after each 5 ps and used for analysis. In this work we have analyzed the effects of NP on membrane in two different regions; near to the adhesion (interacting) site and away from the interacting site. Therefore, we have divided the membrane based on the distance from NP to the lipid molecules in interacting leaflet only. As we have used short range cut-off of 1.4 nm, we have considered the interacting short range (SR) lipid molecules (coordinates of head group Nitrogen atoms) which fall into the distance of 1.5 nm + radius of NP (r). E.g., for 2nm_AuNP the interacting lipid molecules are those, which fall into the distance of 2.5 nm from the center of mass (CoM) of AuNP. To understand the indirect effect of NP on bilayer; we have considered a region, which is away from interacting short ranged lipid molecules as defined above. As SR lipids can diffuse with time, therefore, to get rid of hard boundary

TABLE 5.1: Details of the bilayer NP systems.

System	Gold (Au)	AOPC (Molecules)	AOPC(atoms)	water	System size	Simulation box (nm)		
						X	Y	Z
Reference	0	512	28672	48949	175519	22.06	11.13	9.09
2nm_AuNP	249	128	7168	11008	40441	11.01	5.55	8.52
3.5nm_AuNP	1289	512	28672	76619	259818	22.32	11.16	12.5
5nm_AuNP	3926	512	28672	89681	301640	22.38	11.19	14.3
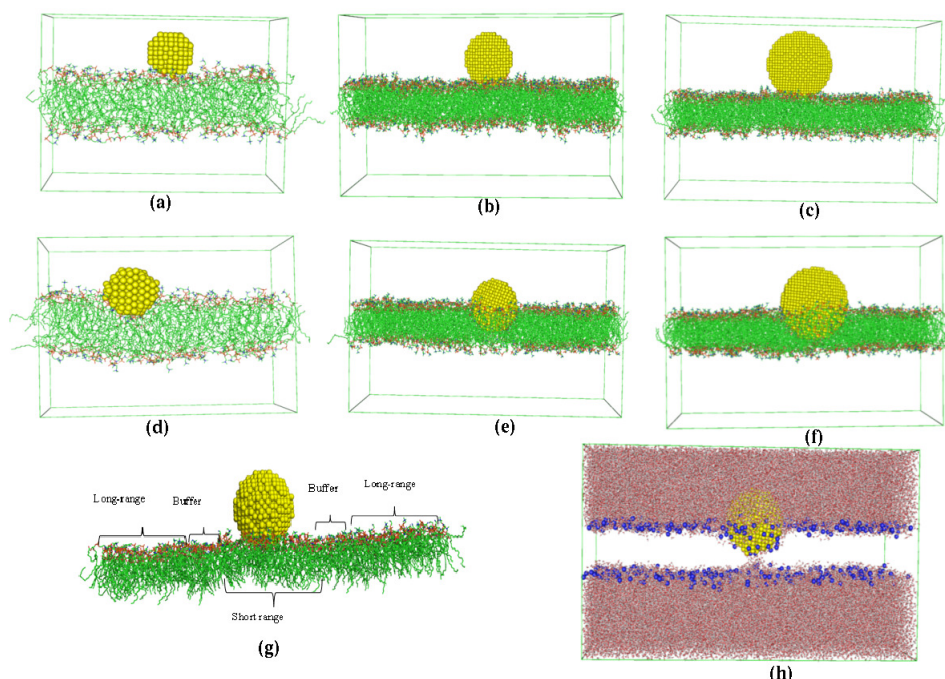
FIGURE 5.6: Initial and final snapshots after 100 ns MD simulation of three systems. (a,d) 2nm_AuNP (b,e) 3.5nm_AuNP (c,f) 5nm_AuNP. (g) shematic representation of short range(SR), long range (LR) and buffer region. (h) snapshot of 3.5nm_AuNP system with explicitely represented head-group atoms in blue color.

between SR molecules and rest of lipid molecules, we have defined a region as a buffer. The lipid molecules fall in between distance greater than (r+1.5 nm) and less than (r+ 1.5 nm + 0.5 nm) are taken as buffer region lipid molecules and are not considered in any analysis. The rest of the lipid molecules in the same leaflet, which are at a distance greater, than (r+ 1.5 nm + 0.5 nm) are not directly interacting with AuNP, are termed as long range (LR) lipid molecules (Figure 5.6g). As lipid molecules (and AuNP) are dynamic in nature, we have updated these boundaries (between SR buffer and buffer LR region) every 10 ns and tagged the lipid molecules of these respective regions for further analysis. To calculate the properties of long range molecules we have considered the sufficiently large system with 512 lipid molecules which gives a total of 301640 atoms (for details see Table 5.1) including water and NP. For all analysis we have used lipid molecules from interacting (with AuNP) leaflet. Schematically we have shown SR, LR

and buffer molecules in the bilayer in Figure 5.6g, and the number of the lipids falls into respective regions is shown in Table 5.2. All the analysis programs are discussed along with the results and discussions.

TABLE 5.2: Number of lipids in SR, buffer and LR region.

System	SR lipids	Buffer lipids	LR lipids
2nm_AuNP	~ 16	~ 10	~ 46
3.5nm_AuNP	~ 44	~ 10	~ 218
5nm_AuNP	~ 62	~ 10	~ 198

5.3   Results and discussions

5.3.1   Structural properties of interacting molecules with AuNP

Four systems, including the reference system (without AuNP) are structurally characterized to see the position of the NP as a function of time. The snapshots of the systems as a function of time (0 ns, 25 ns, 50 ns, 75 ns and 100 ns) are given in Figure 5.7.
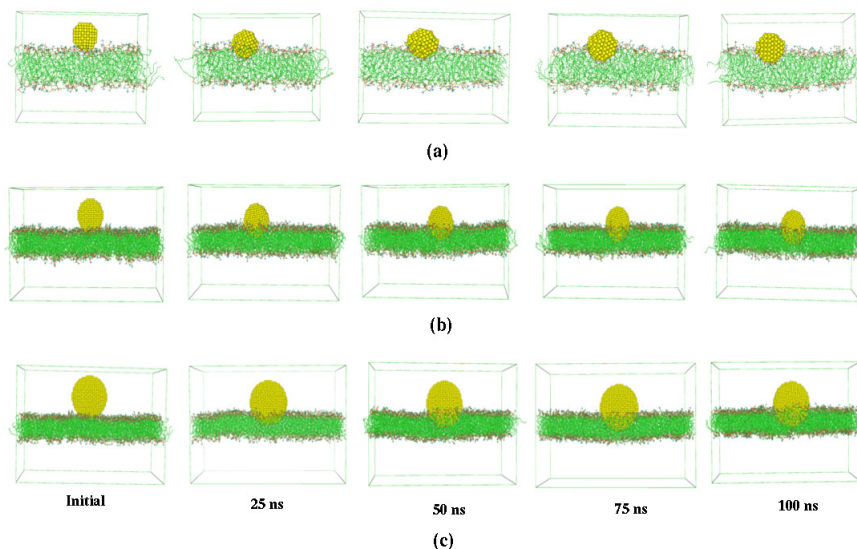
FIGURE 5.7: The snapshots of the systems (a) 2nm_AuNP, (b) 3.5nm_AuNP and (c) 5nm_AuNP as a function of time (0 ns, 25 ns, 50 ns, 75 ns and 100 ns).

From the snapshots at 100 ns in Figure 5.6d, e, f (intermediate snapshots at Figure 5.7) it is evident that the AuNP of different sizes gets adsorbed on the bilayer surface

and penetrates deeper in the bilayer along with some of the head groups of the lipid molecules (Figure 5.6h). From partial density plots (Figure 5.8), it is clear that the head group nitrogen atoms penetrate deep into the bilayer along with AuNP. However, the nanoparticle it stays in contact with the lipid headroups and the interface water molecules.
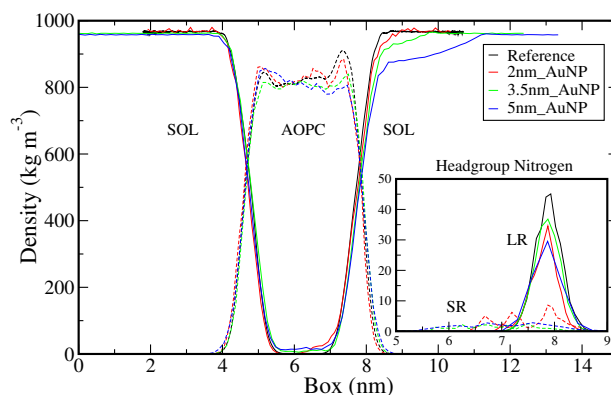
FIGURE 5.8: Partial densities of water and AOPC. Dotted lines represents lipid and solid lines represents the water partial densities. Black, red, green and blue line respresents reference, 2nm_AuNP, 3.5nm_AuNP and 5nm_AuNP systems respectively. Figure inset represents partial densities of head-group Nitrogen atoms of SR and LR lipid interacting monolayer where dotted lines shows SR lipids and solid lines are LR lipids

In Figure 5.8 (inset) nitrogen densities of interacting SR and LR lipids are shown separately, which shows that, the densities of SR molecules are spread deep into the bilayer. However, the Nitrogen atoms of LR lipids are at the same initial position similar to reference bilayer system. In Figure 5.6h, we have shown the snapshot of 3.5nm_AuNP system only with head group Nitrogen atoms of lipids. From partial densities of bilayer systems (see Figure 5.8), it is evident that water is also penetrating along with the AuNP of different sizes. The water molecules and head group atoms of lipids interact with the AuNP because of the hydrophilic nature of NPs. To quantify this, we have calculated distance distributions between lipid head group atoms (of interacting leaflet) and interacting surface Gold atoms of AuNP and illustrated in Figure 5.9. We have considered the Gold atoms in each frame which are at the surface of the NP and in the vicinity of lipid molecules to calculate the distance distribution. These distributions are further normalized by number of interacting atoms of the lipid head groups. Distance distribution between head-groups non-ester phosphate Oxygen atoms (O4 and O5) and Gold atoms shows the higher peak height (3c) than other two atoms (Nitrogen and Carbon, Figure 5.9a and b) which confirms the head-groups non-bridging (non-ester) Oxygen atoms are more ordered near to the AuNP surface. In Figure 5.10, we have depicted separately the distance distribution between AuNP surface Gold atom and all phosphate Oxygen atoms (O3 and O6 for bridging, O4 and O5 double bonded) which show higher ordering of double bonded Oxygen atoms near AuNP surface.
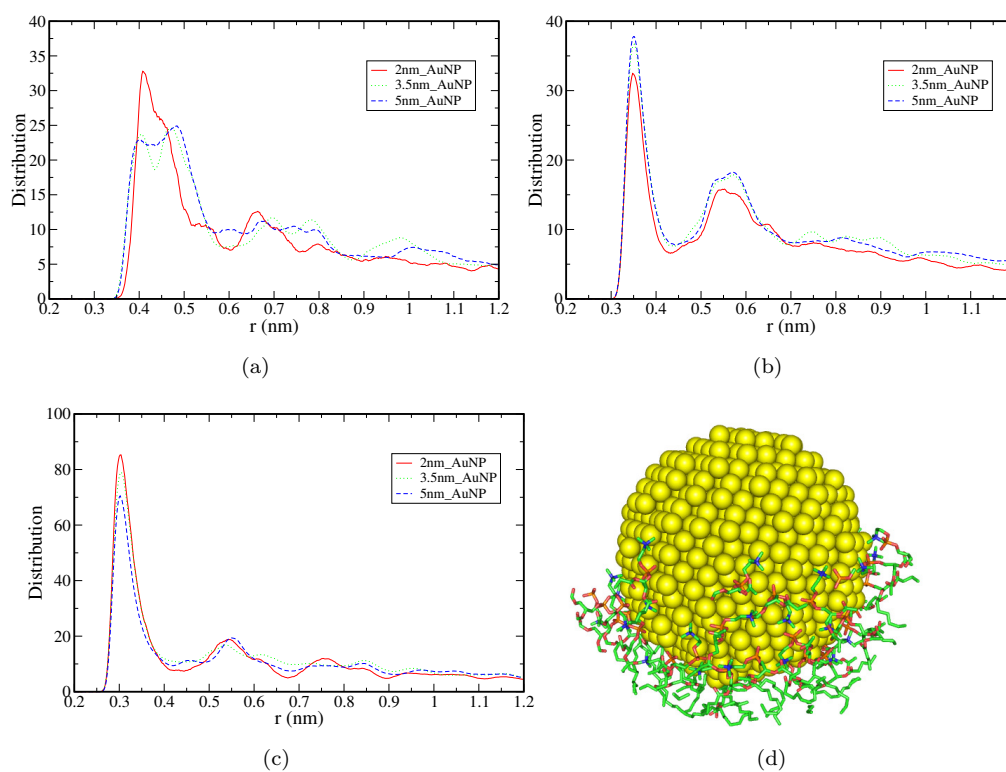
FIGURE 5.9: Distance distribution between surface Gold atoms of AuNP and (a) headgroup Nitrogen, (b) NMe group's C atoms and (c) non-ester Oxygens of Phosphate group respectively. d) Snapshot of lipid headgroup interaction with AuNP.
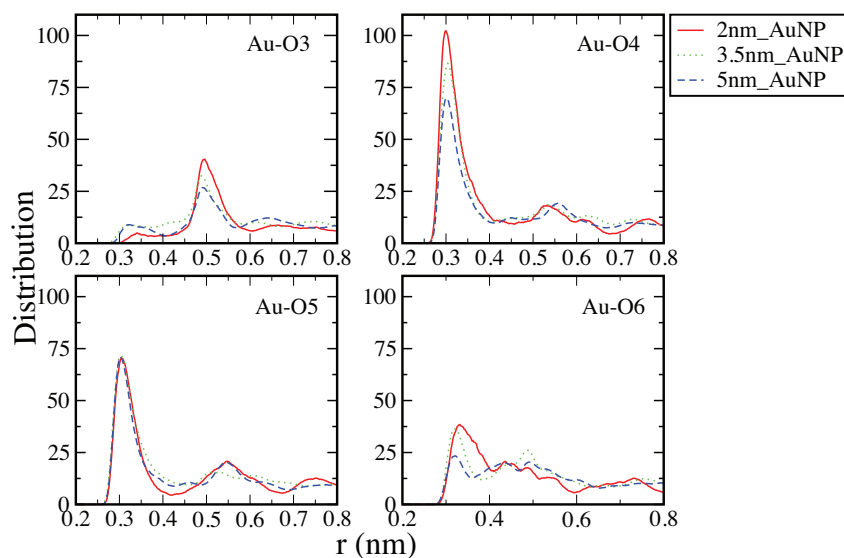
FIGURE 5.10: Distance distribution between AuNP surface Gold and Phosphate Oxygen atoms separately.

From Figure 5.9a and b, it is evident that the Nitrogen and N-methyl Carbon atoms have smaller peak height, hence less ordering than Oxygen atoms. From Figure 5.9, it is also clear that the size of the NP has no effect on the ordering of lipid atoms near the surface of AuNP. In Figure 5.9d we have shown a snapshot of 3.5nm_AuNP along with interacting lipid head group atoms for which we have plotted the distance distribution.

As we have observed the water molecules also penetrated the bilayer along with AuNP, we have quantified the water density near to the AuNP. Two dimensional density map of water is calculated and presented in Figure 5.11. From the densities of water near different sized NPs we have observed that water penetrates into the lipid bilayer along with Gold atoms. The density of water around the AuNP inside the bilayer is much less than the interfacial water density. It is also evident from the Figure 5.11 that the water molecules, which enter the bilayer region along with AuNP remain discontinuous i.e., the water molecules are clustered near the AuNP surface. A snapshot representing this water cluster is shown in Figure 5.11d. The two dimensional density calculated here is an average from last 10 ns of 100 ns trajectory. To our surprise the water clusters formed near the AuNP surface inside the bilayer region do not change its position and therefore shows discontinuity in the density profile. This provides a fact that, there is a clear competition between water oxygen and lipid head group atoms to interact with the hydrophilic AuNP. Therefore, only few water molecules penetrate the bilayer along with Gold atoms and get stabilized locally with the Gold surface atoms. Different sized Gold NP has no effect in altering the local structure and the density of water around the AuNP (Figure 5.11a, b and c).

5.3.2 Comparison of structural and dynamical properties of short and long range lipids

It is obvious that the lipid molecules, which are interacting with AuNP will get affected the most and structural and dynamical properties of the lipid molecules will get altered. However the LR lipid molecules, which are much away from the adhesion site, also may get affected due to the indirect effect from the perturbation caused by AuNP. The different sizes of AuNP also may cause alteration in properties with different magnitude. Therefore, to understand the effect of NP, we have calculated structural and dynamical properties of the lipid molecules and compared with the reference lipid system. To understand the effect of perturbation of AuNP on lipid molecules, we have calculated separately the structural properties of the head-groups and aliphatic tails of short (SR) and long range (LR) lipids independently and compared with the reference lipid bilayer system (without AuNP).
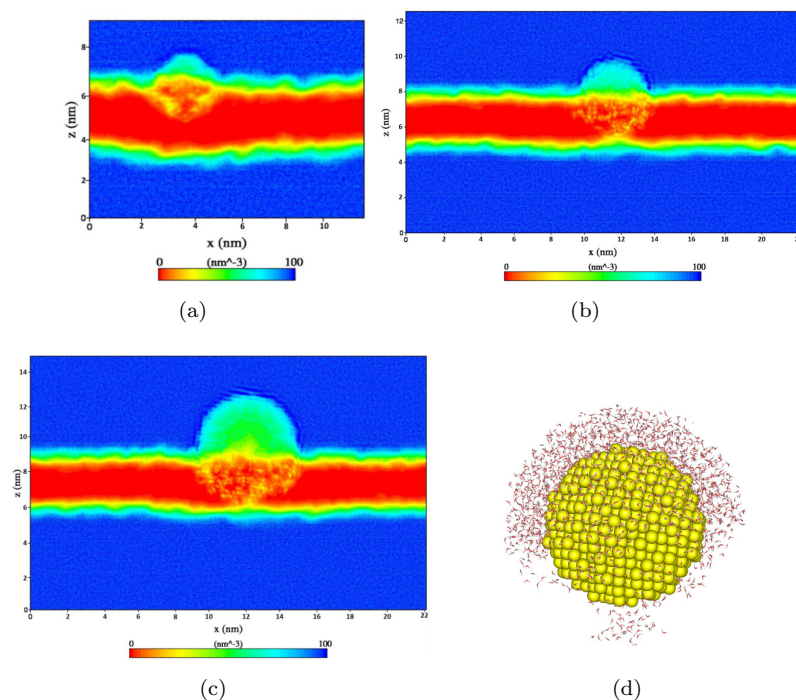
FIGURE 5.11: Two dimensional density map of water (a), (b), and (c) represents systems 2nm_AuNP, 3.5nm_AuNP and $5nm\_AuNP$ respectively (d) schematic respresentation of water density around AuNP upto certain cut-off (bilayer not shown).
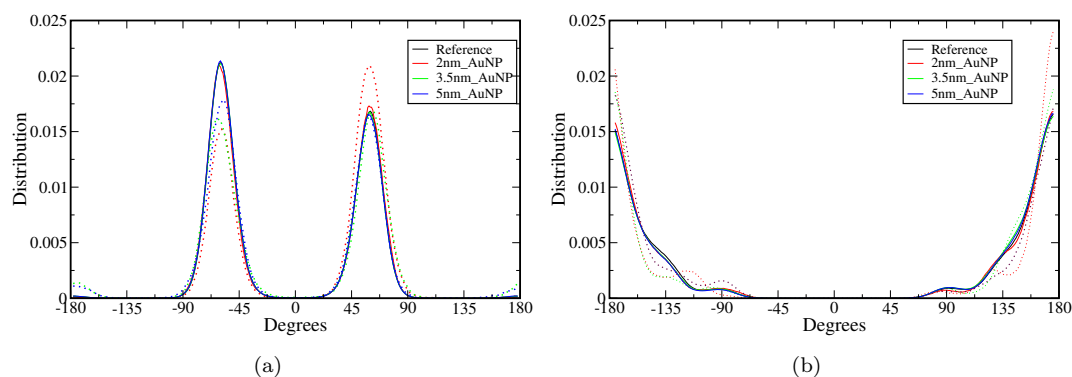
FIGURE 5.12: Dihedral angle distribution of the head-group atoms (a) N-C25-C24-O6 (b) C25-C24-O6-P. Dotted and solid lines are for SR and LR lipid molecules.

The hydrophilic AuNP shows higher interaction with the hydrophilic atoms of the head-group of lipid molecules. Because of this interaction, the dihedrals between the head-group atoms can get altered. Therefore, we have calculated and compared the dihedral angle distribution of head-group atoms (N-C25-C24-O6 and C25-C24-O6-P) of SR and LR lipids (Figure 5.12a, b). The deviation in the dihedral angle distribution is observed for SR molecules. C25-C24-O6-P dihedral (Figure 5.12b) shows changes in peak position. This is may be because of higher interaction of Gold surface with the head group Oxygen atom, which is observed from the distance distributions (see Figure 5.9). However, LR molecules show the same distribution as reference bilayer

system. Similarly, we have calculated angle distributions between the head group atoms N-C25-C24, C25-C24-O6 and C24-O6-P from last 10 ns of 100 ns trajectory. There is not much difference in angles between adjacent atoms of head-group of SR and LR lipid molecules. The results are given in Figure 5.13.
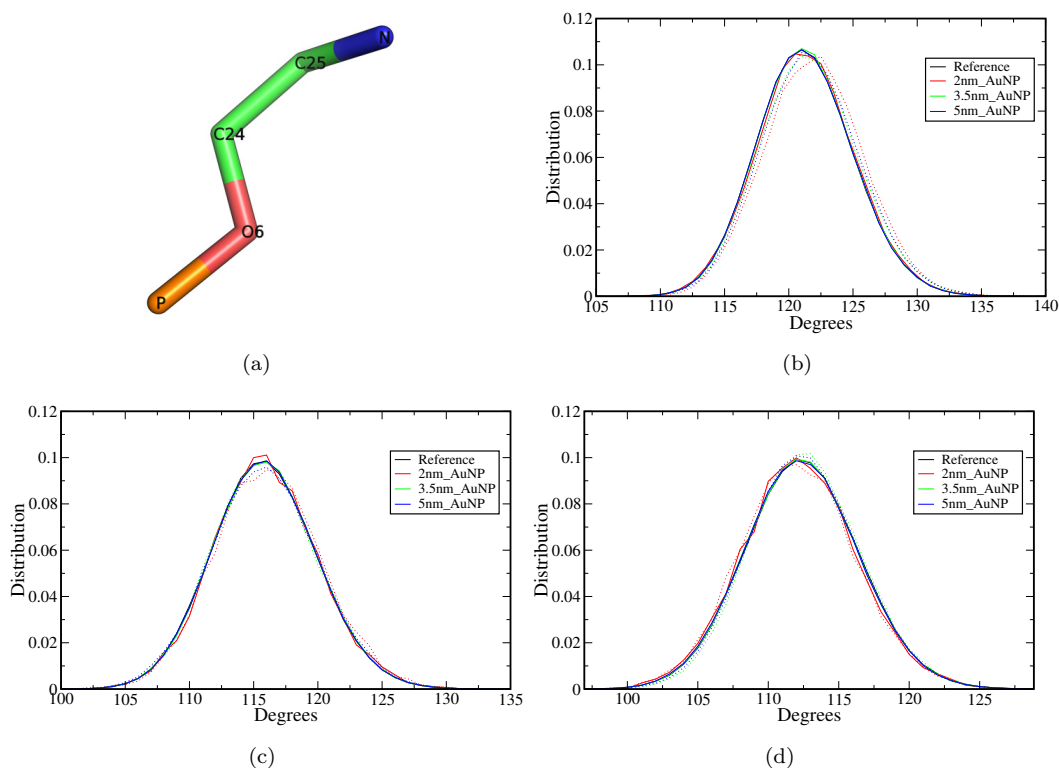
FIGURE 5.13: (a) Head-group atoms. Angle distribution of the head-group atoms (b) N-C25-C24 (c) C25-C24-O6 and (d) C24-O6-P.

The interacting atoms of SR lipids (with NP) like Nitrogen and Oxygen shows a slight deviation in angle with neighboring atoms compared to LR molecules. We do not observe significant differences in the angle between head-group atoms for different size of AuNPs. The predefined parameters for angle (force constant) for harmonic angle potentials result in large bonded interaction between atoms of angles, which does not get affected due to much weaker interaction caused by favorable van der Waals or electrostatics. Therefore, we do not see much of difference in angle of head-group atoms of SR lipid molecules. It is reported in the literature that a small perturbation to the bilayer can change the fluidity of the bilayer [201, 202, 214]. The fluidity of a bilayer is often related to the structural ordering of the lipid molecules and in this case it is mainly aliphatic tails of the lipids. The orientational order parameter $-S_{cd}$ is an amount that provides how well a molecule

lines up with the bilayer normal, and it is given by the equation below,

$$-S_{cd} = \frac{2}{3}S_{xx} + \frac{1}{3}S_{yy}$$

$$-S_{\alpha\beta} = \frac{1}{2}\langle\overline{3cos\theta_\alpha cos\theta_\beta - \delta_{\alpha\beta}}\rangle \quad \alpha,\beta = x,y,z \qquad (5.1)$$

$$cos\theta_\alpha = \hat{e_\alpha}.\hat{e_k}$$

where $\hat{e}k$ is the bilayer normal vector, $\hat{e}x$ is a unit vector perpendicular to vector $e_{i,i+2}$, $e_{i,i+2}$ is the unit vector from A_i to A_{i+2} which is contained in the plane formed by the $i, i+1, i+2$ particles, θ_x is the angle between $\hat{e}k$ and $\hat{e}x$, and θ_y is the angle between $\hat{e}k$ and the unit $\hat{e}y$ which is perpendicular to the plane formed by the $i, i+1, i+2$ particles. A value of 0.5 indicates a perfectly ordered acyl chains whereas; the value 0 denotes random/unordered alignment. In general, order decreases from the interface region to the bilayer center. The order parameter is also related to the tilt angle of the acyl chain with respect to the bilayer normal and gives indirect distribution of dihedral angles of the chain. So with the increase in the order parameter (-S_{cd}) the trans conformation increase and tilt angle decrease. Figure 5.14a and b illustrates the order parameter -S_{cd} for *sn1* and *sn2* chains of lipid as a function of carbon atom number (same number used as in Figure 5.1). In our simulations, we have used lipid molecules with one saturated (*sn1*) and other unsaturated (*sn2*) aliphatic chain (C37-C38 refer Figure 5.1). The order parameters are calculated for carbon atoms C17 to C2 of *sn1* chain and C31 to C45 of *sn2* chain (Figure 5.1). The unsaturation introduces a kink in the hydrocarbon chain (*sn2*) therefore a sharp fall in parameter values is observed(Figure 5.14b).
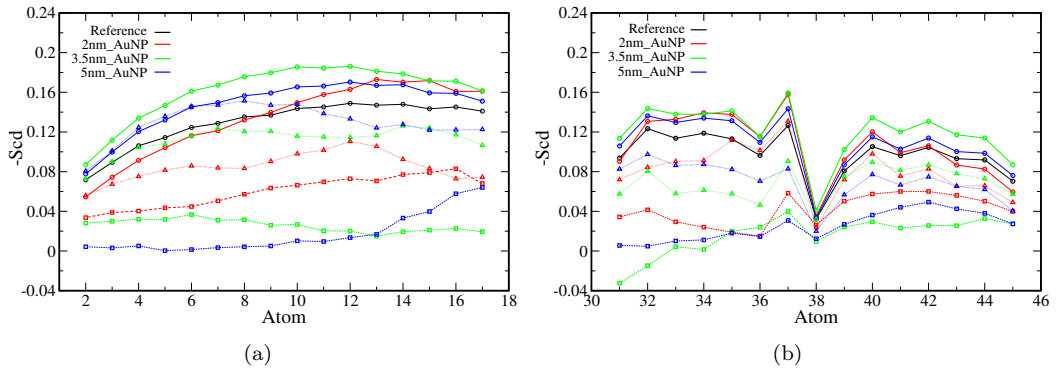
FIGURE 5.14: $-S_{cd}$ order parameters of chains (a) *sn1* and (b) *sn2*. Symbols sqaure (dashed lines), triangle (dotted lines) and circle (solid lines) represents short range, buffer region and long range lipids respectively.

From Figure 5.14 it is evident that carbon atoms, which are located near to the head-group (C17-C8) of *sn1* chain, are more ordered than *sn2* chain of LR lipid molecules. The carbon atom of end-group of tails of *sn1* and *sn2* chains shows less ordering because of their higher flexibility. Hence the bilayers, which are perturbed by different sizes of

AuNP show more ordering of LR lipid tails than the reference bilayer. The lipids at buffer region are ordered compared to the SR region, however, not as ordered as LR region. The ordering of *sn1* and *sn2* tails of SR lipid molecules is much less than the LR lipids and a reference bilayer system. So it is evident that the AuNP not only affects the lipid molecules in the vicinity, but also causes changes in structural properties of the lipid molecules far from the adhesion site. The observed enhancement of structural ordering of lipid tails can cause decrease in area per head group and increase the bilayer thickness.
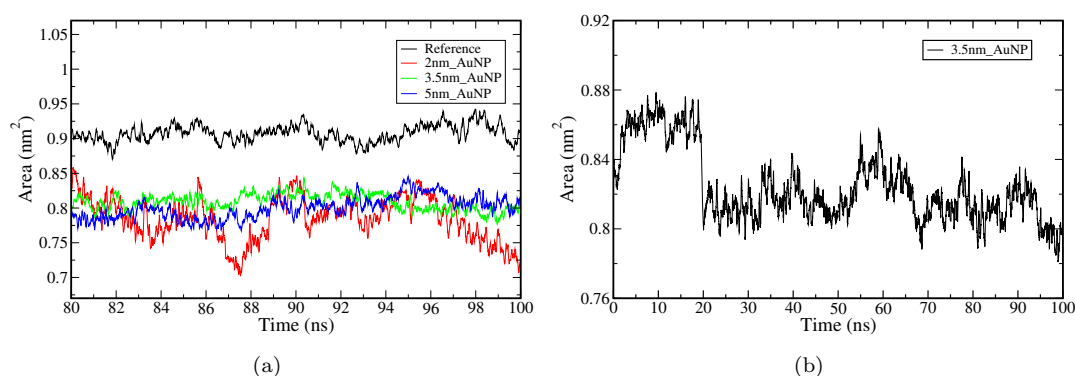
FIGURE 5.15: (a) Area per head-group of LR lipids and (b) Area per head group for LR lipid molecules as function of time for 3.5nm_AuNP system.

However, the effect can be seen in the region where LR lipid molecules are present. Therefore, we have computed the area per lipid of LR molecules. It is calculated by subtracting the area of SR molecules, including the buffer region from the total area of the box in a bilayer plane. Thereafter, this area is divided by the number of lipid molecules present in the interacting leaflet in LR region and represented in Figure 5.15a as a function of time (last 20 ns of 100 ns). We have observed for all the cases there is a slight decrease $(6 - 7\%)$ in area per head group of the LR lipid molecules. In Figure 5.15b, we have shown the transition of the area per head group as a function of time starting from 0 ns.

This gives the direct evidence that the AuNP after getting inserted enough in the bilayer the area per head groups for the LR molecules get altered. The lipid order parameters, area per lipid and the bilayer thickness are the inter-related properties, as one can expect the enhanced lipid ordering can increase the bilayer thickness due to higher lipid packing. Therefore, to check this, we have calculated the bilayer thickness. It is carried out by dividing the simulation box in 50x50 grids using GridMAT-MD algorithm developed for bilayer analysis [215]. In each grid we have calculated the distances between nitrogen atoms of two leaflets and averaged it. Then the normalized distribution of the bilayer thickness is calculated from each grid for the LR lipid region and plotted in Figure 5.16a. The distribution of bilayer thickness for the SR lipid region is given in Figure 5.16b.
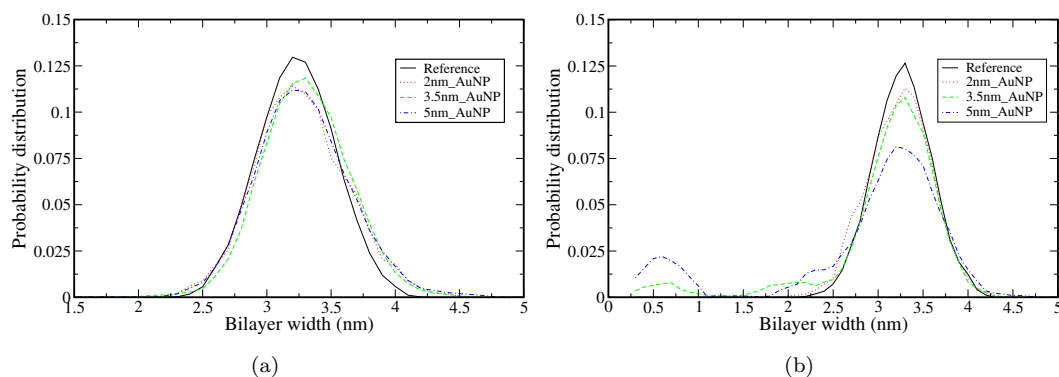
FIGURE 5.16: Distribution of lipid bilayer thickness of (a) LR and (b) SR lipid region respectively. Colors black, red, green and blue represents reference system, 2nm_AuNP, 3.5nm_AuNP and 5nm_AuNP systems respectively.

From Figure 5.16a it is clear that the distributions of a bilayer thickness shift towards higher value than the reference bilayer system. This is the direct evidence of the increase in packing of the LR lipid molecules because of a higher ordering of the aliphatic tails lipid molecules residing in the LR region.

The ordering of the lipid will directly affect the membrane fluidity. Therefore, we have checked the fluidity of the membrane from the mean square displacement (MSD) of SR and LR lipid molecules and compared with the reference bilayer lipid molecules. We have considered last 20 ns part (80-100 ns) of the trajectory to compute the MSD at which the system is expected to be well equilibrated. However, to get the statistically better MSD, we have divided the trajectory in the consecutive intervals of 2 ns and then taken averaged MSD from the individual MSDs of these intervals (Figure 5.17). The lateral and normal to the bilayer MSDs are calculated and depicted in Figure 5.18.
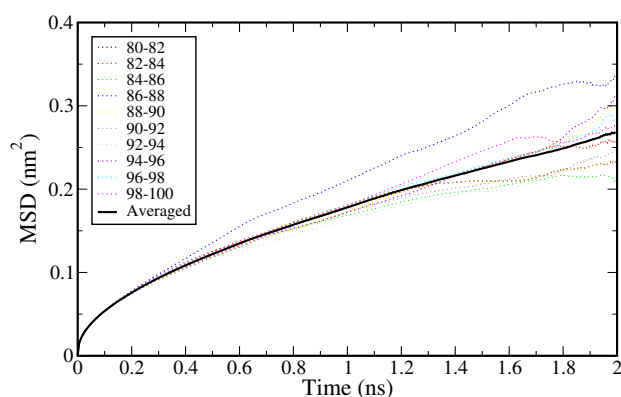
FIGURE 5.17: Lateral mean square displacement of AOPC lipids from last 20 ns with 2 ns interval of each. Black solid line represents average MSD of all intervals.

In all the cases we have observed the decrease in MSDs due to the presence of the NP. The MSDs of SR molecules decreased because of direct interaction with AuNP. However, the decrease in lateral and normal to bilayer MSDs for LR molecules are even lesser than

(a)

(b)

(c)
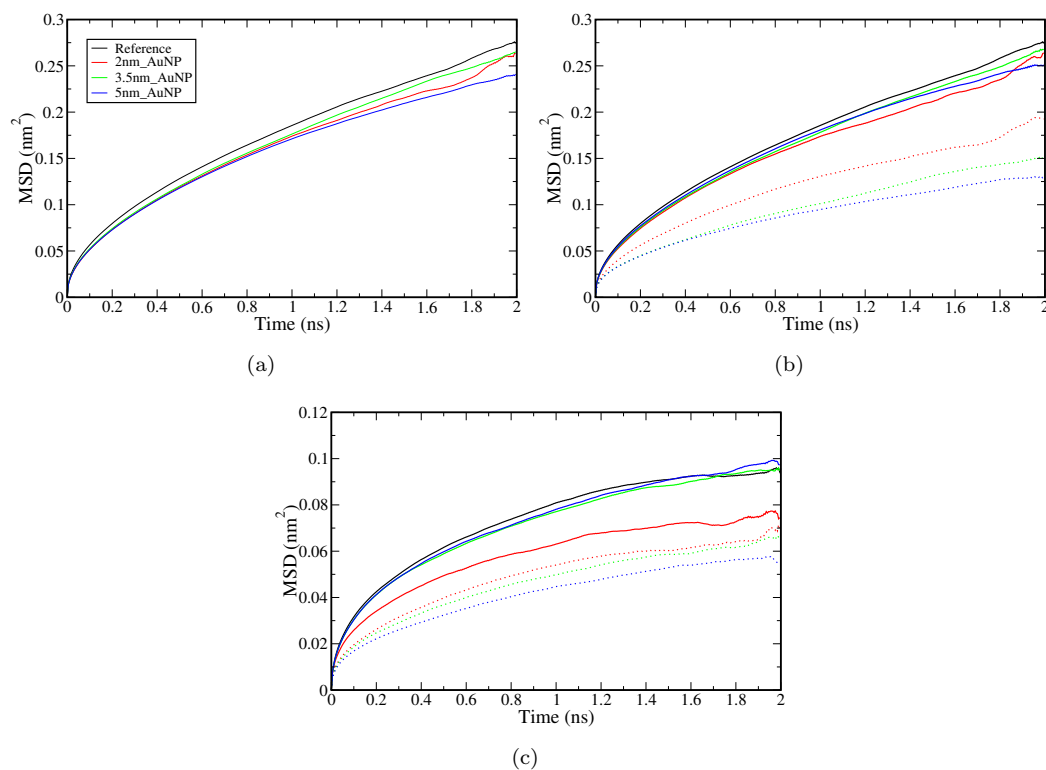
FIGURE 5.18: (a) Lateral MSD of all AOPC lipids in system, (b) lateral MSD of (only interacting leaflet) and (c) MSD of interacting leaflet along bilayer normal. Dotted lines represents MSDs of SR lipid whereas solid lines are for LR lipid molecules.

TABLE 5.3: Diffusion coefficient for SR and LR lipids.

System	SR Lipids ($\times 10^{-7} cm^2/s$)	LR Lipids ($\times 10^{-7} cm^2/s$)
Reference	-	1.50 ± 0.145
2nm_AuNP	0.98 ± 0.145	1.42 ± 0.101
3.5nm_AuNP	0.86 ± 0.199	1.45 ± 0.176
5nm_AuNP	0.62 ± 0.199	1.19 ± 0.243

the SR molecules. Different sized NPs show a similar decrease in MSDs, however the magnitudes are marginally same. The diffusion constants calculated from these MDS are given in Table 5.3.

We have observed the decrease in the diffusion coefficient values for both SR and LR lipids. The lipid molecules much away from the AuNP interacting site indirectly get disturbed, which helps in the ordering the hydrophobic tails. This ordering enhances the packing of the hydrophobic part of the lipid molecules and thus reduces the fluidity of the molecules.

5.4   Conclusions

We have demonstrated the effect of interaction of single AuNP on the lipid bilayer membrane by using all atomistic molecular dynamics simulations. AuNP can alter the structural properties of the head-groups of lipid molecules, which directly interacts with the Gold atoms. We have observed local structural arrangements of lipid head-group near to the surface of the Gold atoms. The motivation of the work was to understand the effect the perturbation caused by the AuNP on the lipid molecules, which are away from the interacting site. To achieve this, we have performed long simulations on sufficiently large bilayer AuNP systems. The results of these simulations are compared with the reference bilayer. The lipid molecules which are away from the AuNP adsorption site showed an enhancement in structural ordering of the hydrophobic tail. The higher ordering the bilayer thickness in the LR region turn out to be increased and area per head group got decreased. The packing of the lipid molecules in LR region became more, which results into relatively lesser fluidity of the LR lipid molecules. The different sizes AuNPs have the same effect on the bilayer. However, the magnitude of structural ordering and fluidity differs. In this work we have dealt with only one AuNP at a time, so the NP concentration on the bilayer surface was very small. Marginally higher concentration of AuNP may enhance the effect of ordering to certain extent. However, much higher concentration will effectively increase deformation in the adsorption sites and can cause changes in bilayer properties. Therefore, understanding in molecular level the effect of higher the loading of NPs in the bilayer remains open for further investigation. In this work, we have focused on the structural change of the lipid molecules in lesser time-scale. In a larger time-scale NPs can alter the inter-leaflet motion of the lipid molecules, i.e., lipid flip-flop. Coarse-gain model of lipid and NP will be useful to address such dynamics of the lipid, which is beyond the scope of this work.

Chapter 6

Free Energy of Bare and Capped Gold Nanoparticle Permeating Through Lipid Bilayer

6.1   Introduction

In chapter 5, we have demonstrated that hydrophilic Gold nanoparticle (AuNP) interact favorably with the lipid headgroups and stays near interface of lipid and water. There would be the energy barrier that prevents the further loading of nanoparticle into the hydrophobic region of the lipid bilayer. Therefore in this chapter, we emphasized on the insertion process of nanoparticle from the water phase to the membrane interior and estimated the free energy required for the process.

Nano-particles have received significant attention over the past century based on their beneficial and detrimental health effect [2–10, 216]. Being nanometer in size, these particles are capable of crossing the cellular membrane. Therefore, are widely being used in biomedicines, such as drug delivery and gene carriers [35, 36]. In spite of that, another subject of concern is its potential toxicity. Hence there is a need for extensive experimentation to understand the risk and the hazards associated [7, 8, 216] NPs in bio applications.

NP crosses cell membrane mainly via endocytosis or direct penetration (diffusion). The translocation of NPs through the lipid membrane is regulated by the physical and chemical properties of NP and lipid bilayer. The considerable amount of research in the similar line has been carried out to understand that how NP properties, e.g., constituents, size, shape, surface topology, and charge influence their interactions with

cell membranes [50, 56, 87, 217, 218]. It is reported that, the size of NP plays a key role in their adhesion as well as penetration through the cell membrane. Larger NPs of size in size range of $\sim 10 - 100$ nm translocate via the process of endocytosis whereas smaller NPs penetrate the cell membrane. Kai Yang investigated the translocation of different shaped NP such as spheres, ellipsoids, rods, discs and pushpin-like particles in the lipid bilayer [54]. They have computed the minimum driving force required for the permeation of the different shaped particle to estimate the penetrating capability of the particle using dissipitive particle dynamics (DPD) model. They showed that the translocation of the particle across the membrane is dependent more on the shape anisotropy and initial orientation of particles than particle volume. However, in case of isotropic spherical particles the penetration becomes difficult with increasing particle volume [219]. Li and Gu reported the effect of charged NP which induces a local transition in fluid like bilayer [196]. The study showed that cationic NPs fluidize the lipid membrane locally, whereas negatively charged NPs help in forming ordered regions in bilayer. The hydrophilic and hydrophobic nature of the NP also influences their interaction with lipid membranes. Hydrophilic NPs generally get adsorbed at the bilayer-water interface, whereas hydrophobic NPs get embedded in the hydrophobic region of the membrane. However the loading of hydrophobic NP in the membrane is energy demanding process [76, 78].

NPs cannot penetrate the membrane easily via diffusion like small molecules such as O_2 and CO_2 due to the energy barriers which increase with the volume of NP. Therefore, an external force on the NP is often applied, which can help its penetration [54, 63, 67–69]. Direct microinjection of nanomaterials into cells, [70, 71], the use of electroporation, [72] and conjugation of natural cell-penetrating/-fusogenic chaperons to nanomaterials [73] are some of the common approaches used in transport of the nanomaterials into the cell. It was observed that, NPs coated with suitable ligand significantly lowers the energy barrier for translocation process [59, 79]. Therefore capping of NP surface with suitable ligand is considered as one of the efficient ways to improve translocation efficiency of NP through the membrane. Polyethelene glycol (PEG), 11-mercapto-1-undecanesulphonate (MUS), Tri-Octyl-Phosphene-Oxide (TOPO) and alkanethiols are widely used as ligand for surface passivation of NP to facilitate its permeation [56–58, 74–77]. Stellacci and coworkers studied the Gold nanoparticle (AuNP) coated with hydrophobic octanethiol (OT) and hydrophilic mercaptopropionic acid (MPA) to understand the translocation of functionalized NPs through fibroblast cell membrane [56–58]. AuNP, composed of a metallic core and self-assembled monolayer (SAM) of thiolated molecules (the ligand shell), have multiple potential applications, e.g., sensing, catalysis, drug delivery and molecular recognition [37, 38, 81–84].

Understanding of the energetics of the permeation process and the effect of surface coating can be helpful in terms of designing or engineering efficient cargo NPs. Therefore, in this chapter, we performed simulations to calculate the permeation of the AuNP through lipid bilayer and the free energy required for NP to translocate across the bilayer. We have also simulated the effect of surface modification (ligand bound AuNP) on the penetration efficiency of NPs from free energy calculations. In the present work, we have performed steered molecular dynamics and umbrella sampling simulations to estimate the permeation free energy for bare and capped AuNP with the lipid bilayer. The lipid bilayer properties have also been analyzed and reported here.

6.2   Computational Methods

The methodology in the present study is divided in four consecutive steps. i) self-assembly simulations of the coarse grained lipids ii) conversion of the coarse grained model to atomistic details iii) equilibration of the bilayer system iv) umbrella sampling simulations to obtain the potential of mean force and free energy for the permeation of NP process.

6.2.1   Self-Assembly of lipids

We have performed the self-assembly simulations using coarse grained lipid models as the time scale at which self-assembly of lipids takes place is typically limited for detailed atomistic simulations [159, 160, 220, 221]. We have used Martini coarse grained force field for the lipid self-assembly simulations [158–160]. Martini coarse graining is done with 4:1 mapping scheme where a group of four atoms is represented by single site (or bead) in order to reduce the degrees of freedom in the simulation to achieve higher time and length scale.

Biological membranes are largely diversified because of their composition and structure. The bilayers made up of lipids with unsaturated tails exhibit higher fluidity compared with lipids with saturated aliphatic tails due to lower melting temperature. Scientists have studied the relationship between the fluidity and the permeation of solutes across the membrane [222–224]. The penetration of the permeant molecules decreases with the diffusivity of the lipids molecules in the bilayer. Thus introducing a lipid having lower melting temperature in the bilayer can enhance/influence the permeability of the NP. Therefore, this chapter deals with the bilayer self-assembled from the mixture of the 1,2-dipalmitoyl-sn-glycero-3-phosphocholine (DPPC) and 1,2-dioleoyl-sn-glycero-3-phosphocholine (DOPC) with two unsaturated tails in 1:1 ratio. In this work we have

considered only one ratio of lipids as we have constructed significantly larger systems and free energy simulations are computationally intensive.

All the simulations in the present study were performed by using Gromacs 4.5.5 simulation package [147–149]. The system consisted of 512 lipid molecules, which could yield considerably large lipid bilayer. The lipids were allowed to self-assemble in the presence of Martini water starting from a complete random configuration of all the molecules. The simulations were performed with isothermal-isobaric ensemble at temperature 323 K which is above the chain melting temperature of $\sim 315K$ for DPPC lipids [225, 226]. The CG model allows a larger time step than that of traditional atomistic simulations. In our case we have used time step of 15 fs. The system temperature was controlled by v-rescale thermostat [180] with coupling constant of 1.5 ps whereas the pressure was kept constant at 1 bar using Berendsen barostat [181] with coupling time of 1.5 ps. The cut-off for non-bonded Coulomb interactions was set to $r_c=$ 1.2 nm and the force was smoothly shifted to zero at cut-off. The simulations were carried with periodic boundary conditions. Similarly the Lennard-Jones potential was shifted smoothly to zero starting from $r_s=$ 0.9 nm. The self-assembly simulation was carried out for 1 μs and the initial and final snapshots of the systems are shown in Figure 6.1. The self-assembled lipid bilayer was then reversed mapped to the atomistic configuration which is further characterized and studied.

Coarse grained model   **All atomistic model**
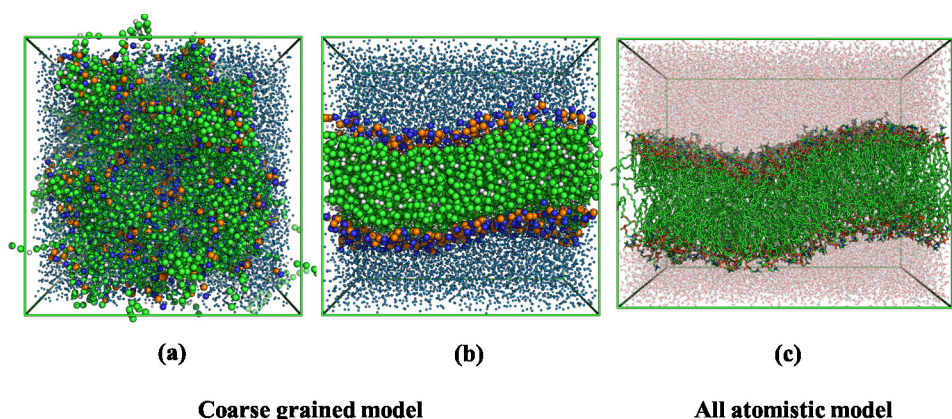
FIGURE 6.1: Coarse grained to fine grained conversion, a) initial coarse grained random configuration b) self-assembled lipid bilayer and c)reverse mapped fined grained lipid bilayer.

6.2.2   Reverse mapping

Reverse mapping or back-mapping is the process of conversion from coarse-grained to atomistic detailed model. This allowed us to map back atomistic details i.e., all the atoms to the coarse-grained beads. The equilibrated coarse grained lipid bilayer (after self-assembly) was mapped to detailed configuration using the atomic and united-atom

model representation. We have used the reverse transformation technique developed by Rzepiela *et al.*, [227] which allows to reintroduce atomistic details in CG structures to obtain a fine grained structure. United atom model of DPPC proposed by Chandashekhar *et al.* [228] and DOPC by Poger *et al.* [229] were used to convert the coarse grained lipid bilayer into the atomistic configuration. The technique involves random positioning of atomistic particles within a sphere around their corresponding CG beads. It is followed by restrained simulated annealing (SA) to generate low energy and high resolution system. In the simulated annealing, the temperature is gradually decreased from a high starting value to the desired target temperature which allows the system to rapidly cross energy barriers and attain the low-energy minimum at the end of the simulation. We have performed SA run for 80ps, followed by 140ps equilibration at the final temperature of 300 K under the restraints. The initial temperature T_{init} was chosen 1300 K which is high enough to overcome the relevant energy barriers during the simulation. Thereafter, the restraining potential was removed within a time period of 10 ps. The resulting fine grained united atom model of lipid bilayer was further equilibrated for 15 ns (the simulation details are explained in the next section) with SPC water model [178]. The potential energy and volume of the box computed from the equilibration trajectory are plotted in Figure 6.2. This equilibrated bilayer was then used to construct the NP-membrane system.
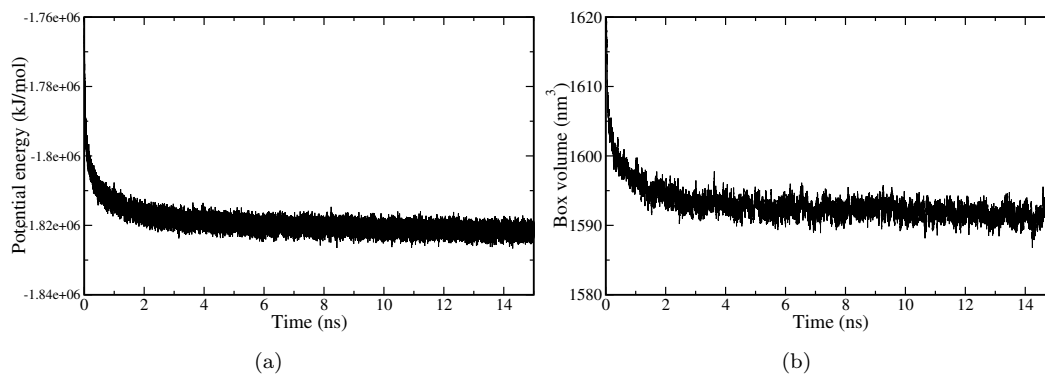
FIGURE 6.2: (a) Potential energy and (b) box volume as a function of simulation time.

6.2.3   Construction of nanoparticles

A spherical bare AuNP of size 3 nm in diameter was constructed using fcc lattice of Gold atoms. The initial structure of AuNP is obtained by taking the Gold atom which falls in the spherical cut-off of 1.5 nm from an atom (defined as central atom) of the fcc crystalline lattice (Figure 6.3). The non-bonded Lennard-Jones parameters were obtained from paper of Heinz *et al.* and were used to define the interaction potential between the Gold atoms [213]. These parameters maintain integrity of the NP shape throughout the

simulation as seen in the previous chapter. We have used this bare AuNP for further simulations. The snapshot of the initial spherical AuNP is shown in Figure 6.3a.
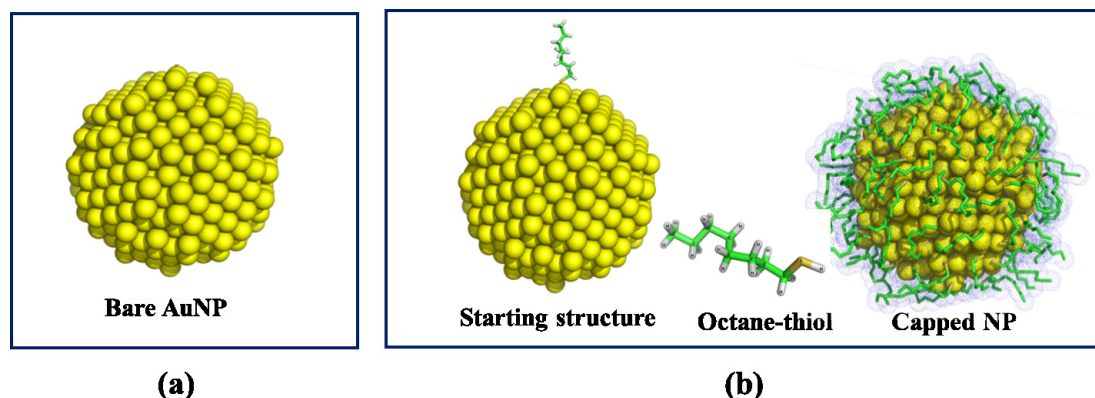
FIGURE 6.3: (a) Initial configuration of bare AuNP and (b) capped AuNP.
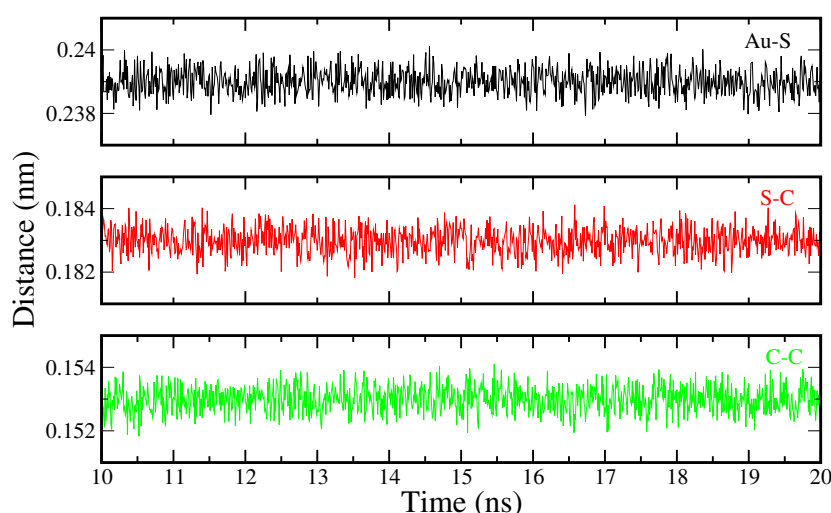
FIGURE 6.4: Distances between Au-S (black), S-C (red), C-C (green) atoms.

In this present study, we considered capped AuNP modeled with octane-thiol (OT) molecules linked to NP surface (Figure 6.3b). A united atom representation was used to treat the octane-thiol molecules in the simulations. The connectivity between surface Gold atoms and alkane chains was defined with the thiol linkage between Gold and sulphur atom. The Au-S bond strength and the angle bending (Au-S-C) parameters were taken from the work of Seminario *et al.* [230] and Hautman *et al.* [231] respectively. The octane chain was represented by the GROMOS53a6 united atom model. The AuNP was functionalized with 115 chains of octane-thiol (Figure 6.4b). The surface area occupied by single alkane-thiol is 21.6 $\mathring{A}^2$, [232, 233] therefore 115 chains were enough to cover the AuNP surface (Figure 6.3b). The coated AuNP was then equilibrated for 10 ns in a simulation with water as solvent and the final structure was used for further simulations with bilayer. We have calculated and plotted the distances between Gold-Sulphur,

Sulphur-Carbon atoms and Carbon-Carbon atoms of a octane thiol chain to check the consistency of the bonds (Figure 6.4).

6.2.4 Equilibration of a AuNP-lipid bilayer system

In two different simulation boxes containing equilibrated lipid bilayer with atomistic details, we placed bare and capped AuNP on the top of the bilayer approximately at distance $\sim 6 - 7$ nm away from the bilayer center of mass. These simulation boxes were then solvated and equilibrated initially with SPC water model [178] by restraining the position of AuNP for 10 ns. Another 2 ns additional equilibration run was performed without any position restraint to relax the NP structures. We have simulated a sufficiently large system, which includes 512 lipid molecules, AuNP and water molecules accounting total of ~ 190000 atoms (system details are given in Table 6.1).

TABLE 6.1: Details of the bilayer NP systems.

System	Gold (Au)	OT	Lipids	water	Total	Simulation box (nm)		
						X	Y	Z
Bare NP	627	0	26624	155919	183170	12.67	12.67	14.12
Capped NP	627	1035	26624	171000	199286	12.78	12.78	14.97

Isothermal and isobaric ensemble with periodic boundary conditions are employed to perform all the simulations. A temperature of 300 K was kept constant using v-rescale thermostat [180] with coupling constant of 0.1 ps. Constant pressure of 1 bar was maintained by using Berendsen barostat [181]. All bonds were constrained with LINCS algorithm. The non-bonded LJ interactions were taken care with the cut-off of 1.4 nm and electrostatic interactions Particle-Mesh Ewald (PME) [146] method was used with 1.4 nm cut-off. These equilibrated structures were then used to perform steered molecular dynamics (SMD) simulations.

6.2.5 Free energy calculation

We employed SMD simulations to pull the AuNP the along the bilayer normal from bulk water to bilayer interior. Two independent SMD runs of 5 ns for bare and capped AuNP were carried out, allowing the NP to penetrate the bilayer. The AuNP was pulled along the z axis with a force constant of 1000 $kJ/mol/nm^2$ with pull rate of 0.005 nm/ps using pull code as implemented in GROMACS 4.5.5 [147–149]. The pull rate is carefully chosen such that NP does not rupture the lipid membrane. The non-bonded cut-off were

used same as used for equilibration run. The simulation trajectory was written after every 2 ps.

The potential of mean force (PMF) of AuNP bilayer systems as a function of the distance between the centre of mass (CoM) of the NP and the center of mass of the bilayer were calculated using umbrella sampling simulations. In total 50 and 75 configurations (windows) for bare and capped AuNP respectively, were extracted from the respective SMD trajectories and then used to perform simulations by incorporating umbrella potentials. Independent umbrella sampling simulations were performed with harmonic umbrella potential [153–155] with a force constant 1000 $kJmol^{-1}$. All the sampling windows were simulated for 5 ns. The spacing between adjacent umbrella sampling windows was chosen carefully between 0.1 and 0.5 nm depending upon the separation between bilayer and NP CoM distance. Weighted histogram analysis method (WHAM) [184] was used to calculate the PMF and finally Gibbs free energy.

6.3 Results

6.3.1 Free energy

PMF for the permeation of bare and capped AuNP are calculated from the umbrella sampling simulations. The PMF of the systems as a function of the distance between the NP and the bilayer for bare and capped AuNP are plotted separately in Figure 6.5a and b. The free energy profile of both the systems comprises of two different regions, NP adsorption and loading of NP into bilayer interior.
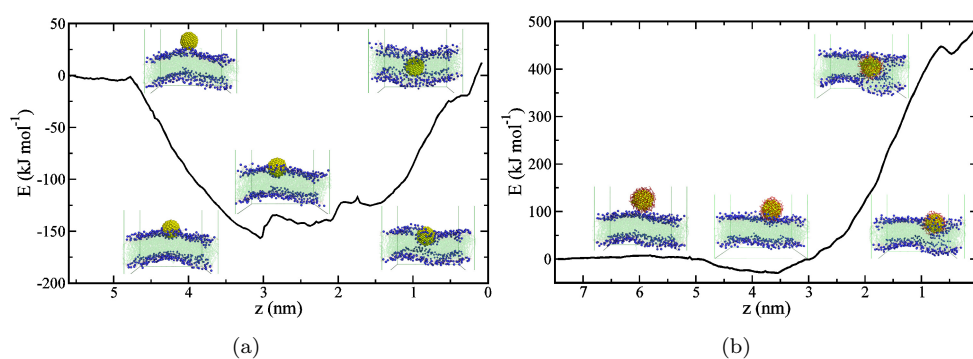
FIGURE 6.5: Potential mean force for the permeation of (a) bare and (b) capped NP. The reaction coordinate z (bilayer normal) is the center of mass distance between lipid bilayer and NP.

From Figure 6.5a, a sharp decrease in the PMF is noted because of adsorption of the AuNP to the hydrophilic region (bilayer water interface) of the bilayer. The drop in the PMF continues till it reaches the most energetically favorable state at the CoM distance

of 3 nm between bilayer and NP. At this point, the interaction between hydrophilic headgroups and Gold atoms of the NP are optimum to minimize the free energy of the system. This indicates the hydrophilic nature of the AuNP interact well with the lipid head groups and water around it. To quantify these interactions we have further calculated the distance distribution functions (RDF) between the Gold atoms of bare AuNP and water oxygen (Au-OW, Figure 6.6a) and lipid head group nitrogen atoms (Au-N, Figure 6.6b). We have also checked the RDF of surface Carbon (C1) atoms of capped AuNP with OW and lipid headgroups. The RDFs clearly depict the ordering of lipid head groups and water molecules near the bare AuNP due to the favorable hydrophilic interactions compared to capped AuNP.
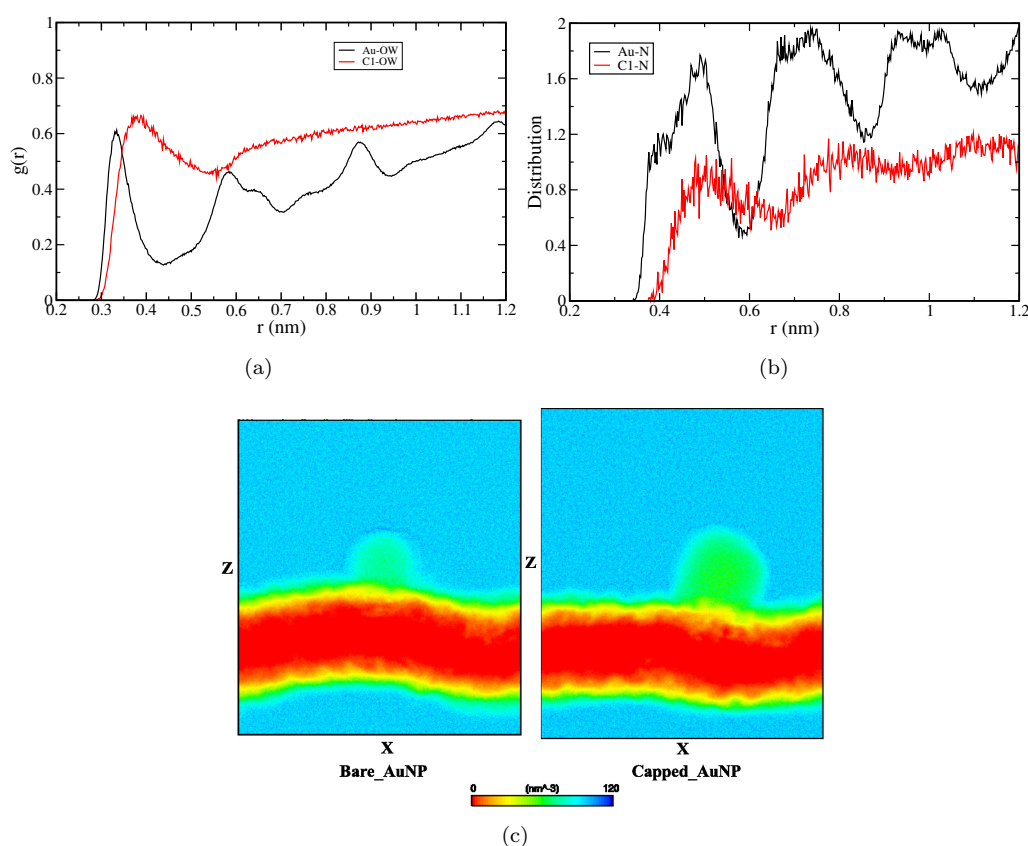
FIGURE 6.6: (a) RDF of water Oxyegen (OW) with surface Au atoms of bare NP and surface C1 atoms of capped (C1) NP colored black and red respectively (b) RDF for lipid headgroup atoms (N) and Au with C1 represented as black and red lines respectively. Figure (c) two dimensional density map of the water.

We have calculated two dimensional density map of water (averaged over the Y axis) and depicted in Figure 6.6c which clearly shows the ordering of the water near the NP. As a result of this favorable interaction with interface water and lipid headgroup, the free energy of -150 $kJmol^{-1}$ indicates a forward reaction of adsorption of bare NP on bilayer surface. However, in between 3 to 1.5 nm (CoM distance between NP and bilayer), a gradual increase in the PMF is noted with a sharp rise after the CoM distance reaches 1.5

nm. The free energy required for further loading of the NP after adsorption is positive and calculates as $\sim +125 kJmol^{-1}$.

The free energy profile obtained for the octane-thiol capped AuNP showed a slight dip in the free energy profile after 5 nm as shown in Figure 6.5b followed by a sharp rise in PMF as observed in the case of bare AuNP. The dip in the free energy profile resulted due to the NP interaction with lipids, which introduces disruption in a membrane leaflet by inserting the octane chains into the hydrophobic region (see Figure 6.7) of the bilayer. It shows favorable interaction to open up the membrane for insertion of NPs into the bilayer. However, the free energy change is very small (-30 $kJmol^{-1}$). Thereafter, the calculated free energy required to load the capped AuNP from the interface to the membrane interior is more than bare AuNP. The free energy of $\sim 500 kJmol^{-1}$ clearly shows that the accumulation of caped NP in the bilayer interior is energetically unfavorable process.

The computed adhesive forces between NP and bilayer in the present study are good agreement within the range provided by Vasir *et al.* [234] from their experimental observations. They have shown that modified NPs demonstrate greater adhesion toward cell membrane and interact more favorably with the greater adhesive force (50- 1200 pN) than unmodified NPs which show fewer interactions (20- 280 pN). These adhesion forces are the results of binding of NP surfaces with the molecules present on cell surfaces. In the present study, hydrophilic bare NP interacts favorably with outer leaflet of the lipid bilayer with the probable force of ($\sim$ 249 pN) whereas capped AuNP shows the lower limit of the range ($\sim$ 50 pN). One should note that the size and capping agents used for NP passivation are different from experimental work.
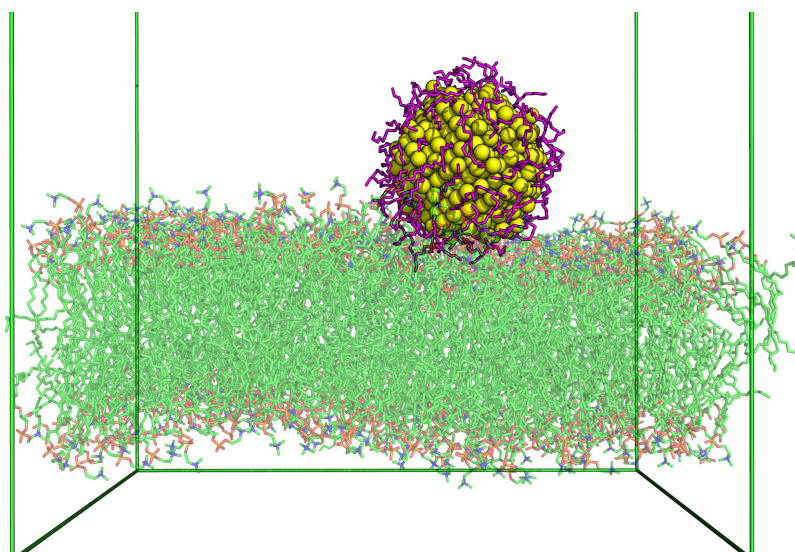
FIGURE 6.7: Snapshot for the interaction of capped AuNP with lipid bilayer.

Experimentally researchers have observed that hydrophobic NPs favor to stay in the hydrophobic membrane interior but their loading into the membrane is difficult [76, 78].

Hence, an external force is always needed to accelerate the permeation efficiency of the NP [54, 63, 67–69]. Besides hydrophobicity, the particle volume is also a crucial factor of translocation. The penetration of a spherical particles becomes more difficult with increase in the particle volume [219]. Therefore in our case, the hydrophobic nature of the capping and the particle volume because of surface capping made the penetration energetically unfavorable. In addition, we have analyzed the bilayer-NP system further to investigate the factors involved in the loading of NP which finally contributes to the free energy.

6.3.2 Density profile

The partial densities of lipid, NP and water along the bilayer normal are computed and plotted in Figure 6.8a and b for bare and capped AuNP respectively. The partial densities were computed from the different sampling windows depicting the location of the NP in a simulation box. From Figure 6.8, a nearly identical density profile for the both systems are observed when NP resides in bulk water and the deformation in the lipid bilayer is seen as NP progresses towards the lipid bilayer for both NP system.
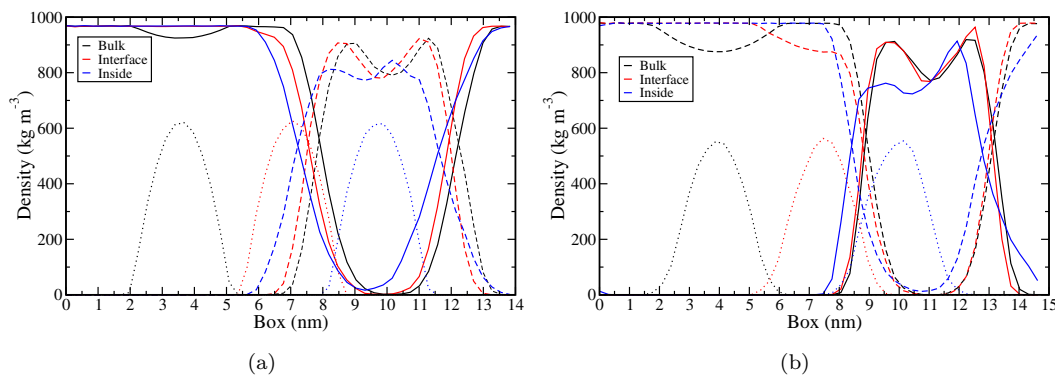
FIGURE 6.8: Partial densities for lipids (dashed lines), NP (dotted lines) and water (solid lines) of (a) bare NP and (b) capped NP consisting system. Colors black, red and blue depicts the location of nanoparticle as in water phase, bilayer water interface and inside the lipid membrane respectively.

AuNP induces deformation in the lipid bilayer by pushing lipid molecules inside the membrane. Therefore, a gradual decrease in lipid partial density (at distance 6-10 nm for bare NP and 7-11 nm for capped NP system) is noted in both cases. However, the extent of perturbation caused by capped AuNP is more as seen from the widely spread lipids in the simulation box.

6.3.3   Penetration of water

Both AuNPs disrupts the lipid membrane and thus allows water molecules to penetrate the hydrophobic region. This is examined by calculating the partial density of the water along bilayer normal axis (Figure 6.9a). The umbrella sampling simulation trajectories were chosen correspond the location of NP (i.e. bulk, interface and inside) to compute the partial density. The partial densities of water in the hydrophobic region of lipid membrane for both the systems are plotted in Figure 6.9a. The left and right panel of the figure describes the water densities for systems consisted of bare and capped AuNP respectively. It is evident from Figure 6.9, that water molecules penetrate into the lipid bilayer along with bare Gold nanoparticle and a significant amount of water molecules in the hydrophobic regions of lipid membranes are noted in both cases.

(a)

(b)

(c)

(d)
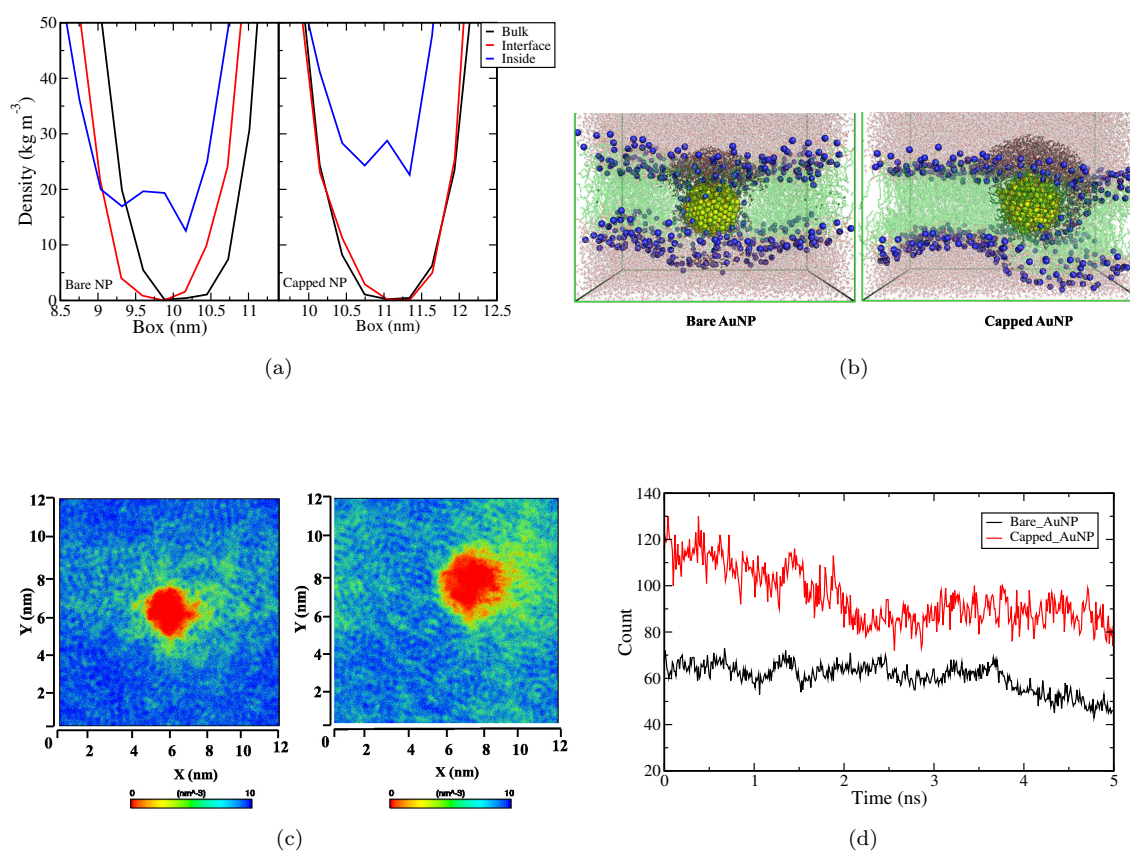
FIGURE 6.9: Penetration of water molecules (a) Partial densities of water at different NP location (b) snapshot for NP permeation along with water (c) two dimensional density map of lipids and (d) number of water molecules in membrane interior.

In bare AuNP system, water molecules penetrate along with hydrophilic NP. On the other hand, capped AuNP creates a pore like structure in the lipid bilayer by pushing of some lipid headgroups of the interacting leaflet (can be attributed as an effect of pulling). This allows water to enter along the lipid headgroup. The disruption in the membrane is further checked by calculating the two dimensional density map of lipids averaged over z

axis (for interacting leaflet) and plotted in Figure 6.9c. It is evident from the figure that capped AuNP create more local deformation on the lipid bilayer and the periphery of the pore is less dense (lipid) compared to bare NP-bilayer. This is due to the presence of the ligands, which spread around the NP and cause more perturbation to the interacting leaflet.

Further, in this section, we have calculated the number of water molecules penetrated along NP and plotted in Figure 6.9d. We have considered the umbrella sampling trajectory with most perturbed bilayer to calculate the number of penetrating water (see Figure 6.9b). The water molecules fall in the distance cut-off of 1 nm from the NP surface were considered. We have discarded the water molecules which are at the bilayer water interface. From Figure 6.9d, we clearly see significant a higher number of water molecules penetrate with capped AuNP compared to bare AuNP. This is counter intuitive because hydrophobic NP (i.e., capped with hydrophobic ligand)imparts more mobility of water molecules. However, this is may be due to larger the size of NP (because of capping) than bare NP and differences in pore formation mechanism. We have discussed this further in the following sub-sections.

6.3.4   Bilayer curvature

The NPs are known to affect the lipid membranes by inducing the membrane curvature or by the formation of pores. A number of simulation studies have demonstrated that NPs that interact favorably with the lipid headgroups can promote curvature formation on the lipid membrane [235–237]. Therefore, to quantify the curvature of lipid membrane induced upon AuNP interaction, we have calculated the tilt angle between the lipid headgroup phosphorous atoms (P), lipid CoM and bilayer normal. The umbrella sampling simulation trajectories (non perturbed and maximally perturbed membrane) were used to compute the tilt angles. The distributions of these tilt angle were calculated and plotted for systems consisting bare and capped AuNP in Figure 6.10a. The left and right panel of this figure shows tilt angle distribution for upper (interacting with AuNP) and lower leaflet respectively. The angle of 0° shows the perfect alignment of the lipid headgroups with the bilayer whereas the wider distribution of tilt angle denotes the bending of lipid headgroups.

In case of a capped AuNP system, a nearly identical angle distribution for perturbed and non perturbed membrane is observed. However, for the upper leaflet, the effect of perturbation can be clearly seen from a slight fall in the angle distribution at angle 20°. In case of hydrophilic bare NP, a notable shift in tilt angle is been observed. The distribution of tilt angle shifts towards higher values than the non-perturbed membrane. This suggests

(a)

(b)

(c)
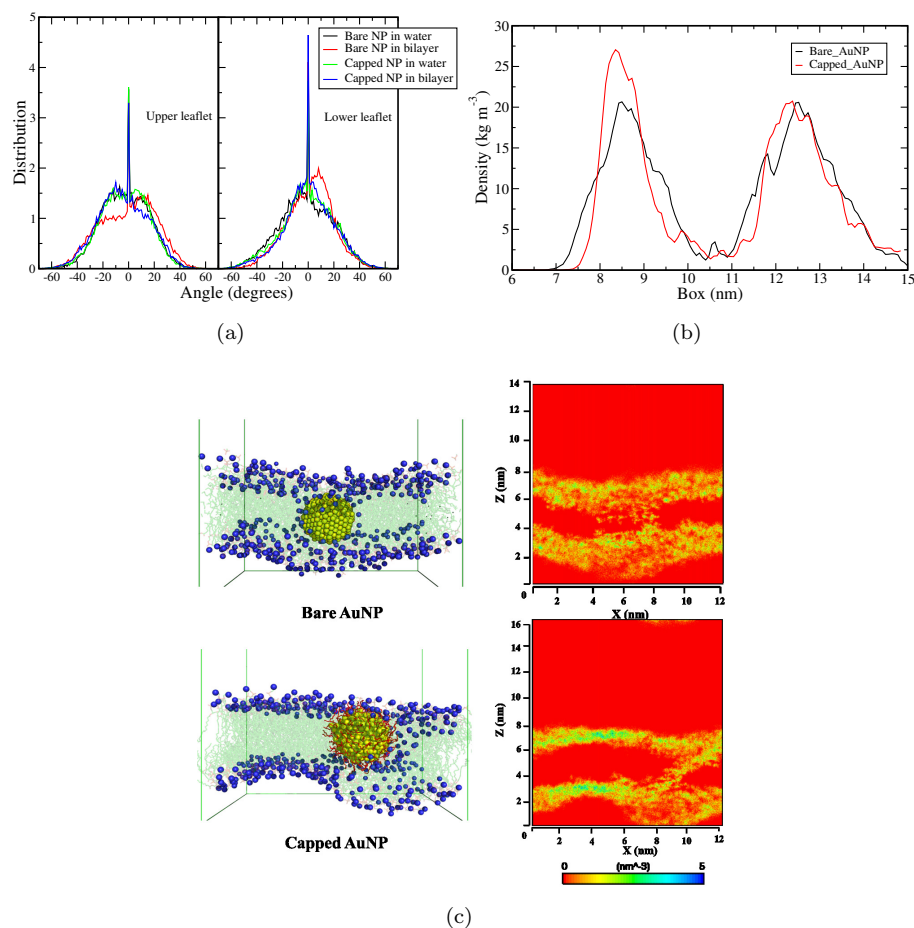
FIGURE 6.10: (a) Headgroup tilt angle distribution (b) Nitrogen atom partial density along z axis (c) snapshot and two dimensional density of nitrogen atoms averaged over y axis

that bare NP induces curvature in lipid layer by pushing the lipids toward the inner leaflet. It is further elaborated by calculating the partial densities of headgroup nitrogen atoms along the bilayer normal. We have calculated partial densities for the nitrogen atoms of both the systems and plotted in Figure 6.10b. It shows wider distribution of lipids for bare AuNP compared to capped AuNP. We have further calculated the two dimensional density map averaged over the y axis (Figure 6.10c). From the density map, it is evident that bare AuNP pushes the lipid headgroup towards the inner leaflet of the membrane. As a result of this, lipid membrane adapts a curvature near to the NP. The snapshots taken from the most perturbed sampling window are presented in same figure shows the curvature of lipid bilayer near bare AuNP. On the other hand, because of a capped AuNP upper leaflet of the bilayer opens up. However, we do observe few lipid headgroups within the hydrophobic region in case of capped AuNP-bilayer system, may be due to the high pulling rate of large sized NP.

6.3.5   Lipid ordering

We have observed in the previous chapter that ordering of lipid tails gets affected due to the interaction of NP with bilayer leaflets. We have correlated this with the fluidity of the membrane. Korgel *et al.* [200] has explained the enrichment of hydrophobic NPs within the lipid bilayer which finally affects the properties of lipid bilayer such as lipid packing and the lipidlipid interactions. They have also shown that the NPs get accumulated in the bilayer interior by unzipping of the leaflets. We have shown in this chapter that the energy needed for this accumulation (via an unzipping mechanism as suggested by Korgel *et al.* [200]) for hydrophobic capped NP is very high. This leads to changes in lipid packing especially the lipid tail ordering [201, 238].

Lipid order parameter is a quantity which can be affected as a consequence of this bilayer leaflet unzipping. The orientational order parameter ($-S_{cd}$) for the lipid tails with reference to the bilayer normal axis according to Chau *et al.* [239] and Tieleman *et al.* [240] is calculated for bare and capped NP-bilayer systems. The order parameter is based on the tilt angle of the acyl chain with respect to the bilayer normal.
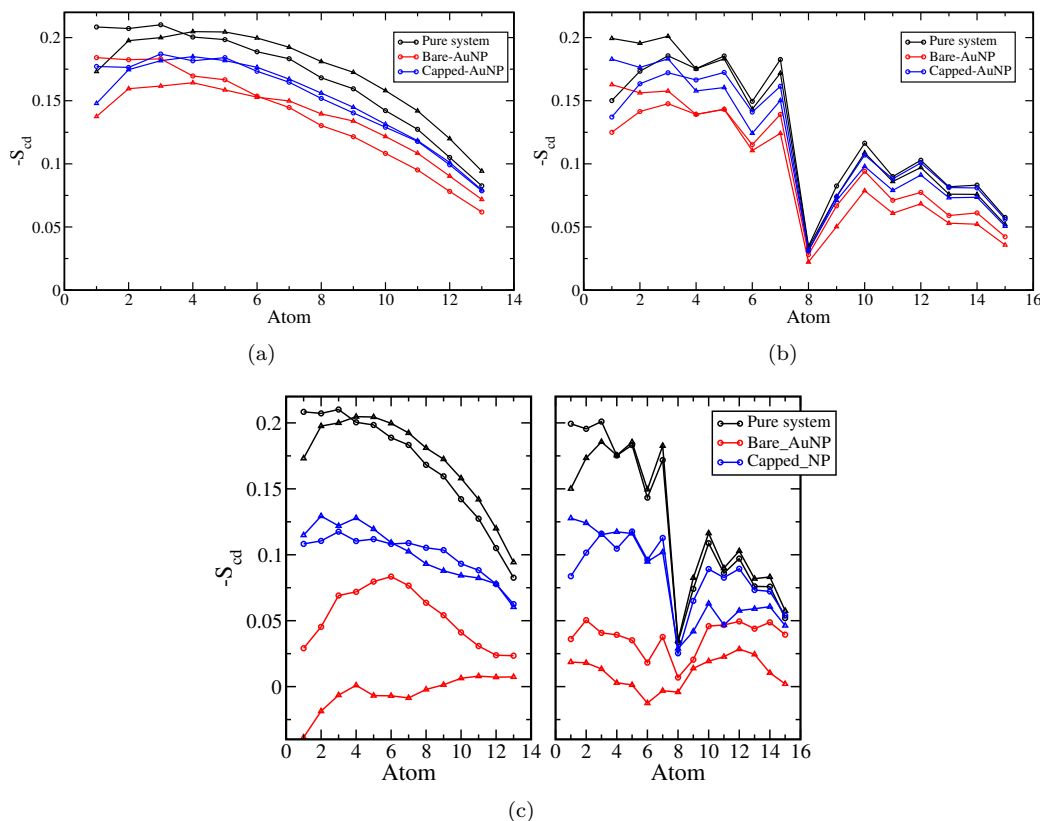
FIGURE 6.11: Lipid tail order parameter for all (a) DPPC and (b) DOPC lipids respectively. Figure (c) shows lipid order parameters for NP interacting lipids. The left and right panel are for DPPC and DOPC lipid tails respectively.

The order parameters for lipids DPPC (saturated chains) and DOPC (unsaturated chains) plotted separately in Figure 6.11 for both bare and capped AuNP-bilayer. The order parameters for bilayer (without any NP, termed as Pure system) also plotted in the same figure (Figure 6.11 a, b) to compare the effect of NPs on the membrane. The effect due to the perturbation caused by NPs is clearly seen in the both cases. Bare AuNP significantly perturb the system and is higher than the capped AuNP. This is may be due to differences in insertion mechanism. Because of the hydrophobic nature capped AuNP, it gets inserted into the membrane by unzipping the lipid membrane, thus perturbs the bilayer less. Whereas, bare NP pushes the leaflet and causes more decrease in the ordering (packing) of the lipid tails.

We have also quantified the effect of perturbation locally at the NP adsorption site. The lipid molecules directly interacting with the NP (lipids within 1.5 nm from NP surface) were considered to calculate the tail order parameters. From Figure 6.11c, left (DPPC) and right (DOPC) panels it is evident that the lipids, which are interacting with the hydrophilic bare AuNP are severely affected compared to the capped AuNP. The size of the capped AuNP is larger than the bare AuNP, intuitively larger particle should cause more distortion to the bilayer. However, because of different insertion mechanisms we observe less disorder caused by capped AuNP.

6.3.6   Bilayer thickness

From the partial density plots, it was observed that lipids were pushed inside along with the NP and lipid tail order parameter showed the higher ordering upon interacting with the capped AuNP than bare AuNP. It is reported that the increased chain order leads to increased hydrophobic thickness [241, 242]. We have further investigated this by calculating the thickness of the bilayers while interacting with NPs. The bilayer thickness is computed as a distance between the phosphorous atoms of lipids from upper and lower leaflet using a GridMat algorithm [243]. The bilayer was divided into 20×20 grids along the XY plane (i.e., bilayer plane) and the lipid molecules falling in each grid were chosen to compute the distance between P atoms of headgroups residing in two leaflets. The last 2 ns of umbrella sampling simulation trajectory (of adsorbed AuNP) was used to compute the thickness. In every grid, the distances were calculated between the lipid headgroups. Thereby, a contour plot obtained from these 20×20 grid distance data points which is depicted in Figure 6.12a and 6.12b for bare and capped AuNP system respectively. A distinctive contours of thickness of 0.5-1.5 nm is observed for both the NP bound systems which is an indicative of local disruption of the lipid bilayer at the NP adsorption site. The smaller bilayer thickness values depict pushing of the lipids to membrane interior

thus yield lower values. Larger contour area of smaller thickness values is observed for bare AuNP (Figure 6.12a) compared to capped AuNP bound bilayer.
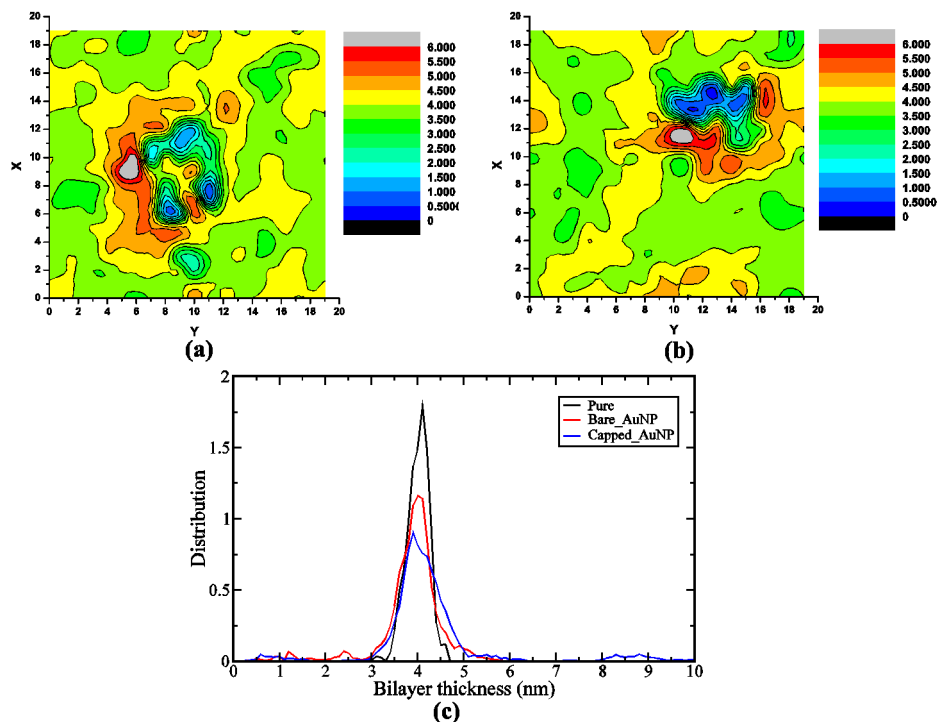
FIGURE 6.12: Contour plot for bilayer thickness of systems with (a) pure lipid bilayer, (b) bare NP and (c) capped AuNP respectively and (c) represents distribution of the lipid bilayer thickness. Color black red, and blue shows distribution for pure lipid bilayer, bare and capped AuNP consisting system.

Further, to quantify this we have calculated distribution of thickness values and plotted in Figure 6.12c. From figure 6.12c, a clear shift towards the higher value is observed for the capped AuNP bound system. In addition to that a finite distribution for values between 8-10 nm is also observed for capped AuNP, whereas a wide range of values are observed for bare AuNP. This shows that the insertion of capped AuNP in the membrane interior unzips the lipid bilayer which does not effect the lipid ordering as much as for bare AuNP.

6.4   Conclusions

In summary, we have investigated the translocation of NPs across the lipid membrane using all atomistic molecular dynamics simulations. We have calculated the free energy required for the loading of bare and capped AuNP in the lipid membrane using SMD and umbrella sampling simulations. We have shown that how the surface passivation of the NP with hydrophobic ligands change the mechanism of permeation process. The estimated adsorption free energies for bare and capped AuNP are -150 $kJmol^{-1}$ and

-30 $kJmol^{-1}$ respectively. However, further loading for both the AuNPs are found to be energetically expensive. The free energies calculated for loading of bare and capped AuNP in the hydrophobic region of bilayer are +125 $kJmol^{-1}$ and +500 $kJmol^{-1}$ respectively. The high energy barrier for the capped AuNP comes from the cumulative effect of hydrophobic surface coating and increased particle volume.

We have also shown that bare AuNP induces curvature in the lipid bilayer with local deformation of the lipids ordering at the site of adsorption. The octane-thiol capped AuNP gets inserted into the lipid membrane by unzipping it whereas, bare AuNP pushed the lipid molecules along with it. As a result of this, we observe less ordering of the lipids and decreased bilayer thickness for bare AuNP compared to capped AuNP. We have reported in this chapter the penetration of the water molecules along with the NP. The bare AuNP pushes the lipid to the membrane interior along with water molecules attached with the headgroups. However, capped AuNP ruptures the lipid membrane by forming pores. In this work, we have dealt with only one AuNP at a time. The higher concentration of AuNP may have different effect on the bilayer properties. This work can be extended by investigating the NPs functionalized with different types of ligands (charged and amphiphilic ligands) which may have different permeation characteristics.

The findings of the current work will lead to better understanding of the translocation mechanism of NPs across lipid membranes, which can be useful in developing efficient nano-cargoes for delivery of therapeutics and better understanding of the mechanisms for cytotoxicity of some types of NPs.

Chapter 7

Self-Assembly of Phospholipids on Flat Model Supports[1]

7.1   Introduction

Extending the study of the interaction of lipid membranes with the nanoparticle (chapter 5 and 6 of part B), interaction of lipid bilayer with the surfaces is studied in the chapter 7. Lipid bilayers supported on the surface provides an artificial platform which can mimic the cell membrane. It helps to exclude various factors influencing the experiments carried out on real cells and provide a possibility to focus on the phenomena of interest. This chapter investigates the physico-chemical properties of the lipid membrane under the influence of the solid supports. Supported bilayer is used for studying the cell membrane as it preserves the functions and properties of the lipid bilayer as observed in living cells [93–95]. Therefore, it has gained a lot of attention due to its various applications in the areas of biological and pharmaceutical research [27–29]. SLBs are excellent model to understand the T cell immunological synapse, [99, 100] neuronal interactions, [101] and the triggering of EphA2 receptor in mammary epithelial cells [102]. The SLBs are also used as biosensors and biodevices [95–98]. Richter *et al.* [244] reviewed various SLB systems that includes solid-supported lipid bilayers, [103–107] polymer-cushioned lipid bilayers, [108–110] hybrid bilayers, [111, 112] tethered lipid bilayers, [113] suspended lipid bilayers, [114, 115] and supported vesicular layers [116, 117]. Experimentally, the SLBs are formed on solid substrates like silica-based surfaces (e.g., glass, aerogels, xerogels) and mica [27, 118–120]. Among the several experimental methods for the formation of SLBs [93], the vesicle fusion [123] and Langumuir-Blodgett [121, 122] are considered as

---

[1]This chapter is adapted from the publication Mhashal AR, Roy S (2015) Self-Assembly of phospholipids on the at model supports. Physical Chemistry Chemical Physics, 2015,17, 31152-31160

the most commonly used techniques to yield SLBs. However, theoretical studies dealt with SLB involve deposition of self-assembled lipid bilayer over solid substrate. One of the theoretical investigations of SLB was done by Xing *et al.* [245]. They performed molecular level simulations of free standing pre-assembled bilayer on the model supports. They transferred pre-assembled lipid bilayers in water to model supports which was further simulated by using molecular dynamics. The study emphasized on the properties of lipid bilayer as a function of the geometry and chemical nature of the support.

The support essentially plays a vital role in determining the properties of supported membrane. The physical and chemical properties of the substrate often change the properties of deposited bilayer/monolayer such as decoupled phase transitions [54, 124–126] and structural and dynamical heterogeneity of inner and upper leaflet [127–129]. Cha *et al.* showed that the surface charge density of support controls the rupture of adsorbed lipid vesicles to form stable, supported phospholipid bilayers [246]. Lin X. *et al.* investigated the interactions between hydrophilic nanoparticle with the bilayer supported on the surface [247].

Self-assembly of the lipids on the supports can produce supported lipid bilayers alternative to the deposition of the pre-assembled lipid assemblies on supports. Besides that, the self assembly of lipids from the complete disordered state in the presence of artificial model surface is unexplored till date. Therefore, it would be interesting to understand the complex self-assembly process in the influence of the external perturbations due to supports. Hwankyu Lee [248] studied the self-assembly of lipids on single-walled carbon nanotube by performing molecular simulations. They performed simulations of lysophospholipids and phospholipids grafted/ungrafted with polyethylene glycol (PEG) and studied the assemblies of these lipids on the nanotube. They reported the formation of cylindrical monolayer resembling micelle of the di-palmityl-phosphotidylcholine (DPPC) and di-palmitoyl-phosphatidylglycerol (DPPG) lipids around the nanotube. The hydrophobic nature of the carbon nanotube induces the adsorption of the lipid in a monolayer fashion. Hydrophobic support are also been extensively studied [249–251] and have reported the formation of lipid monolayers on the support.

However, on the other hand, the substrates used in case of SLBs are mostly hydrophilic in nature e.g., silica derivative substrates. The supported lipids on the such substrate maintain the bilayer morphology in head-tail-tail-head fashion with lipid head-groups facing hydrophilic support [245, 247]. Hence, after self-assembly, one could expect different macroscopic structure depending on the chemical nature of the substrate. A number of attempts have been made to construct the SLBs on hydrophilic surfaces such as gold, [124] SrTiO2, [252] TiO2, [253] and platinum experimentally [254]. However,

mica and silicon-based materials, such as glass, Si3N4, or silica considered to be the most common surfaces used for the preparation of SLBs [27, 118–120].

It is also reported that the chemical nature of the support has an effect on the bilayer properties [54, 124–129, 245]. It is believed that hydrophobic or hydrophilic nature of substrates can affect the bilayer properties differently. However, it is also probable that different strength of hydrophilicity or hydrophobicity of the support affects the bilayer properties to a different extent. Peter Lenz et al. [250] performed successive plasma oxidation of the poly-dimethylsiloxane (PDMS) substrate from SiCH3 to SiOx and found out the formation of monolayer and then bilayer when moved from hydrophobic substrate to hydrophilic substrate.

To the best of our knowledge, self-assembly simulations of lipids on flat surfaces having different hydrophobicity and hydrophilicity were not studied. Therefore, in our study, we have simulated self-assembly DPPC lipids on flat supports by varying the hydrophobicity and hydrophilicity to elucidate the mechanism of self-assembly. We have also analyzed and compared the properties of the self-assembled supported bilayers. The choice of the parameters to define hydrophilic or hydrophobic support was decided on the basis of the water droplet simulation on the model support. In the present work, we have constructed eight supports with different strengths of hydrophobicity and hydrophilicity and have employed molecular dynamics (MD) simulation to self-assemble the lipids on these supports. The present work is mainly focused on the following issues a) self-assembly lipids on flat support and b) effect of hydrophobic and hydrophilic nature of support on self-assembly of the lipids c) properties of the lipid bilayer on different support and d) the mechanism and energetics of lipid self-assembly process.

7.2   Computational methods

All the simulations were carried out using GROMACS 4.5.5 [148, 149] simulation code. The coarse grained Martini model for lipid and water proposed by Marrink were used [158–160]. In this work, we have considered model solid supports made of hydrophilic and hydrophobic beads. The hydrophobicity and hydrophilicity of the support were decided on the basis of interaction strength (parameters) ϵ_{sw} between the support beads (S) and water (W) beads. Martini force field consists of 4 types of beads, polar (P), nonpolar (N), apolar (C) and charged (Q). The hydrophobic moieties in force field are represented as type C beads with five variants from C1 to C5. Type C1 bead is the most repulsive to water with interaction parameter $\epsilon_{ij} = 2.0$ kJ/mol and the C5 bead ($\epsilon_{ij} = 3.1$ kJ/mol) is relatively less hydrophobic in nature while hydrophilic P5 bead is most attractive ϵ_{ij}=5.6 kJ/mol bead among all beads. Therefore, we have constructed the

hydrophobic and hydrophilic supports based on the above parameters and have checked their effect on the water droplet. We have also modified the parameters to tune the hydrophobicity/hydrophilicity of these support beads and performed MD simulations of whole system consisting of the support, DPPC and water beads.

The non-bonded terms in the Martini force field are modeled by pairwise Lennard-Jones (LJ) interactions and cross terms σ_{ij} and ϵ_{ij} are defined by combination rule of geometric mean. The hydrophobic supports were constructed by considering the most hydrophobic bead. Type C1 is the most water repulsive bead in the Martini force field, represented by $\epsilon_{ij} = 2.0$ kJ/mol. We have constructed the support with beads with hydrophobicity more than C1 ($\epsilon_{sw} < 2.0$ kJ/mol) beads (see Figure 7.1).
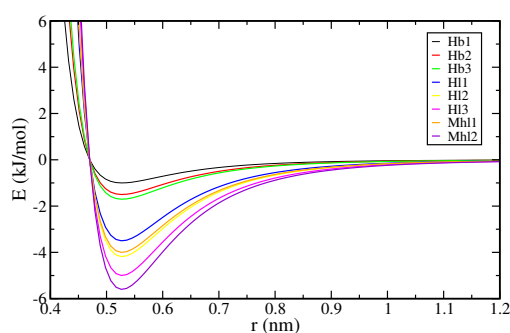
FIGURE 7.1: Lennard Jones potential between water and surface beads. Colors black, red, green, blue, yellow, magenta, orange and violet represents systems Hb1, Hb2, Hb3, Hl1, Hl2, Hl3, Mhl1 and Mhl2 respectively

The strength and reliability of the hydrophobicity of the support were further checked by performing water droplet simulations. Water droplet simulations were performed on model support made of four layers of fixed particles (S) positioned on a square grid separated by 0.3 nm distance. This results in the adjacent support beads of 0.47 nm radius and diagonally placed beads to overlap on each other, hence leaving no gap in the support thereby not allowing any water bead to pass through it. However, the support-support bead interactions were turned off in all the simulations. The dimension of the support was 12.6 nm×12.6 nm along the XY plane (details of which are explained in the following section). We have kept additional 0.3 nm of box dimension in both X and Y direction to maintain the periodicity of support beads without superimposition. A semi-hemispherical water droplets of 4580 water beads were then simulated on six different supports with $\epsilon_{sw} = 1.0$ kJ/mol, $\epsilon_{sw} = 1.5$ kJ/mol, $\epsilon_{sw} = 1.7$ kJ/mol, $\epsilon_{sw} = 1.8$ kJ/mol, $\epsilon_{sw} = 2.0$ kJ/mol and $\epsilon_{sw} = 5.0$ kJ/mol. The σ values for all the beads were chosen as 0.47 nm as in the Martini force field. The droplet simulations were performed for 60 ns and wetting or dewetting of the supports were quantified by calculating the number of water beads coming into the contact (with in 1 nm from support) with support surface as a function of simulation time (Figure 7.2a).
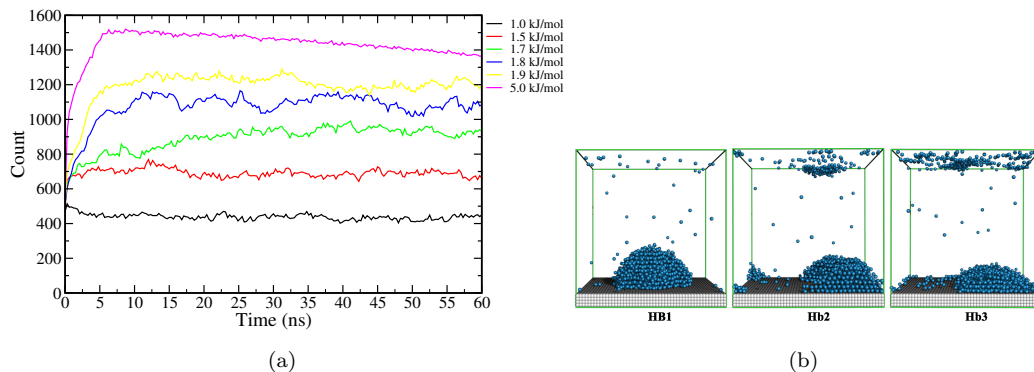
FIGURE 7.2: (a) Water beads count near the support (b) final snapshots after 60 ns simulation.

The wetting of the support surface indicates the hydrophilic nature of the support beads and it is accounted from the number of the water beads in contact with support. Similarly, the lesser count of water in support surface contact indicates the hydrophobic nature of the support. The wetting of the support surface can also be visualized from the droplet spreading depicted in Figure 7.2b. From Figure 7.2a, we have shown that the supports with ϵ_{sw}= 1.0 kJ/mol (Hb1), ϵ_{sw}= 1.5 kJ/mol (Hb2) and ϵ_{sw}= 1.7 kJ/mol (Hb3) retains the droplet structure and does not wet the surface. A rise in the number of water beads near the support is observed beyond ϵ_{sw}= 1.7 kJ/mol which indicates the hydrophilic nature of supports. Hence beads with ϵ_{sw}= 1.0, 1.5 and 1.7 kJ/mol were considered as hydrophobic and used to construct the support for lipid self-assembly simulations. The final snapshots of the water droplets simulations are depicted in Figure 7.2b for hydrophobic supports which are denoted as Hb1 ($\epsilon_{sw} = 1$), Hb2 (ϵ_{sw}=1.5) and Hb3 (ϵ_{sw}= 1.7). Moreover, we have also constructed the supports with support-water interaction parameter (ϵ_{sw}) higher than of hydrophobic (ϵ_{c1w}) interactions in Martini force field [158–160]. The supports are hydrophilic in nature due to the ϵ_{sw} used and as confirmed from the droplet simulations (See Figure 7.2a). These hydrophilic supports are denoted as Hl1 (ϵ_{sw}= 3.5 kJ/mol), Hl2 (ϵ_{sw}= 4.18 kJ/mol) and Hl3 (ϵ_{sw}= 5 kJ/mol), where Hl3 is the most hydrophilic systems considered here. The surface-water interactions are carefully chosen for all hydrophobic and hydrophilic systems except Mhl1 and Mhl2 (described below) (Table 7.1) which are taken from Martini.

For Mhl1 and Mhl2 we have used Nda and P5 types of Martini beads which are commonly used to represent hydrophilic support in supported lipid bilayer simulations. Lin X. *et al.* has studied the properties of the lipid membrane on the hydrophilic support made of Nda type beads [247]. In the present study, the Nda type surface bead is represented as Martini hydrophilic bead (Mhl1). Additionally, we have considered P5 beads to represent the most hydrophilic Martini support (ϵ_{sw}=5.6 kJ/mol) and termed as system Mhl2. It exhibits higher interactions with water compared to rest of the beads. Hence, as

TABLE 7.1: Non-bonded interaction strength (ϵ_{ij} in kJ/mol) between the particles.

System	Surface-Water	Surface-Head	Surface-Tail	Head-Head	Tail-Tail
Hb1	1.0	0.83	0.83	3.5	3.5
Hb2	1.5	1.25	1.25	3.5	3.5
Hb3	1.7	1.42	1.42	3.5	3.5
Hl1	3.5	2.92	2.92	3.5	3.5
Hl2	4.18	3.5	3.5	3.5	3.5
Hl3	5.0	4.18	4.18	3.5	3.5
Mhl1	4.0	4.0	2.0	3.5	3.5
Mhl2	5.6	5.0	2.0	3.5	3.5

described above in total we have constructed eight systems with different model supports based on the interaction with water beads ϵ_{sw} ranging from 1.0 kJ/mol to 5.6 kJ/mol given in the Table 7.1 and as depicted in Figure 7.1.

The interaction between the support and the rest of the beads was carefully parameterized. Initially, we have calculated the interaction parameters (ϵ_{ss}) from the desired ϵ_{sw} by solving the geometric mean combination rule (equation 1). Further, the interactions of the surface beads with other beads are calculated e.g., interactions between support and lipid head-group beads (NC3) are calculated by using equation 2. We did not consider the support beads to interact among themselves.

$$\epsilon_{ss} = \frac{\epsilon_{sw}^2}{\epsilon_{ww}^2} \tag{7.1}$$

$$\epsilon_{sNC3} = \sqrt{\epsilon_{ss} \times \epsilon_{NC3.NC3}} \tag{7.2}$$

Where ϵ_{sw}, ϵ_{ss} and ϵ_{sNC3} are the interactions between support-water, support-support and support-lipid head-groups respectively.

The hydrophobicity of the support here is defined in terms of the interaction parameter between support with water beads. The interaction strength computed from combining (using geometric mean) epsilons for support and tail beads is relatively lesser than of support and water beads (see Table 7.1). Therefore, the support favors interacting with water than lipid tail beads. As a consequence of the choice if parameters in this work we did not observe the formation of lipid monolayer on a hydrophobic surface. Therefore, it is evident that the hydrophobic supports we have considered in this work cannot be termed as super-hydrophobic [251, 255–259] rather moderately hydrophobic with respect to water. Therefore, as a test case we have performed simulations with support and lipid

tail beads interaction higher than support water bead(Table 7.2), which resulted in the formation of monolayer on the support (see Figure 7.3).

TABLE 7.2: Non-bonded interaction strength (ϵ_{ij} in kJ/mol) between the particles for system Hb3.

System	Support	Water	Head	Tail
Support	-	1.7	1.42	3.5
Water	1.7	3.8	5	2
Head	1.42	5	3.5	2
Tail	3.5	2	2	3.5
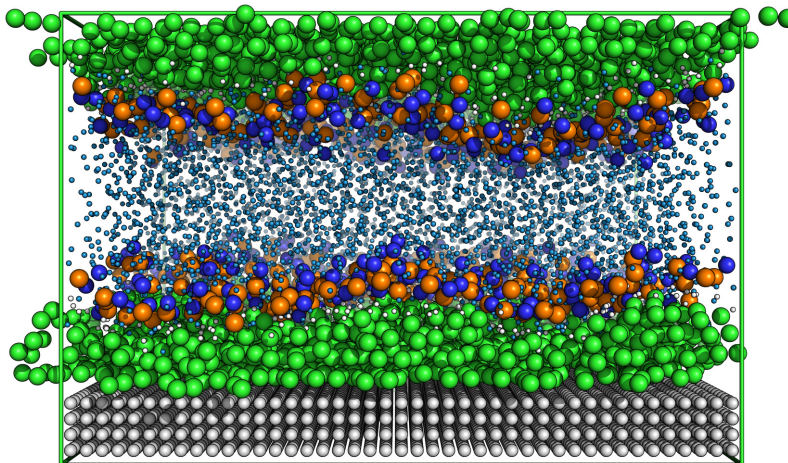
FIGURE 7.3: Final snapshots after 1μs simulation.

7.2.1   Simulation details

We have constructed the support with completely fixed beads positioned on a square grid of 0.3 nm for the droplet and self-assembly simulations. The X and Y dimensions of the support were carefully chosen to commensurate the resultant surface area of the self-assembled DPPC bilayer. The equilibrium area per headgroup (APL) of free-standing DPPC bilayer is 62.4 Å^2. Therefore, considering this, we have chosen box dimension of 12.9 nm×12.9 nm (including 0.3 nm to avoid superimposition of support beads due to periodic boundary condition) along the X and Y directions to accommodate 512 DPPC molecules to form bilayer.

It is observed that, the freezing temperature of coarse grained martini water is higher compared to the real water (or atomistic water) and it freezes rapidly when simulated

with solid surfaces [260]. The surface acts as a nucleation site which drives the rapid freezing of coarse grained water near the surface. To tackle such situations, Marrink *et al.* introduced an extra bead called anti-freeze particle (BP4) in the force field to prevent the freezing of water [159]. These beads interact (because of high σ_{ij} and ϵ_{ij}) with water beads which disturbs the ordering of coarse grained water beads. However the use of anti-freeze particles were not that promising while dealing with the surfaces as reported by Xing *et al.* [245]. Therefore, they have used the weaker water model proposed by Bennun *et al.* [260]. Bennun *et al.* manually reduced water-water interaction and iteratively tested the relationship between the water-water potential and water freezing. They have found that the scaling of ϵ_{ww} to 76% of original value prevents the freezing of water and reproduces the properties close to bulk water. However, there are some disadvantages of this weaker water model dealing with bilayer simulation. Lamberg *et al.* [261] recently showed, how the equilibrium area per lipid increases with weaker interactions between water molecules.

For the self-assembly of lipids, we have used the water model proposed by Bennun *et al.* [260] and were able to reproduce the results of free standing lipid bilayer [245](not shown here). From this simulations, we have calculated the area per headgroup of the free standing bilayer (76.0 Å^2) which is same as reported by Xing *et al.* [245]. Finally the same water-water interaction (i.e. scaled ϵ_{ww} to 76% of the original value of Martini forcefield) was used for all the self-assembly simulations on eight different supports mentioned before. We have performed self-assembly simulations of lipids starting from randomly placed 512 DPPC lipid molecules on support. Interestingly, we observed that the system assembled into two distinctly separate lipid domains after 500 ns of the simulation. 456 out of 512 lipids molecules were aggregated together and formed lipid bilayer, whereas, 56 lipids were observed to form a small lipid cluster in a simulation box away from the bilayer. Same segregation was observed even by repeating the self-assembly simulation starting from scratch i.e, initial structure (randomly placed DPPC and water molecules). In fact similar trend was observed when we have transferred a well equilibrated free standing lipid bilayer on the support and carried out simulations for 500 ns (Figure 7.4).

The segregation occurred due to the decrease in water density resulting from the 76% scaling of water-water interaction which affects the interfacial tension between lipid-water and the amount of water in the interface. The bilayer was observed to expand to a new equilibrium area per lipid (measured value of 76 Å^2) [245, 261].

Henceforth, all the self-assembly simulations on supports were performed with 456 lipid molecules solvated in water starting from a random configuration. The simulations were performed using NAP_zT ensemble by keeping the area constant along the bilayer plane (XY) and constant pressure of 1 bar along z axis. The pressure along Z-axis was
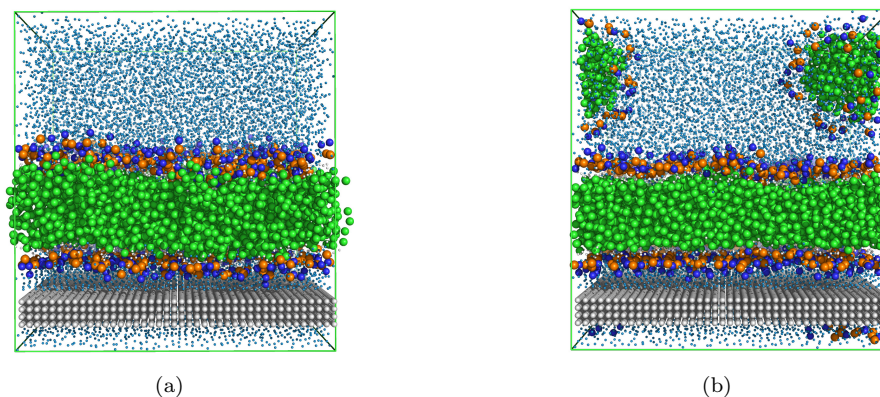
FIGURE 7.4: Snapshots of (a) initial and (b) final configurations after 500 ns.

controlled by Berendsen barostat. All the simulations were carried out at 323 K which is just above the chain melting temperature of DPPC. The temperature was kept constant by using V-rescale thermostat with temperature scaling factor of 1.5 ps. The cut off for non-bonded Coulombic interaction was r_c= 1.2 nm and the force was smoothly shifted to zero at cut-off. Similarly, the Lennard-Jones potential was shifted smoothly to zero starting from r_s= 0.9 nm. All the systems were simulated for 1 microsecond with a timestep of 15 fs. All the systems were simulated thrice with different initial random configurations of DPPC. Final snapshots of the all these systems are presented in Figure 7.5. We have developed analysis codes which are described in the results and discussion section.
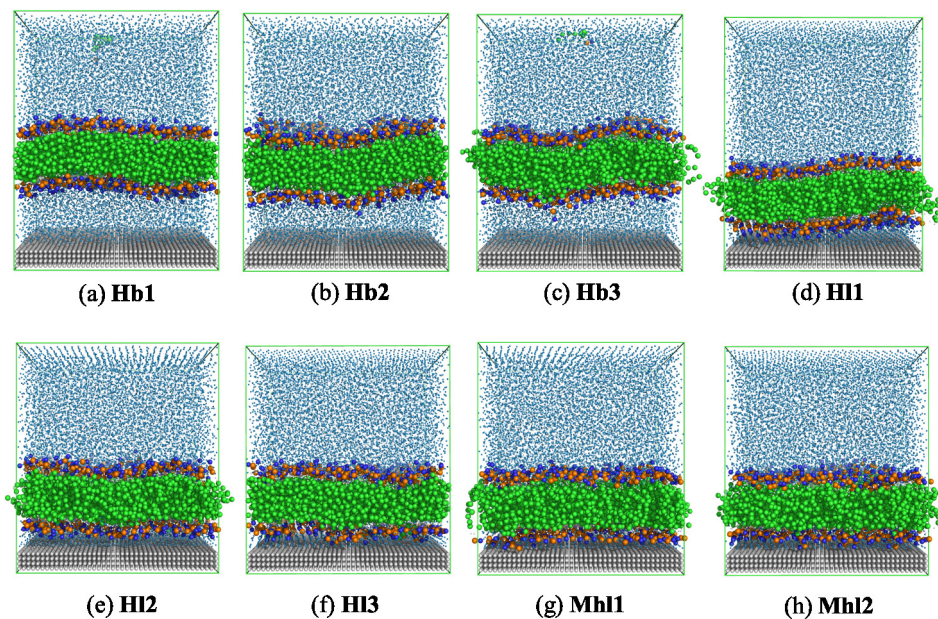
FIGURE 7.5: Final snapshots after the 1μs simulation.

7.3   Results and discussions

7.3.1   Density profile

We have calculated the partial densities of water and lipid along the bilayer normal (z axis) for all self-assembled systems. The density profiles are plotted separately for hydrophobic and hydrophilic support systems in Figure 7.6a and b respectively. It is reported that the surface acts as a nucleation site for Martini water beads, which induces water to freeze rapidly near the proximity [260, 262]. Therefore, a clear ordering of the coarse grained water near all the support surfaces is observed.

A relatively higher ordering of the water near the hydrophilic than hydrophobic support is observed due to stronger attractive interactions (see Figure 7.6b). The observed bulk water density $\sim 900 kg/m^3$ (Figure 7.6a and b) with scaled interactions is in good agreement with work by Xing *et al.* [245] Interesting thing we have noticed is that, the location of the self-assembled bilayer in simulation box is guided by the hydrophobic or hydrophilic nature of the support. In case of the hydrophobic supports, the repulsive interaction between lipid head group and support which resulted into bilayer formation away from the surface. However, the formation of bilayer proceeds due to the contributions from inter-lipid and lipid-water interactions. In case of hydrophilic support, surface beads attract the head group beads of amphiphilic lipid and the formation of bilayer takes place near to the support. We have calculated the center of mass (CoM) distance between the lipid bilayer and support as a function of interaction parameters and depicted in Figure 7.6c and d. We have observed that the bilayers formation takes place near the hydrophilic support than the hydrophobic, because of the higher attractive interactions between head-groups and the support.

We have also computed two-dimensional density map of water averaged over the Y axis to visualize the density of water across the simulation box. The density maps were calculated from last 50 ns of total 1 μs trajectory. The ordering of water near the surface is clearly visible from Figure 7.7 and it is also seen from the partial density profiles in Figure 7.6. However, the density of water near the surface is apparently higher in case of hydrophilic supports compared to the hydrophobic. The hydrophilic solid support enhances water ordering upto ~ 2.8 nm (six dense water layers) from the surface. The ordered water layers upto ~ 1.5 nm are observed for hydrophobic supports but are less dense compared to hydrophilic supports which is also noted from the partial density plots (Figure 7.6).

(a)   (b)

(c)   (d)
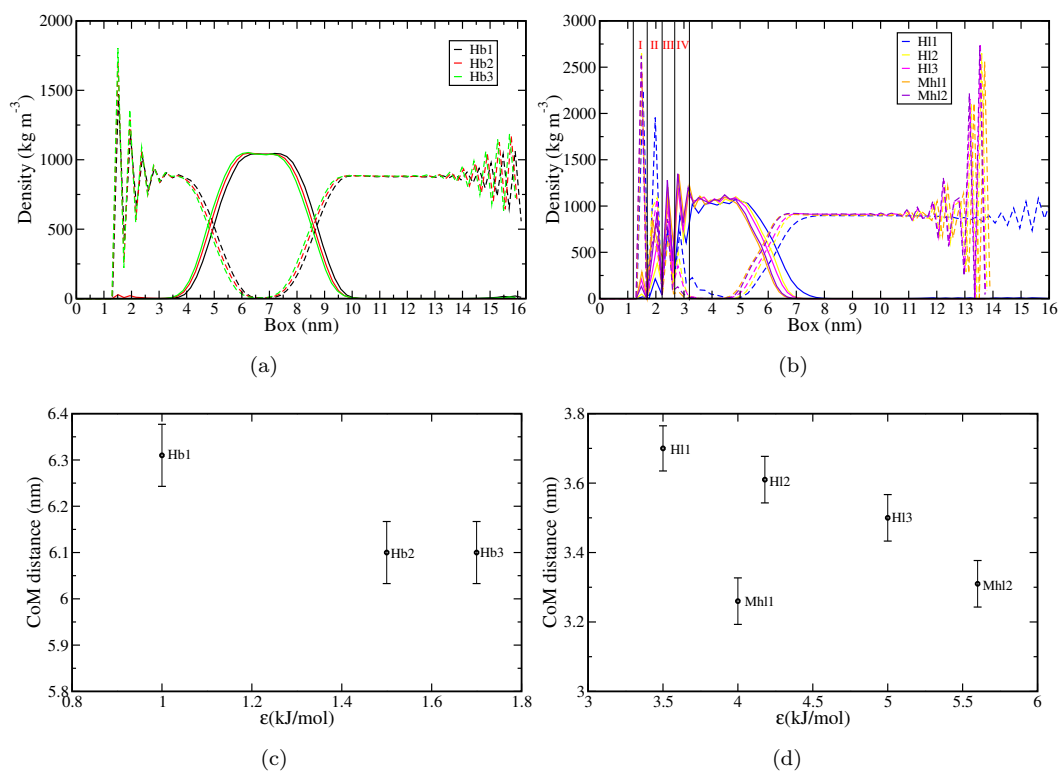
FIGURE 7.6: Partial densities of water (dashed lines) and lipid (solid lines) for (a) hydrophobic and (b) hydrophilic support system. (c) and (d) shows the center of mass distance between support and lipid bilayer from hydrophobic and hydrophilic support systems respectively.
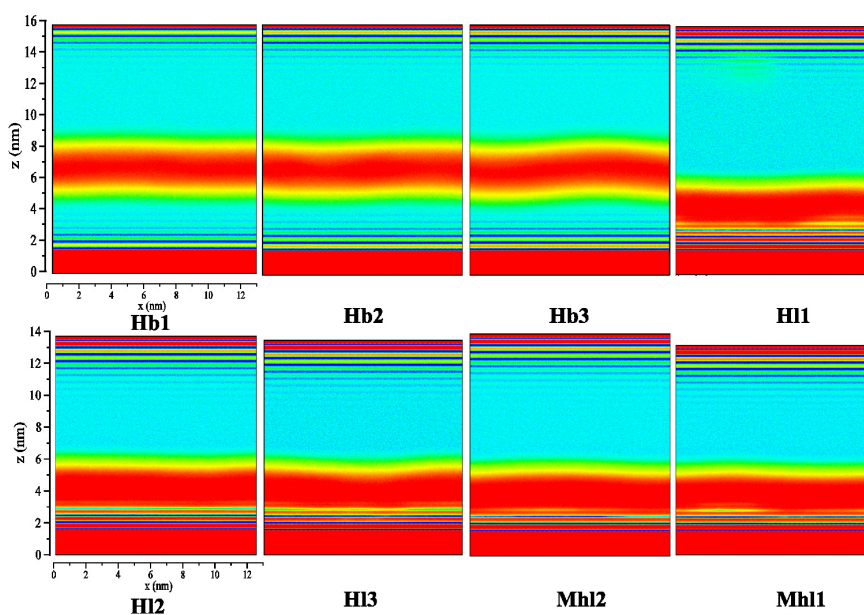
FIGURE 7.7: Two dimensional density map of water.

7.3.2 Diffusion

It is observed that lipid molecules in a supported bilayer system show slower diffusion as compared to the unilamellar vesicles [263]. Thus, we have examined the dynamics of the lipid molecules by calculating mean squared displacement (MSD) of CoM of each lipid molecule. Figure 7.8a, shows the average MSD computed at an interval of 5 ns each from last 50 ns trajectory (the lipids are already in self-assembled bilayer form). From this figure (Figure 7.8a), it is evident that the diffusion of the lipid is strongly affected in case of hydrophilic supports. The attractive force from the support significantly reduces the mobility of lipids. We have also observed that the strength of hydrophilicity of the support has an effect on the lipid mobility. From the diffusion coefficient values provided in Table 7.3 and MSD plots (Figure 7.8), it is clear that hydrophilic supports Hl3 and Mhl2 can slow down the dynamics of lipid molecules by $\sim 50\%$ of any hydrophobic system. However, by construction Hl1 system is a borderline between hydrophobic and hydrophilic support, so it is evident that the decrease in diffusion is not much.

TABLE 7.3: Diffusion coefficient

	DPPC $\times 10^{-7}\ cm^2/s$	$NC3_{lower}$ $\times 10^{-7}\ cm^2/s$	$NC3_{upper}$ $\times 10^{-7}\ cm^2/s$
Hb1	1.21±0.16	1.05±0.18	1.27±0.08
Hb2	1.10±0.20	1.02±0.17	1.13±0.18
Hb3	1.09±0.25	0.95±0.15	1.17±0.11
Hl1	0.95±0.21	0.64±0.28	1.11±0.18
Hl2	0.81±0.15	0.451±0.09	1.01±0.12
Hl3	0.59±0.07	0.23±0.05	0.82±0.11
Mhl1	0.70±0.11	0.437±0.10	0.80±0.09
Mhl2	0.55±0.06	0.20±0.03	0.74±0.05

The lower leaflet (i.e. near to the support) of self-assembled bilayer on support interacts more with the surface beads than outer leaflet. Therefore, we have investigated the effect of hydrophilicity on lipid leaflets separately. The MSD of the lipid head-group beads (NC3) are calculated based on the leaflets. Figure 7.8b depicts the leaflet-wise averaged MSD from 5 ns time interval as a function of time. The diffusion coefficients computed from the slope (linear region) are listed in Table 7.2. The lower leaflets of hydrophilic supports are severely slowed down because of higher interaction than the upper leaflets. We can even observe significant arrest of motion of lipid headgroups for Hl1 support. Both, Hl3 and Mhl2 supports exhibit $\sim 80\%$ decrease in diffusion of headgroups (NC3) compared to the most hydrophobic system (HB1). Interestingly,
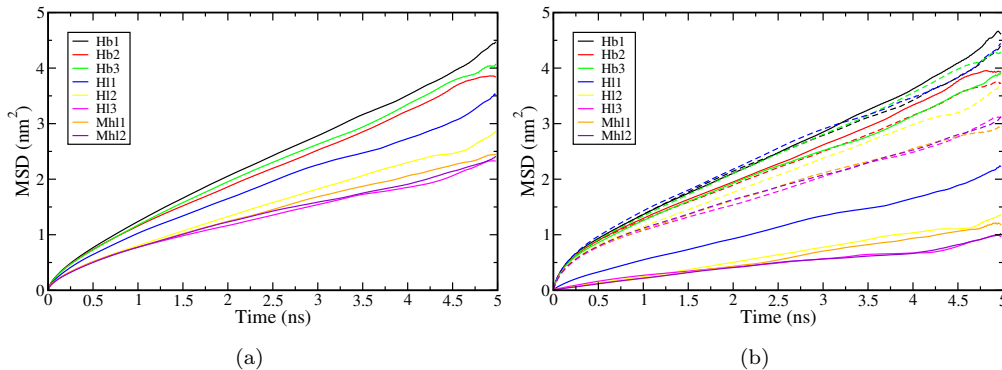
FIGURE 7.8: (a) Mean square displacement (MSD) of lipids. (b) MSDs of NC3 beads of lower leaflet lipids as dashed lines whereas NC3 beads from upper leaflet showed as solid lines.

we do not observe any significant effect of the hydrophobic surface on the diffusion of headgroups either in lower or upper leaflet of the bilayer as they are free from any substrate interactions. The diffusion coefficient values for hydrophobic supported bilayers are in good agreement with the experimental diffusion coefficient of free standing lipid bilayers ($D = 1.0 \times 10^{-7} cm^2 s^{-1}$ to $1.5 \times 10^{-7} cm^2 s^{-1}$) [160, 264–266].

7.3.3 Lipid order

Lipid tail order parameter is a measure of lipid ordering and their packing in the bilayer. The bilayer property such as fluidity, is dependent on ordering of lipid tail. The order parameters for coarse grain lipid beads used in our simulations can be calculated by the following equation.

$$P2 = 0.5 \times (3 \times < cos^2(\theta) >) - 1 \tag{7.3}$$

where θ is the angle between the bonds of two adjacent beads and bilayer normal. The value of P2=1 denotes the perfect alignment of the lipid with the bilayer normal, P2=-0.5 is anti-alignment and P2=0 represents the random orientation of lipid beads.

We have calculated the order parameters of self-assembled lipids both on hydrophilic and hydrophobic supports and plotted in Figure 7.9a. In Figure 7.9a black line denotes the lipid tail order parameter for a free standing lipid. We have plotted average lipid tail order parameters separately for upper (red dashed line) and lower leaflet (red solid line) i.e., the layer near to the support. The numbering in the x-axis (of Figure 7.9a) denotes the bond number connecting consecutive tail beads. The number 1 denotes the bond which is connecting the Glycerol moiety to the next nearest bead (Figure 7.9b)(e.g. bond 1 is GL1-C1A) and 4 is the farthest. In case of hydrophobic support, we did not observe

a significant change from free standing lipid, which may be obvious, as the self-assembly happens at a larger distance from the support compared to hydrophilic support.
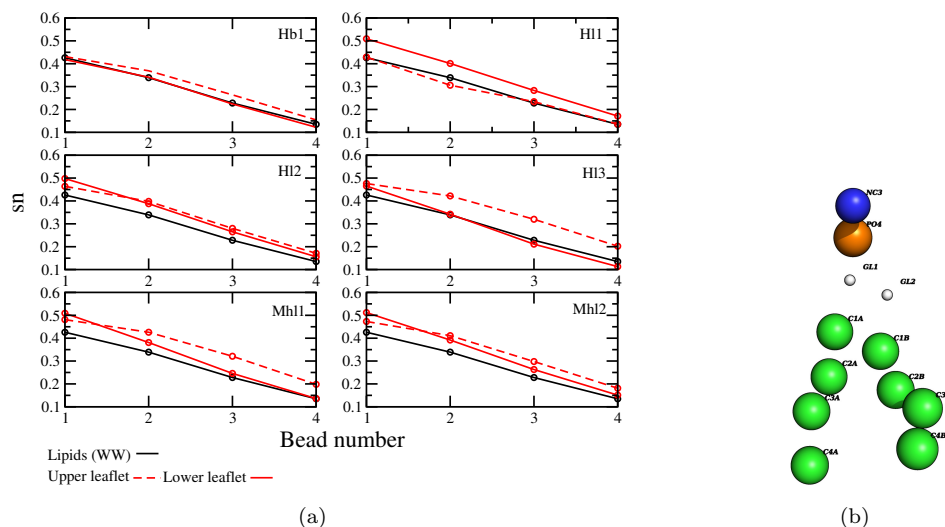
FIGURE 7.9: (a) Lipid order parameters. Black solid line represents free standing lipid tail order parameters and red dotted and solid lines are upper and lower leaflet of supported bilayers (b) schematic representation of DPPC lipid.

However, for hydrophilic support, the upper leaflet of all the systems (except Hl1) gets affected and their ordering gets increased. Hl1 is the border line case, where hydrophilicity of support is not as much as other systems, thus the upper leaflet is almost free from any interaction due to the support and shows similar trend as free standing lipid. We have observed a significant differences in ordering of the upper and lower leaflet with the increase in the hydrophilic nature of the support (e.g., Hl2, Hl3, Mhl1, Mhl2). Because of interaction with support and water beads, the lower leaflet is mostly less ordered than the upper leaflet. Even for the most hydrophilic systems (i.e., Hl3 and Mhl2), the ordering of lower leaflet crosses the free standing lipid. It is interesting to observe that the surface hydrophilicity enhances the ordering of the leaflet which is not interacting (upper leaflet) and decreases the ordering of the interacting leaflet.

7.3.4 Mechanism of self-assembly

Self-assembly is a random chemical process that involves with the arrangement of molecules from a disordered state to an organized macroscopic structure or pattern. In lipid self-assembly, lipids arrange themselves together to form lammellar, micelle or vesicular structures depending on the chemical environment, composition and concentration. It is a result of hydrophobic interactions along the lipid tails, as they try to minimize the contact with aqueous solvent and lipid headgroups pointing outside facing water molecules. During the self-assembly of lipids, it is expected that the hydrophobic

interactions bring lipid tails (C1 beads) together and the hydrophilic interaction drives NC3 beads (lipid head groups) to come closer. In the present study, we focus on the self-assembly of the lipids in presence of supports as a function of simulation time by checking the proximities of hydrophilic and hydrophobic entities. From the trajectory, we have calculated the number of NC3 beads coming in contact with each other as a function simulation time. We have calculated inter NC3 bead distances and counted the number of beads within 0.9 nm cut-off. This cut-off mainly takes care of the DPPC area per head-group (76 $\mathring{A}^2$) and counts the adjacent lipids.
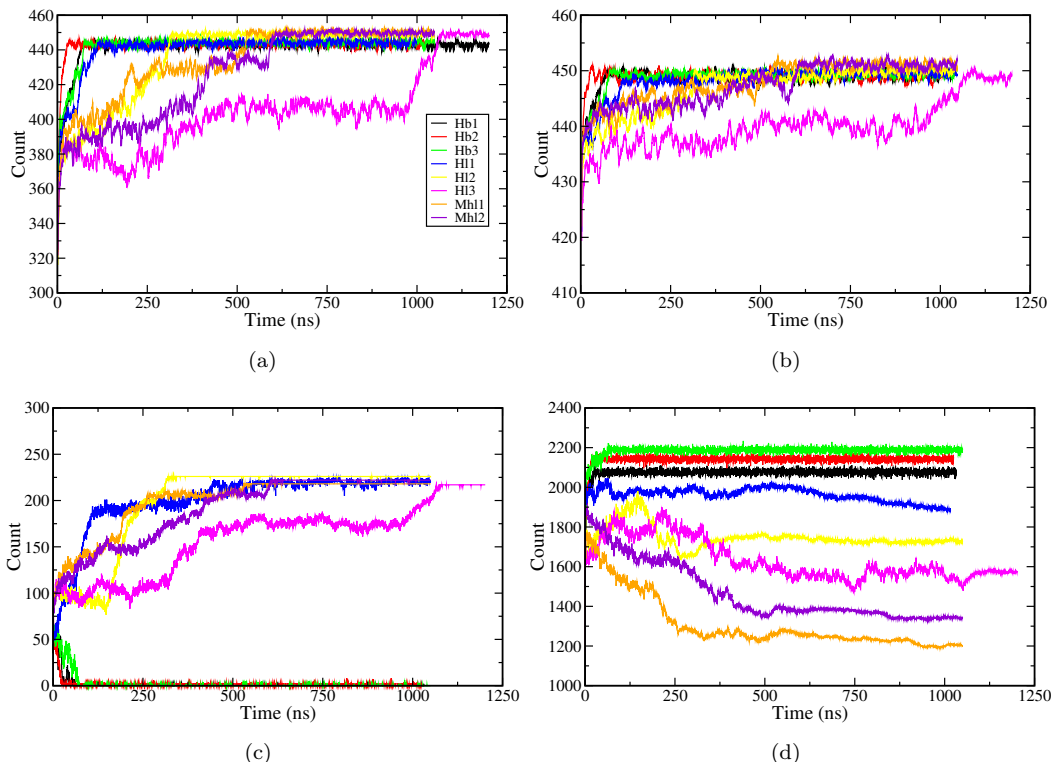
FIGURE 7.10: Number of beads within 0.9 nm distance cut-off of intra (a) NC3 bead and (b) C1 beads distances as a function of simulation time. Figure (c) and (d) shows the number of NC3 and W beads near the support respectively.

In Figure 7.10a, we have plotted this count as a function of time which shows a significant difference in case of lipid which are on hydrophilic support. Similarly, to quantify the collapse due hydrophobic interactions, we have computed the number of lipid tail (terminal C1 beads) coming together as a function of time. We have used the same cutoff of 0.9 nm to calculate the count (see Figure 7.10b). From Figure 7.10a and b, it is evident that in case of Hb1, Hb2 and Hb3 systems, lipids self-assemble within initial few nanoseconds ($\sim 20 - 80$ ns) (Figure 7.11).

Both head and tail group lipid beads have come together in a similar time frame. On the contrary, self-assembly of lipid beads have taken longer time on hydrophilic supports. In case of Hl3 system, the lipid molecules taken the longest time ~ 1000 ns to get settled on

(a)   (b)

(c)
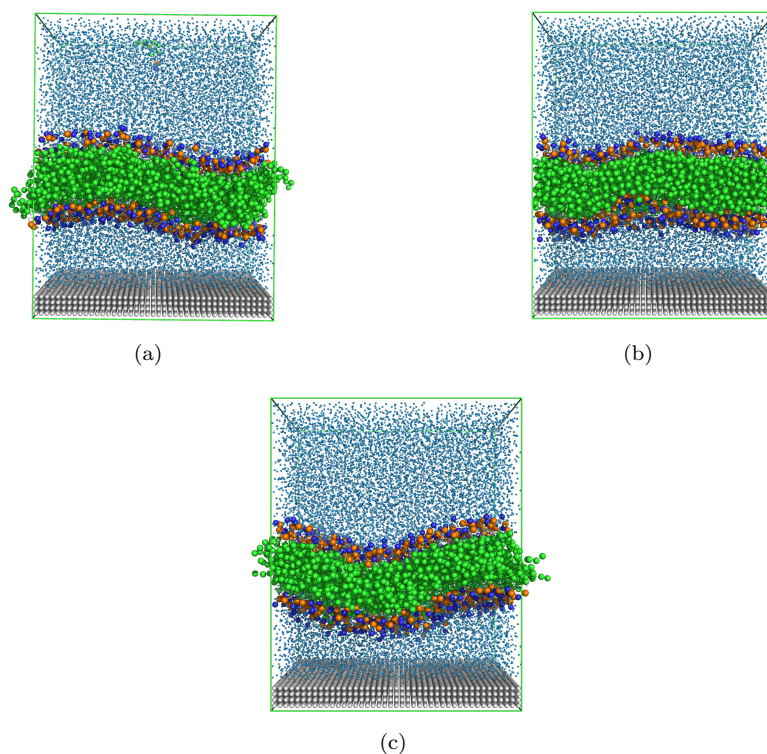
FIGURE 7.11: Snapshots after 80ns for the systems (a) Hl1, (b)Hl2 and (c) Hl3 respectively.

the support surface. This essentially occurs due to the competitive forces acting among the support, water and lipid.

The repulsive or the attractive interaction from the support can assist or delay the self-assembly process. However, in all cases we have observed self-assembly. Now, it was important to understand the interplay between the interactions of lipid and water with the support. The question was, how these inter-particle forces guide the self-assembly of lipids. For that, we have calculated the number of lipid head-groups (NC3) and water beads in the close vicinity of the support as a function of simulation time. We have taken a cut-off of 2.5 nm (from the first layer of surface beads), because the location of the bilayer-water interface from the support surface (see Figure 7.6) falls within that range. The NC3 and water bead counts as a function of time plotted in Figure 7.10c and d respectively. As we have started the simulation from randomly distributed molecules we have observed clearly that in case of Hb1, Hb2 and Hb3 supports, the NC3 beads move away from the surface and count reaches to zero in a very short time span of $\sim 20 - 80$ ns. On the other hand, hydrophilic supports induces the lipid molecules to settle down near all the surfaces due to attractive interactions.

The hydrophilic support imparts a strong interaction towards water beads. It is evident from Figure 7.10d that, there is a decrease in the number of water beads near hydrophilic

support. This might be possible because the head-groups (NC3) also favor to interact with hydrophilic support beads. As a result, NC3 beads get accumulated near hydrophilic support competing with water. However, from the two-dimensional density maps (Figure 7.7), we have seen that the density of water near to the surface is higher in case of hydrophilic support than hydrophobic support. In the hydrophilic support systems, the interaction potentials ϵ_{sw} are more attractive than ϵ_{s-NC3} (Table 7.1), therefore water beads settle more in number near to the support surface. Besides that, the support acts as a nucleation site, thus, favors waters bead to arrange near the surface. However, approximately within 2.5 nm (see Figure 7.6 for the partial density of water near hydrophilic support) from the hydrophilic support, there is a competition between lipids and water for finding the position after the initial deposition of the water adjacent to the support. However, apart from this, there are also inter-particle interactions other than surface contributing to the lipid self-assembly. It includes inter-lipid, lipid-water and water-water beads interactions. E.g., in Hl1 system, the support beads interact with water with $\epsilon_{S-W} = 3.5$ kJ/mol, water-water interaction strength is $\epsilon_{W-W} = 3.8$ kJ/mol. Further, the nucleation of the water allows these interactions to overcome the support-head group ($\epsilon_{NC3-S} = 2.92$ kJ/mol) (see Table 7.1) and hence accelerates water beads to settle near support surface. Beyond the non-bonded cut-off from support, we have found ϵ_{NC3-W} interactions dominate which helps in the self-assembly process. Therefore, we have observed a sharp rise in the NC3 count for all hydrophilic support (Figure 7.10c).

However, it was still unclear that, why the number of water molecules near hydropholic support (expect Hl1 system) decreases with time, even though the water densities are higher near hydrophilic supports (2.5 nm from the support surface). Apparently for hydrophobic support systems, we have observed a higher number of water beads resides in the 2.5 nm cut-off from the support surface. This mainly resulted due to the formation of bilayer that takes place away from the support. Interestingly, the number of water beads gradually increases with the interaction parameters (ϵ_{sw}) for hydrophobic support with water. The water density increases as the support attracts more water with increase in hydrophilicity

To address the anomaly of the lesser water bead count near hydrophilic supports (Hl2, Hl3, Mhl1 and Mhl2) compared to hydrophobic support. We have calculated the partial densities of water and head-group beads (NC3) near the hydrophilic support (within the cutoff of 2.6 nm). As the amphiphilic lipids are settling down near the surface, it is expected that lipids may be replacing some of the water beads. In Figure 7.12, we have plotted the partial density of the water and NC3 groups during self-assembly (i.e. initial 0 - 50 ns) with an interval of 10 ns.
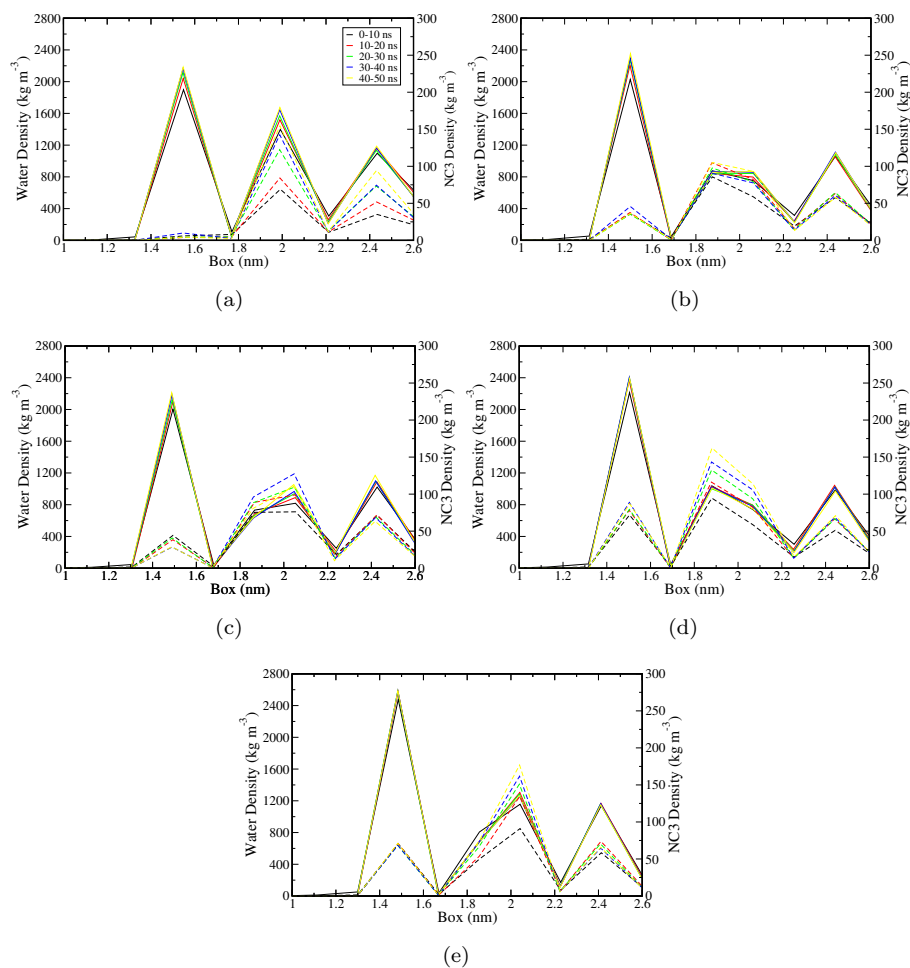
FIGURE 7.12: Partial densities of water (solid lines) and NC3 beads (dashed lines) as a function of time interval of 10 ns each. (a), (b), (c) and (d) represents system Hl2, Hl3, Mhl1 and Mhl2 respectively.

The 1st layer of water has a higher density than other layers for all the hydrophilic systems. However, the number of water beads in the second and third layers varies and we have observed a significant number of NC3 beads have penetrated these two water layers. This is because of favorable water - NC3 bead interaction parameter and competition between water and NC3 bead to settle down near the surface. Thus, we have seen lesser water bead counts in proportional to the hydrophilicity of the support. The maximum density of NC3 is noted in Mhl1 system due to the competitive interactions between NC3 and W with support ($\epsilon_{S-NC3}=\epsilon_{S-W}=$ 4 kJ/mol).

7.3.5   Energetics of the mechanism

We have further examined these systems by calculating the potential energy, i.e., non-bonded Lennard Jones (LJ) interaction energies experienced by lipid-head group and water beads separately in different regions near to the support surface. In case of
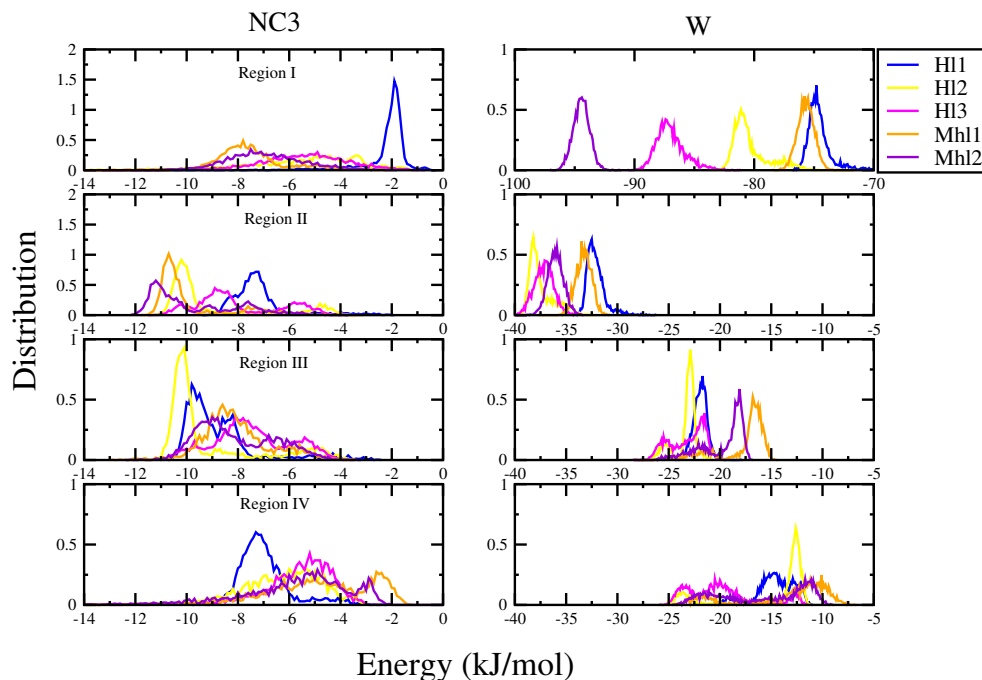
FIGURE 7.13: Potential energy (LJ) between the beads near hydrophilic supports. Left and right panels shows energies felt by water and NC3 beads respectively in different regions.

hydrophilic support we have observed the self-assembly of lipids near to the support. Therefore, here we have only reported the energies related to the hydrophilic support systems. We have observed a competition between the lipid head-groups and water beads for finding a position predominately within the distance of 2 nm from the support surface. The partial densities (Figure 7.6) also evident that, this region is the most oscillating region where water and headgroup beads are getting arranged. Hence, we have divided this region in four equal slabs (denoted as I, II, III and IV region) of 0.5 nm staring from 1.2 nm to 3.2 nm (see Figure 7.6). In these predefined regions (of self-assembled equilibrated), we have calculated the total energy (sum of non-bonded energy between water/headgroup and all other beads) by each water and headgroup bead. The energies in different regions are further plotted as a distribution in Figure 7.13.

From this Figure (right panel), it is evident that water is the most energetically favored near to the surface (region I) and then in region II. As Hl3 and Mhl2 are the most hydrophilic systems in two categories, water near to these surfaces (in region I) are energetically favorable. However, as we go further from the surface, i.e., in region II, III and IV the potential energy experienced by water of different support hydrophilicity are almost similar (overlapping distributions). However, in case of headgroup beads (NC3) the region II and III are the more energetically favorable regions. In region II and III headgroup beads get stabilized by interacting with water and support beads. The

separate energy contributions to the total energy of headgroup in these regions are given in Figure 7.14 and 7.15.

(a)   (b)
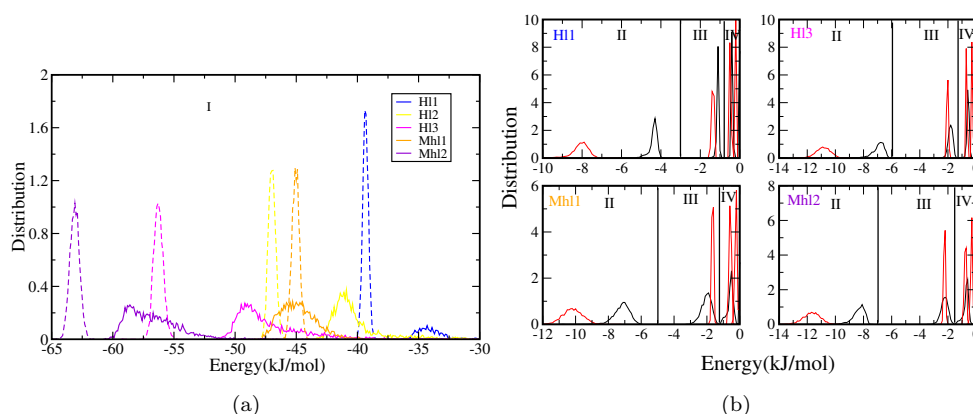
FIGURE 7.14: Potential energies between water-water beads. (a) Potential energies between the water beads falling in region I of 0-0.5 nm from support surface. Dotted and solid lines represents W-S and NC3-S interaction energies respectively and colors blue, yellow, magenta, orange and violet represents Hl1, Hl2, Hl3,Mhl1 and Mhl2 systems respectively (b) Potential energy within regions II, III and IV. Color red is W-S and black is NC3-S LJ energies.

(a)   (b)

(c)
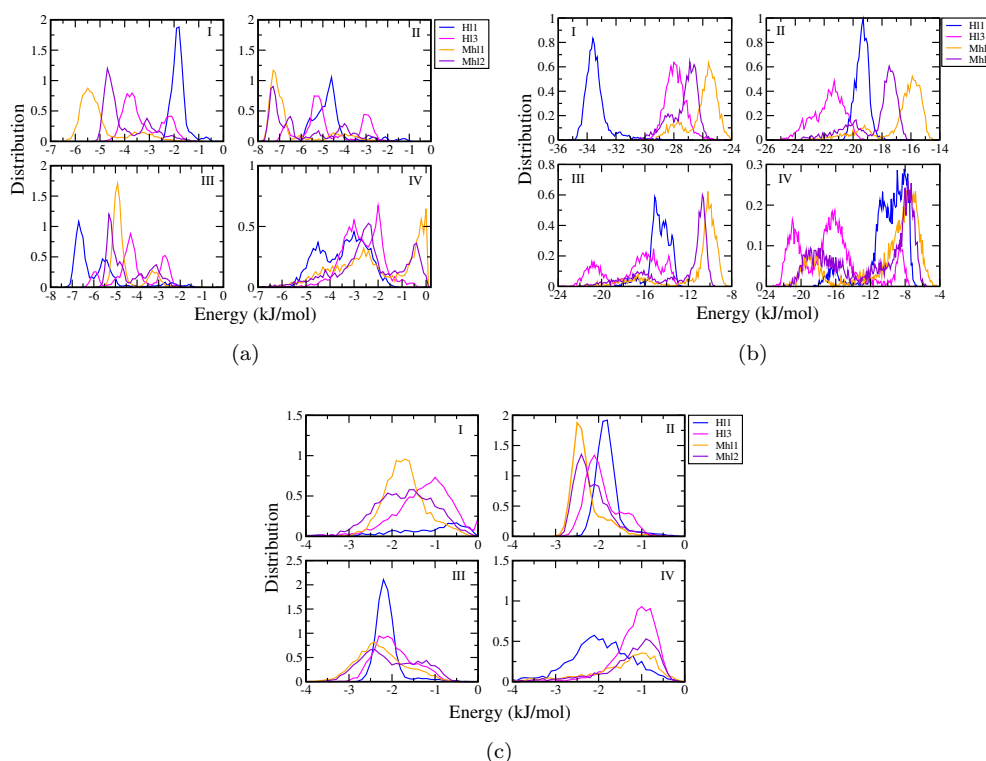
FIGURE 7.15: Potential energy between (a) NC3-water beads, (b) water-water beads and c) NC3-NC3 beads respectively. Colors blue, magenta, orange and violet represents systems Hl1, Hl3, Mhl1 and Mhl2 respectively

It is also evident from Figure 7.13 that in region II and III there are not much influence of the support on headgroup beads. In region II most hydrophilic support (Mhl2) marginally

stabilizes the headgroup beads, but in region III less hydrophilic support (Hl1, Hl2) stabilize the headgroups. In region III and IV of Figure 7.13 we observe the broad distribution of energies felt by headgroups due to varied balancing interactions from water, surface and lipid tails beads. This is one of the main reasons why we observe less ordering in lipid tail (see Figure 7.9).

These observations confirm that the lipid self-assembly with the solid supports mainly guided by the various interactions taking place between the support, lipids and water beads. The arrangement of molecules from a disordered state into organized macroscopic structures is predominantly dependent upon the properties of the support and nature of the interacting particles.

7.4   Conclusions

We have carried out the lipid self-assembly simulations on different model supports constructed on the basis of their hydrophobic or hydrophilic nature. Significant differences are noticed in all these self-assembly processes. The hydrophobic support, due to the repulsive interaction, repels the lipids and the bilayer formation observed at a distant region from the support. The lipid bilayers settle down near to the modeled hydrophilic support due to favorable attractive interactions. We have found out that the lipid bilayers from the hydrophobic support systems were least affected, whereas, the hydrophilicity of the support affects the bilayer properties to a certain extent. The ordering of lower and upper leaflets is affected in case of hydrophilic support. The hydrophilic supports are found to enhance the water ordering near the support as evident from the structural and dynamical properties of water. During the self-assembly, hydrophobic supported lipids arrange quickly to form lipid bilayer whereas the hydrophilic support delays the self-assembly process. It is mainly because of the interplay between surface-head, head-head, surface-water and head-water interactions. We confirmed the competition between water and lipid head-group to interact with hydrophilic supports by calculating energetic of the system.

Chapter 8

Conclusion

In the present study, we have investigated the various bio-molecular systems using the computer simulations. Our research is essentially adhered to the proteins and lipid simulations to understand the various physico-chemical properties of the soft matter. In this thesis, we have discussed the important aspects of enzyme mechanism of PcrA helicase and the properties of the lipid bilayers in the presence of NPs and surfaces. Acoordingly, The thesis is divided into two parts - protein and lipid membranes.

Part A of the thesis is dedicated to the understanding of the enzyme PcrA helicase and ATP binding to it. PcrA helicase functions on the basis of the binding and hydrolysis of ATP induces conformational changes in the protein, which mediate the translocation of these motors over nucleic acid and unzips it. We have essentially targeted here the process of ATP unbinding from the catalytic site and estimated the ATP binding free energy in chapter 3. The free energy required to pull ATP from the active cleft was computed to be $85kJmol^{-1}(\pm5kJmol^{-1})$. However, we have investigated the components of unbinding free energy which results from a change in conformation of residues of protein near to the binding site and because of breaking (and reformation) of hydrogen bonds between ATP and the helicase. This study has also elaborated the local conformational changes in more detail for ATP and the active site residues as a result of ATP unbinding. As a consequence of the ATP unbinding, the substrate state protein gets converted to the product state protein. Therefore, in chapter 4 of the thesis, we have simulated the substrate state and product state of the protein and observed domain motions because of flexibility in ATP free product state.

To summarize part A, we have elaborated the atomistic details of the ATP unbinding and the effect of ATP unbinding on local conformational flexibility and subsequently its effect on the global conformational change of the motor protein.

In part B of the thesis, we have studied the effect of NP and surface interactions on the properties of the lipid membrane. In chapter 5, we have investigated the effect of neutral AuNP on the membrane fluidity while chapter 6 elucidates the interactions of the neutral and octane thiol capped AuNP with the lipid bilayer.

In chapter 5, we have investigated the perturbation caused by different sized AuNP on lipid molecules locally at adsorption site (SR region) and in the region away from the NP (LR region). Significant difference in the bilayer properties is being observed for both the regions. Compared to the reference bilayer, we observed the lipid molecules in the NP bound system showed relatively lesser fluidity of the LR lipid molecules due to enhanced packing of the lipids. The different sizes AuNPs have the same effect on the bilayer. However, the magnitude of structural ordering and fluidity differs. We have investigated the effect of single NP at a time, morever the loading of higher concentration of NP will may have different effect on the membrane properties. We have observed that the AuNP interacts favorably with the interacting upper leaflet without permeating it. Therefore, in the following chapter, we have computed the free energy required for the permeation.

Besides the bare AuNP, we also used the ligand coated AuNP to study how the surface structuring affect the details of the permeation process. (in chapter 6) It was observed that the hydrophilic nature of bare AuNP favors the adsorption of NP to the bilayer but further loading becomes difficult. The estimated adsorption and loading free energies for bare AuNP are -150 $kJmol^{-1}$ and +125 $kJmol^{-1}$ respectively. For octane thiol capped AuNP loading becomes very difficult due to the hydrophobic capping and the increased size. The adsorption and loading energies computed as -30 $kJmol^{-1}$ and +500 $kJmol^{-1}$ respectively. The high energy barrier for the capped AuNP comes from the cumulative effect of hydrophobic surface coating and increased particle volume. Therefore, loading of the NP from the bilayer-water interface to the membrane interior becomes energetically unfavorable. Structurally, we observed that lipid bilayer adapts curvature around the hydrophilic bare AuNP however capped AuNP ruptures the lipid membrane by formation of pore like structures. This favors the entry for water molecules. This work can be extended by functionalizing NPs with other types of ligands e.g. charged and amphiphilic ligands which may have different permeation characteristics. The findings of the current work will lead to better understanding of the translocation mechanism of NPs across lipid membranes, which can be useful in developing efficient nano-cargos for delivery of therapeutics and better understanding of the mechanisms for cytotoxicity of some types of NPs.

We expanded our research on lipid membranes and studied the interactions of the lipid membrane with the surfaces. In chapter 7 of the thesis, we have carried out the lipid self-assembly simulations and studied the properties of the self-assembled membranes

on different model support constructed on the basis of their hydrophobic or hydrophilic nature. Significant differences were noticed in all these self-assembly processes. The hydrophobic support, due to the repulsive interaction, repels the lipids and the bilayer formation observed at a distant region from the support. The lipid bilayers settle down near to the modeled hydrophilic support due to favorable attractive interactions. We have found out that the lipid bilayers from the hydrophobic support systems were least affected, whereas, the hydrophilicity of the support affects the bilayer properties to a certain extent. The ordering of lower and upper leaflets is affected in case of hydrophilic support. The hydrophilic supports are found to enhance the water ordering near the support as evident from the structural and dynamical properties of water. During the self-assembly, hydrophobic supported lipids arrange quickly to form lipid bilayer whereas the hydrophilic support delays the self-assembly process.

Molecular simulations employed in the present study enabled us to examine the complex biomolecular assemblies in atomic detail, from the conformational motion in an individual protein to the various properties of the lipid membrane under the influence of nanoparticles and surfaces. The protein simulations in the present study have provided a better understanding of DNA unwinding mechanism by PcrA helicase. The lipid bilayer simulations elucidated the properties of the biological membrane under the influence of the nanoparticle and surfaces which certainly contribute to the development to the development of pharmaceuticals, anesthetics and drug-gene delivery agents.

Appendix A

Publications

1. Effect of Gold Nanoparticle on Structure and Fluidity of Lipid Membrane. **Mhashal AR** and S. Roy⋆, PLoS ONE 9(12): e114152. doi:10.1371/journal.pone.0114152.

2. ATP Induced Conformational Flexibility in PcrA Helicase Protein from Molecular Dynamics Simulation, **Mhashal AR**, C. K. Choudhury and S. Roy⋆, Journal of Molecular Modeling *Accepted*.

3. Self-Assembly of phospholipids on the flat model supports, **Mhashal AR**⋆ and S. Roy⋆, Phys. Chem. Chem. Phys., 2015,17, 31152-31160.

4. Permeation Free Energy of Naked and Capped Gold Nanoparticle., **Mhashal AR**⋆ and S. Roy⋆, *Under review*.

5. Investigations of Conformational and Functional Dynamics of Kallikrein in Organic Solvents, Dalal, Sayli, **Mhashal, AR** and Gaikwad, Sushama⋆, Journal of Biomolecular Structure and Dynamics, DOI:10.1080/07391102.2016.1138884.

Bibliography

[1] Bruce Alberts, Alexander Johnson, Julian Martin Raff Lewis, Keith Roberts, and Peter Walter. Molecular biology of the cell, 4th edition. *Garland Science, New York*, 2002.

[2] Robert F. Service. Nanotechnology takes aim at cancer. *Science*, 310(5751):1132–1134, 2005. doi: 10.1126/science.310.5751.1132. URL http://www.sciencemag.org/content/310/5751/1132.short.

[3] Younan Xia. Nanomaterials at work in biomedical research. *Nat Mater*, 7:758–760, 2005. doi: 10.1038/nmat2277. URL http://dx.doi.org/10.1038/nmat2277.

[4] Samir Mitragotri and Joerg Lahann. Physical approaches to biomaterial design. *Nat Mater*, 8:15–23, 2009. doi: 10.1038/nmat2344. URL http://dx.doi.org/10.1038/nmat2344.

[5] Andre E. Nel, Lutz Madler, Darrell Velegol, Tian Xia, Eric M. V. Hoek, Ponisseril Somasundaran, Fred Klaessig, Vince Castranova, and Mike Thompson. Understanding biophysicochemical interactions at the nano-bio interface. *Nat Mater*, 8:543–557, 2009. doi: 10.1038/nmat2442. URL http://dx.doi.org/10.1038/nmat2442.

[6] P. Decuzzi and M. Ferrari. The receptor-mediated endocytosis of nonspherical particles. *biophys j*, 94:3790–3797, 2008. doi: 10.1529/biophysj.107.120238. URL http://dx.doi.org/10.1529/biophysj.107.120238.

[7] Tian Xia, Michael Kovochich, Jonathan Brant, Matt Hotze, Joan Sempf, Terry Oberley, Constantinos Sioutas, Joanne I. Yeh, Mark R. Wiesner, and Andre E. Nel. Comparison of the abilities of ambient and manufactured nanoparticles to induce cellular toxicity according to an oxidative stress paradigm. *Nano Letters*, 6 (8):1794–1807, 2006. doi: 10.1021/nl061025k. URL http://dx.doi.org/10.1021/nl061025k. PMID: 16895376.

[8] Andre Nel, Tian Xia, Lutz Mädler, and Ning Li. Toxic potential of materials at the nanolevel. *Science*, 311(5761):622–627, 2006. doi: 10.1126/science.1114397. URL http://www.sciencemag.org/content/311/5761/622.abstract.

[9] Günter Oberdörster, Oberdörster, and Jan Oberdörster. Nanotoxicology: An emerging discipline evolving from studies of ultrafine particles. *Environ. Health Perspect.*, 113:622–627, 2005. doi: 10.1289/ehp.7339.

[10] Renata Behra and Harald Krug. Nanoecotoxicology: Nanoparticles at large. *Nat Nanotechnol*, 3:253–254, 2008. doi: 10.1038/nnano.2008.113. URL `http://dx.doi.org/10.1038/nnano.2008.113`.

[11] Timothy M. Lohman and Keith P. Bjornson. Mechanisms of helicase-catalyzed dna unwinding. *Annual Review of Biochemistry*, 65(1):169–214, 1996. doi: 10.1146/annurev.bi.65.070196.001125. URL `http://dx.doi.org/10.1146/annurev.bi.65.070196.001125`. PMID: 8811178.

[12] Louise E Bird, Hosahalli S Subramanya, and Dale B Wigley. Helicases: a unifying structural theme? *Current Opinion in Structural Biology*, 8(1):14 – 18, 1998. ISSN 0959-440X. doi: http://dx.doi.org/10.1016/S0959-440X(98)80004-3. URL `http://www.sciencedirect.com/science/article/pii/S0959440X98800043`.

[13] Gabriel Waksman, Erich Lanka, and Jose-Maria Carazo. Helicases as nucleic acid unwinding machines. *Nat Struct Mol Biol*, 7:20 – 22, 2000. ISSN 1. doi: 10.1038/71215. URL `http://dx.doi.org/10.1038/71215`.

[14] Kenneth J Marians. Crawling and wiggling on dna: Structural insights to the mechanism of {DNA} unwinding by helicases. *Structure*, 8(12):R227 – R235, 2000. ISSN 0969-2126. doi: http://dx.doi.org/10.1016/S0969-2126(00)00539-6. URL `http://www.sciencedirect.com/science/article/pii/S0969212600005396`.

[15] Jonathan M Caruthers and David B McKay. Helicase structure and mechanism. *Current Opinion in Structural Biology*, 12(1):123 – 133, 2002. ISSN 0959-440X. doi: http://dx.doi.org/10.1016/S0959-440X(02)00298-1. URL `http://www.sciencedirect.com/science/article/pii/S0959440X02002981`.

[16] L. E. Bird, J. A. Brannigan, H. S. Subramanya, and D. B. Wigley. Characterisation of bacillus stearothermophilus pcra helicase: Evidence against an active rolling mechanism. *Nucleic Acids Research*, 26(11):2686–2693, 1998. doi: 10.1093/nar/26.11.2686. URL `http://nar.oxfordjournals.org/content/26/11/2686.abstract`.

[17] Leah E. Mechanic, Mark C. Hall, and Steven W. Matson. Escherichia coli dna helicase ii is active as a monomer. *Journal of Biological Chemistry*, 274(18):12488–12498, 1999. doi: 10.1074/jbc.274.18.12488. URL `http://www.jbc.org/content/274/18/12488.abstract`.

[18] David J. T. Porter, Steven A. Short, Mary H. Hanlon, Frank Preugschat, Jeanne E. Wilson, Derril H. Willard, and Thomas G. Consler. Product release is the major contributor tok cat for the hepatitis c virus helicase-catalyzed strand separation of short duplex dna. *Journal of Biological Chemistry*, 273(30):18906–18914, 1998. doi: 10.1074/jbc.273.30.18906. URL `http://www.jbc.org/content/273/30/18906.abstract`.

[19] Panos Soultanas and Dale B Wigley. Unwinding the 'gordian knot' of helicase action. *Trends in Biochemical Sciences*, 26(1):47 – 54, 2001. ISSN 0968-0004. doi: http://dx.doi.org/10.1016/S0968-0004(00)01734-5. URL `http://www.sciencedirect.com/science/article/pii/S0968000400017345`.

[20] Panos Soultanas and Dale B Wigley. Dna helicases:inching forward. *Current Opinion in Structural Biology*, 10(1):124–128, 2000. ISSN 0959-440X. doi: http://dx.doi.org/10.1016/S0959-440X(99)00059-7. URL `http://www.sciencedirect.com/science/article/pii/S0959440X99000597`.

[21] Mark S. Dillingham, Dale B. Wigley, and Martin R. Webb. Demonstration of unidirectional single-stranded dna translocation by pcra helicase: measurement of step size and translocation speed. *Biochemistry*, 39(1):205–212, 2000. doi: 10.1021/bi992105o. URL `http://dx.doi.org/10.1021/bi992105o`. PMID: 10625495.

[22] Sameer S Velankar, Panos Soultanas, Mark S Dillingham, Hosahalli S Subramanya, and Dale B Wigley. Crystal structures of complexes of pcra {DNA} helicase with a {DNA} substrate indicate an inchworm mechanism. *Cell*, 97(1):75 – 84, 1999. ISSN 0092-8674. doi: http://dx.doi.org/10.1016/S0092-8674(00)80716-3. URL `http://www.sciencedirect.com/science/article/pii/S0092867400807163`.

[23] Markus Dittrich and Klaus Schulten. Pcra helicase, a prototype atp-driven molecular motor. *Structure*, 14(9):1345 – 1353, 2006. ISSN 0969-2126. doi: http://dx.doi.org/10.1016/j.str.2006.06.017. URL `http://www.sciencedirect.com/science/article/pii/S0969212606003017`.

[24] Isaac Wong and Timothy M. Lohman. Allosteric effects of nucleotide cofactors on escherichia coli rep helicase and dna binding. *Science*, 256(5055):350–355, 1992. doi: 10.1126/science.256.5055.350. URL `http://www.sciencemag.org/content/256/5055/350.abstract`.

[25] Jin Yu, Taekjip Ha, and Klaus Schulten. Structure-based model of the stepping motor of pcra helicase. *Biophysical Journal*, 91(6):2097–2114, 2006. doi: 10.1529/biophysj.106.088203. URL `http://dx.doi.org/10.1529/biophysj.106.088203`.

[26] Jin Yu, Taekjip Ha, and Klaus Schulten. How directional translocation is regulated in a dna helicase motor. *Biophysical Journal*, 93(11):3783–3797, 2007. doi: 10.1529/biophysj.107.109546. URL `http://dx.doi.org/10.1529/biophysj.107.109546`.

[27] E. Sackmann. Supported membranes: Scientific and practical applications. *Science*, 271(5245):43–48, 1996. doi: 10.1126/science.271.5245.43. URL `http://www.sciencemag.org/content/271/5245/43.abstract`.

[28] B. A. Cornell, V. L. B. Braach-Maksvytis, L. G. King, P. D. J. Osman, B. Raguse, L. Wieczorek, and R. J. Pace. A biosensor that uses ion-channel switches. *Nature*, 387(6633):580–583, 1997. doi: http://www.nature.com/nature/journal/v387/n6633/suppinfo/387580a0˙S1.html.

[29] Jay T. Groves and Michael L. Dustin. Supported planar bilayers in studies on immune cell adhesion and communication. *Journal of Immunological Methods*, 278(1–2):19 – 32, 2003. ISSN 0022-1759. doi: http://dx.doi.org/10.1016/S0022-1759(03)00193-5. URL `http://www.sciencedirect.com/science/article/pii/S0022175903001935`.

[30] M Bloom, E Evans, and OG Mouritsen. Physical properties of the fluid lipid-bilayer component of cell membranes: a perspective. *Quarterly reviews of biophysics*, 24 (3):293—397, August 1991. ISSN 0033-5835. doi: 10.1017/s0033583500003735. URL `http://dx.doi.org/10.1017/S0033583500003735`.

[31] M Bloom, E Evans, and OG Mouritsen. Structure and dynamics of membranes: From cells to vesicles. *Elsevier*, 1995.

[32] Jr. Merz, K. M. and B. Roux. Biological membranes. *Springer*, 1996.

[33] John F. Nagle and Stephanie Tristram-Nagle. Structure of lipid bilayers. *Biochimica et Biophysica Acta (BBA) - Reviews on Biomembranes*, 1469(3):159 – 195, 2000. ISSN 0304-4157. doi: http://dx.doi.org/10.1016/S0304-4157(00)00016-2. URL `http://www.sciencedirect.com/science/article/pii/S0304415700000162`.

[34] J. Katsaras and T. Gutberlet. Lipid bilayers: Structure and interactions. *Springer-Verlag*, 1996.

[35] Wendy R. Sanhai, Jason H. Sakamoto, Richard Canady, and Mauro Ferrari. Seven challenges for nanomedicine. *Nat Nanotechnol*, 3:242–244, 2006. doi: 10.1038/nnano.2008.114. URL `http://dx.doi.org/10.1038/nnano.2008.114`.

[36] Lawrence Rajendran, Hans-Joachim Knolker, and Kai CSimons. Subcellular targeting strategies for drug design and delivery. *Nat Rev Drug Discov*, 9:29–42, 2010. doi: 10.1038/nrd2897. URL `http://dx.doi.org/10.1038/nrd2897`.

[37] Partha Ghosh, Gang Han, Mrinmoy De, Chae Kyu Kim, and Vincent M. Rotello. Gold nanoparticles in delivery applications. *Advanced Drug Delivery Reviews*, 60(11):1307 – 1315, 2008. ISSN 0169-409X. doi: http://dx.doi.org/10.1016/j.addr.2008.03.016. URL `http://www.sciencedirect.com/science/article/pii/S0169409X08000999`. Inorganic Nanoparticles in Drug Delivery.

[38] Nathaniel L. Rosi and Chad A. Mirkin. Nanostructures in biodiagnostics. *Chemical Reviews*, 105(4):1547–1562, 2005. doi: 10.1021/cr030067f. URL `http://dx.doi.org/10.1021/cr030067f`. PMID: 15826019.

[39] Dan Peer, Jeffrey M. Karp, Seungpyo Hong, Omid C. Farokhzad, Rimona Margalit, and Robert Langer. Nanocarriers as an emerging platform for cancer therapy. *Nat Nano*, 2(4):751–760, 2007. doi: 10.1038/nnano.2007.387. URL `http://dx.doi.org/10.1038/nnano.2007.387`.

[40] Ivan H. El-Sayed, Xiaohua Huang, and Mostafa A. El-Sayed. Selective laser photo-thermal therapy of epithelial carcinoma using anti-egfr antibody conjugated gold nanoparticles. *Cancer Letters*, 239(1):129 – 135, 2006. ISSN 0304-3835. doi: http://dx.doi.org/10.1016/j.canlet.2005.07.035. URL `http://www.sciencedirect.com/science/article/pii/S0304383505007378`.

[41] Kulmeet K. Sandhu, Catherine M. McIntosh, Joseph M. Simard, Sallie W. Smith, and Vincent M. Rotello. Gold nanoparticle-mediated transfection of mammalian cells. *Bioconjugate Chemistry*, 13(1):3–6, 2002. doi: 10.1021/bc015545c. URL `http://dx.doi.org/10.1021/bc015545c`. PMID: 11792172.

[42] Prashant K. Jain, Ivan H. El-Sayed, and Mostafa A. El-Sayed. Au nanoparticles target cancer. *Nano Today*, 2(1):18 – 29, 2007. ISSN 1748-0132. doi: http://dx.doi.org/10.1016/S1748-0132(07)70016-6. URL `http://www.sciencedirect.com/science/article/pii/S1748013207700166`.

[43] Meena Mahmood, Dan Casciano, Yang Xu, and Alexandru S. Biris. Engineered nanostructural materials for application in cancer biology and medicine. *Journal of Applied Toxicology*, 32(1):10–19, 2012. ISSN 1099-1263. doi: 10.1002/jat.1718. URL `http://dx.doi.org/10.1002/jat.1718`.

[44] Fabio Sonvico, Stéphane Mornet, Sébastien Vasseur, Catherine Dubernet, Danielle Jaillard, Jeril Degrouard, Johan Hoebeke, Etienne Duguet, Paolo Colombo, and Patrick Couvreur. Folate-conjugated iron oxide nanoparticles for solid

tumor targeting as potential specific magnetic hyperthermia mediators: Synthesis, physicochemical characterization, and in vitro experiments. *Bioconjugate Chemistry*, 16(5):1181–1188, 2005. doi: 10.1021/bc050050z. URL `http://dx.doi.org/10.1021/bc050050z`. PMID: 16173796.

[45] Q A Pankhurst, J Connolly, S K Jones, and J Dobson. Applications of magnetic nanoparticles in biomedicine. *Journal of Physics D: Applied Physics*, 36(13):R167, 2003. URL `http://stacks.iop.org/0022-3727/36/i=13/a=201`.

[46] Tianmeng Sun, Yu Shrike Zhang, Bo Pang, Dong Choon Hyun, Miaoxin Yang, and Younan Xia. Engineered nanoparticles for drug delivery in cancer therapy. *Angewandte Chemie International Edition*, 53(46):12320–12364, 2014. ISSN 1521-3773. doi: 10.1002/anie.201403036. URL `http://dx.doi.org/10.1002/anie.201403036`.

[47] Vicki L Colvin. The potential environmental impact of engineered nanomaterials. *Nat Biotech*, 21:1166–1170, 2003. doi: 10.1038/nbt875. URL `http://dx.doi.org/10.1038/nbt875`.

[48] Andrew D. Maynard, Robert J. Aitken, Tilman Butz, Vicki Colvin, Ken Donaldson, Gunter Oberdorster, Martin A. Philbert, John Ryan, Anthony Seaton, Vicki Stone, Sally S. Tinkle, Lang Tran, Nigel J. Walker, and David B. Warheit. Safe handling of nanotechnology. *Nature*, 444:267–269, 2006. doi: 10.1038/444267a. URL `http://dx.doi.org/10.1038/444267a`.

[49] Michael N. Helmus. The need for rules and regulations. *Nat Nano*, 2:333–334, 2007. doi: 10.1038/nnano.2007.165. URL `http://dx.doi.org/10.1038/nnano.2007.165`.

[50] B. Devika Chithrani, Arezou A. Ghazani, and Warren C. W. Chan. Determining the size and shape dependence of gold nanoparticle uptake into mammalian cells. *Nano Letters*, 6(4):662–668, 2006. doi: 10.1021/nl052396o. URL `http://dx.doi.org/10.1021/nl052396o`. PMID: 16608261.

[51] Fumio Osaki, Takuya Kanamori, Shinsuke Sando, Takashi Sera, and Yasuhiro Aoyama. A quantum dot conjugated sugar ball and its cellular uptake. on the size effects of endocytosis in the subviral region. *Journal of the American Chemical Society*, 126(21):6520–6521, 2004. doi: 10.1021/ja048792a. URL `http://dx.doi.org/10.1021/ja048792a`. PMID: 15161257.

[52] Sonya Shortkroff, Mary Beth Turell, Karen Rice, and Thomas S. Thornhill. Cellular response to nanoparticles. In *Symposium W – Nanoparticulate Materials*, volume

704 of *MRS Proceedings*, 2001. doi: 10.1557/PROC-704-W11.5.1. URL `http://journals.cambridge.org/article_S1946427400609892`.

[53] Shikha Nangia and Radhakrishna Sureshkumar. Effects of nanoparticle charge and shape anisotropy on translocation through cell membranes. *Langmuir*, 28(51): 17666–17671, 2012. doi: 10.1021/la303449d. URL `http://dx.doi.org/10.1021/la303449d`. PMID: 23088323.

[54] Jie Yang and Jennifer Appleyard. The main phase transition of mica-supported phosphatidylcholine membranes. *The Journal of Physical Chemistry B*, 104(34): 8097–8100, 2000. doi: 10.1021/jp001403o. URL `http://dx.doi.org/10.1021/jp001403o`.

[55] Bo Wang, Liangfang Zhang, Sung Chul Bae, and Steve Granick. Nanoparticle-induced surface reconstruction of phospholipid membranes. *Proceedings of the National Academy of Sciences*, 105(47):18171–18175, 2008. doi: 10.1073/pnas.0807296105. URL `http://www.pnas.org/content/105/47/18171.abstract`.

[56] Ayush Verma, Oktay Uzun, Yuhua Hu, Ying Hu, Hee-Sun Han, Nicki Watson, Suelin Chen, Darrell J. Irvine, and Francesco Stellacci. Surface-structure-regulated cell-membrane penetration by monolayer-protected nanoparticles. *Nat Mater*, 7:588–595, 2008. doi: 10.1038/nmat2202. URL `http://dx.doi.org/10.1038/nmat2202`.

[57] Alicia M. Jackson, Jacob W. Myerson, and Francesco Stellacci. Spontaneous assembly of subnanometre-ordered domains in the ligand shell of monolayer-protected nanoparticles. *Nat Mater*, 3(5):330–336, 2004. doi: 10.1038/nmat1116. URL `http://dx.doi.org/10.1038/nmat1116`.

[58] Ayush Verma and Francesco Stellacci. Effect of surface properties on nanoparticle–cell interactions. *Small*, 6(1):12–21, 2010. ISSN 1613-6829. doi: 10.1002/smll.200901158. URL `http://dx.doi.org/10.1002/smll.200901158`.

[59] Paraskevi Gkeka, Lev Sarkisov, and Panagiotis Angelikopoulos. Homogeneous hydrophobic–hydrophilic surface patterns enhance permeation of nanoparticles through lipid membranes. *The Journal of Physical Chemistry Letters*, 4(11): 1907–1912, 2013. doi: 10.1021/jz400679z. URL `http://dx.doi.org/10.1021/jz400679z`.

[60] Rakwoo Chang and Angela Violi. Insights into the effect of combustion-generated carbon nanoparticles on biological membranes: a computer simulation study. *The Journal of Physical Chemistry B*, 110(10):5073–5083, 2006. doi: 10.1021/jp0565148. URL `http://dx.doi.org/10.1021/jp0565148`. PMID: 16526750.

[61] Randy P. Carney, Tamara M. Carney, Marie Mueller, and Francesco Stellacci. Dynamic cellular uptake of mixed-monolayer protected nanoparticles. *Biointerphases*, 7(1):17, 2012. doi: http://dx.doi.org/10.1007/s13758-011-0017-3. URL `http://scitation.aip.org/content/avs/journal/bip/7/1/10.1007/s13758-011-0017-3`.

[62] Reid C. Van Lehn, Maria Ricci, Paulo H.J. Silva, Patrizia Andreozzi, Javier Reguera, Kislon Voïtchovsky, Francesco Stellacci, and Alfredo Alexander-Katz. Lipid tail protrusions mediate the insertion of nanoparticles into model cell membranes. *Nat Commun*, 5, 2014. doi: 10.1038/ncomms5482. URL `http://dx.doi.org/10.1038/ncomms5482`.

[63] Pascale R. Leroueil, Seungpyo Hong, Almut Mecke, James R. Baker, Bradford G. Orr, and Mark M. Banaszak Holl. Nanoparticle interaction with biological membranes: Does nanotechnology present a janus face? *Accounts of Chemical Research*, 40(5):335–342, 2007. doi: 10.1021/ar600012y. URL `http://dx.doi.org/10.1021/ar600012y`. PMID: 17474708.

[64] Huajian Gao, Wendong Shi, and Lambert B. Freund. Mechanics of receptor-mediated endocytosis. *Proceedings of the National Academy of Sciences of the United States of America*, 102(27):9469–9474, 2005. doi: 10.1073/pnas.0503879102. URL `http://www.pnas.org/content/102/27/9469.abstract`.

[65] Sulin Zhang, Ju Li, George Lykotrafitis, Gang Bao, and Subra Suresh. Size-dependent endocytosis of nanoparticles. *Advanced Materials*, 21(4):419–424, 2009. ISSN 1521-4095. doi: 10.1002/adma.200801393. URL `http://dx.doi.org/10.1002/adma.200801393`.

[66] Kurt A. Smith, David Jasnow, and Anna C. Balazs. Designing synthetic vesicles that engulf nanoscopic particles. *The Journal of Chemical Physics*, 127(8):084703, 2007. doi: http://dx.doi.org/10.1063/1.2766953. URL `http://scitation.aip.org/content/aip/journal/jcp/127/8/10.1063/1.2766953`.

[67] Xing Chen, Andras Kis, A. Zettl, and Carolyn R. Bertozzi. A cell nanoinjector based on carbon nanotubes. *Proceedings of the National Academy of Sciences*, 104(20):8218–8222, 2007. doi: 10.1073/pnas.0700567104. URL `http://www.pnas.org/content/104/20/8218.abstract`.

[68] Ivan U. Vakarelski, Scott C. Brown, Ko Higashitani, and Brij M. Moudgil. Penetration of living cell membranes with fortified carbon nanotube tips. *Langmuir*, 23(22):10893–10896, 2007. doi: 10.1021/la701878n. URL `http://dx.doi.org/10.1021/la701878n`. PMID: 17894512.

[69] Seungpyo Hong, Pascale R. Leroueil, Elizabeth K. Janus, Jennifer L. Peters, Mary-Margaret Kober, Mohammad T. Islam, Bradford G. Orr, James R. Baker, and Mark M. Banaszak Holl. Interaction of polycationic polymers with supported lipid bilayers and cells: nanoscale hole formation and enhanced membrane permeability. *Bioconjugate Chemistry*, 17(3):728–734, 2006. doi: 10.1021/bc060077y. URL `http://dx.doi.org/10.1021/bc060077y`. PMID: 16704211.

[70] Ge Liu, DeShan Li, Murali K. Pasumarthy, Tomasz H. Kowalczyk, Christopher R. Gedeon, Susannah L. Hyatt, Jennifer M. Payne, Timothy J. Miller, Peter Brunovskis, Tamara L. Fink, Osman Muhammad, Robert C. Moen, Richard W. Hanson, and Mark J. Cooper. Nanoparticles of compacted dna transfect postmitotic cells. *Journal of Biological Chemistry*, 278(35):32578–32586, 2003. doi: 10.1074/jbc.M305776200. URL `http://www.jbc.org/content/278/35/32578.abstract`.

[71] JA Wolff, RW Malone, P Williams, W Chong, G Acsadi, A Jani, and PL Felgner. Direct gene transfer into mouse muscle in vivo. *Science*, 247(4949):1465–1468, 1990. doi: 10.1126/science.1690918. URL `http://www.sciencemag.org/content/247/4949/1465.abstract`.

[72] José A. Rojas-Chapana, Miguel A. Correa-Duarte, Zhifeng Ren, Krzysztof Kempa, and Michael Giersig. Enhanced introduction of gold nanoparticles into vital acidothiobacillus ferrooxidans by carbon nanotube-based microwave electroporation. *Nano Letters*, 4(5):985–988, 2004. doi: 10.1021/nl049699n. URL `http://dx.doi.org/10.1021/nl049699n`.

[73] Alexander G. Tkachenko, Huan Xie, Donna Coleman, Wilhelm Glomm, Joseph Ryan, Miles F. Anderson, Stefan Franzen, and Daniel L. Feldheim. Multifunctional gold nanoparticlepeptide complexes for nuclear targeting. *Journal of the American Chemical Society*, 125(16):4700–4701, 2003. doi: 10.1021/ja0296935. URL `http://dx.doi.org/10.1021/ja0296935`. PMID: 12696875.

[74] Wan-Seob Cho, Minjung Cho, Jinyoung Jeong, Mina Choi, Beom Seok Han, Hyung-Seon Shin, Jin Hong, Bong Hyun Chung, Jayoung Jeong, and Myung-Haing Cho. Size-dependent tissue kinetics of peg-coated gold nanoparticles. *Toxicology and Applied Pharmacology*, 245(1):116 – 123, 2010. ISSN 0041-008X. doi: http://dx.doi.org/10.1016/j.taap.2010.02.013. URL `http://www.sciencedirect.com/science/article/pii/S0041008X10000724`.

[75] Jessica P. Ryman-Rasmussen, Jim E. Riviere, and Nancy A. Monteiro-Riviere. Variables influencing interactions of untargeted quantum dot nanoparticles with skin cells and identification of biochemical modulators. *Nano Letters*, 7(5):1344–1348,

2007. doi: 10.1021/nl070375j. URL http://dx.doi.org/10.1021/nl070375j. PMID: 17408303.

[76] Gopakumar Gopalakrishnan, Christophe Danelon, Paulina Izewska, Michael Prummer, Pierre-Yves Bolinger, Isabelle Geissbühler, Davide Demurtas, Jacques Dubochet, and Horst Vogel. Multifunctional lipid/quantum dot hybrid nanocontainers for controlled targeting of live cells. *Angewandte Chemie International Edition*, 45(33):5478–5483, 2006. ISSN 1521-3773. doi: 10.1002/anie.200600545. URL http://dx.doi.org/10.1002/anie.200600545.

[77] Editorial. Colloidal particles at liquid interfaces. *Phys. Chem. Chem. Phys.*, 9: 6298–6299, 2007. doi: 10.1039/B716587K. URL http://dx.doi.org/10.1039/ B716587K.

[78] Wolfgang H. Binder, Robert Sachsenhofer, Dominique Farnik, and Dieter Blaas. Guiding the location of nanoparticles into vesicular structures: a morphological study. *Phys. Chem. Chem. Phys.*, 9:6435–6441, 2007. doi: 10.1039/B711470M. URL http://dx.doi.org/10.1039/B711470M.

[79] Yinfeng Li, Xuejin Li, Zhonghua Li, and Huajian Gao. Surface-structure-regulated penetration of nanoparticles across a cell membrane. *Nanoscale*, 4:3768–3775, 2012. doi: 10.1039/C2NR30379E. URL http://dx.doi.org/10.1039/C2NR30379E.

[80] Paraskevi Gkeka, Panagiotis Angelikopoulos, Lev Sarkisov, and Zoe Cournia. Membrane partitioning of anionic, ligand-coated nanoparticles is accompanied by ligand snorkeling, local disordering, and cholesterol depletion. *PLoS Comput Biol*, 10(12):e1003917, 12 2014. doi: 10.1371/journal.pcbi.1003917. URL http: //dx.doi.org/10.1371%2Fjournal.pcbi.1003917.

[81] Xiang Liu, Miao Yu, Hyewon Kim, Marta Mameli, and Francesco Stellacci. Determination of monolayer-protected gold nanoparticle ligand–shell morphology using nmr. *Nat Commun*, 31(4):1182, 2012. doi: 10.1038/ncomms2155. URL http://dx.doi.org/10.1038/ncomms2155.

[82] Paolo Pengo, Stefano Polizzi, Lucia Pasquato, and Paolo Scrimin. Carboxylateimidazole cooperativity in dipeptide-functionalized gold nanoparticles with esterase-like activity. *Journal of the American Chemical Society*, 127(6):1616–1617, 2005. doi: 10.1021/ja043547c. URL http://dx.doi.org/10.1021/ja043547c. PMID: 15700977.

[83] Marie-Christine Daniel and Didier Astruc. Gold nanoparticles: assembly, supramolecular chemistry, quantum-size-related properties, and applications toward biology, catalysis, and nanotechnology. *Chemical Reviews*, 104(1):293–346, 2004.

doi: 10.1021/cr030698+. URL `http://dx.doi.org/10.1021/cr030698+`. PMID: 14719978.

[84] Daniel Aili, Morgan Mager, David Roche, and Molly M. Stevens. Hybrid nanoparticleliposome detection of phospholipase activity. *Nano Letters*, 11(4):1401–1405, 2011. doi: 10.1021/nl1024062. URL `http://dx.doi.org/10.1021/nl1024062`. PMID: 20795711.

[85] Randy P. Carney, Yann Astier, Tamara M. Carney, Kislon Voïtchovsky, Paulo H. Jacob Silva, and Francesco Stellacci. Electrical method to quantify nanoparticle interaction with lipid bilayers. *ACS Nano*, 7(2):932–942, 2013. doi: 10.1021/nn3036304. URL `http://dx.doi.org/10.1021/nn3036304`. PMID: 23267695.

[86] Reid C. Van Lehn, Prabhani U. Atukorale, Randy P. Carney, Yu-Sang Yang, Francesco Stellacci, Darrell J. Irvine, and Alfredo Alexander-Katz. Effect of particle diameter and surface composition on the spontaneous fusion of monolayer-protected gold nanoparticles with lipid bilayers. *Nano Letters*, 13(9):4060–4067, 2013. doi: 10.1021/nl401365n. URL `http://dx.doi.org/10.1021/nl401365n`. PMID: 23915118.

[87] Ayush Verma and Francesco Stellacci. Effect of surface properties on nanoparticle–cell interactions. *Small*, 6(1):12–21, 2010. ISSN 1613-6829. doi: 10.1002/smll.200901158. URL `http://dx.doi.org/10.1002/smll.200901158`.

[88] Hong-ming Ding, Wen-de Tian, and Yu-qiang Ma. Designing nanoparticle translocation through membranes by computer simulations. *ACS Nano*, 6(2):1230–1238, 2012. doi: 10.1021/nn2038862. URL `http://dx.doi.org/10.1021/nn2038862`. PMID: 22208867.

[89] Sergey Pogodin, Marco Werner, Jens-Uwe Sommer, and Vladimir A. Baulin. Nanoparticle-induced permeability of lipid membranes. *ACS Nano*, 6(12):10555–10561, 2012. doi: 10.1021/nn3028858. URL `http://dx.doi.org/10.1021/nn3028858`. PMID: 23128273.

[90] Christina L. Ting and Zhen-Gang Wang. Minimum free energy paths for a nanoparticle crossing the lipid membrane. *Soft Matter*, 8:12066–12071, 2012. doi: 10.1039/C2SM26377G. URL `http://dx.doi.org/10.1039/C2SM26377G`.

[91] Jiaqi Lin, Hongwu Zhang, Zhen Chen, and Yonggang Zheng. Penetration of lipid membranes by gold nanoparticles: Insights into cellular uptake, cytotoxicity, and their relationship. *ACS Nano*, 4(9):5421–5429, 2010. doi: 10.1021/nn1010792. URL `http://dx.doi.org/10.1021/nn1010792`. PMID: 20799717.

[92] Reid C. Van Lehn and Alfredo Alexander-Katz. Penetration of lipid bilayers by nanoparticles with environmentally-responsive surfaces: simulations and theory. *Soft Matter*, 7:11392–11404, 2011. doi: 10.1039/C1SM06405C. URL `http://dx.doi.org/10.1039/C1SM06405C`.

[93] Ilja Czolkos, Aldo Jesorka, and Owe Orwar. Molecular phospholipid films on solid supports. *Soft Matter*, 7:4562–4576, 2011. doi: 10.1039/C0SM01212B. URL `http://dx.doi.org/10.1039/C0SM01212B`.

[94] E. Tanaka, M.; Sackmann. Polymer-supported membranes as models of the cell surface. *Nature*, 437:656–663, 2005.

[95] Edward T. Castellana and Paul S. Cremer. Solid supported lipid bilayers: From biophysical studies to sensor design. *Surface Science Reports*, 61(10):429 – 444, 2006. ISSN 0167-5729. doi: http://dx.doi.org/10.1016/j.surfrep.2006.06.001. URL `http://www.sciencedirect.com/science/article/pii/S0167572906000616`.

[96] Theobald Lohmüller, Sara Triffo, Geoff P. O'Donoghue, Qian Xu, Michael P. Coyle, and Jay T. Groves. Supported membranes embedded with fixed arrays of gold nanoparticles. *Nano Letters*, 11(11):4912–4918, 2011. doi: 10.1021/nl202847t. URL `http://dx.doi.org/10.1021/nl202847t`. PMID: 21967595.

[97] Armin Rumpel, Michael Novak, Johannes Walter, Björn Braunschweig, Marcus Halik, and Wolfgang Peukert. Tuning the molecular order of c60 functionalized phosphonic acid monolayers. *Langmuir*, 27(24):15016–15023, 2011. doi: 10.1021/la203916h. URL `http://dx.doi.org/10.1021/la203916h`. PMID: 22044068.

[98] Young Kwang Lee and Jwa-Min Nam. Electrofluidic lipid membrane biosensor. *Small*, 8(6):832–837, 2012. ISSN 1613-6829. doi: 10.1002/smll.201102093. URL `http://dx.doi.org/10.1002/smll.201102093`.

[99] Boryana N. Manz, Bryan L. Jackson, Rebecca S. Petit, Michael L. Dustin, and Jay Groves. T-cell triggering thresholds are modulated by the number of antigen within individual t-cell receptor clusters. *Proceedings of the National Academy of Sciences*, 108(22):9089–9094, 2011. doi: 10.1073/pnas.1018771108. URL `http://www.pnas.org/content/108/22/9089.abstract`.

[100] Niña C. Hartman, Jeffrey A. Nye, and Jay T. Groves. Cluster size regulates protein sorting in the immunological synapse. *Proceedings of the National Academy of Sciences*, 106(31):12729–12734, 2009. doi: 10.1073/pnas.0902621106. URL `http://www.pnas.org/content/106/31/12729.abstract`.

[101] S. Pautot, H. Lee, and J. T. Isacoff, E. Y.and Groves. Neuronal synapse interaction reconstituted between live cells and supported lipid bilayers. *Nature Chemical Biology*, 1(31):283–289, 2005. doi: http://www.nature.com/nchembio/journal/v1/n5/suppinfo/nchembio737˙S1.html.

[102] Khalid Salaita, Pradeep M. Nair, Rebecca S. Petit, Richard M. Neve, Debopriya Das, Joe W. Gray, and Jay T. Groves. Restriction of receptor movement alters cellular response: Physical force sensing by epha2. *Science*, 327(5971):1380–1385, 2010. doi: 10.1126/science.1181729. URL `http://www.sciencemag.org/content/327/5971/1380.abstract`.

[103] Ilya Reviakine and Alain Brisson. Streptavidin 2d crystals on supported phospholipid bilayers: toward constructing anchored phospholipid bilayers. *Langmuir*, 17(26):8293–8299, 2001. doi: 10.1021/la010626i. URL `http://dx.doi.org/10.1021/la010626i`.

[104] Charlotte Larsson, Michael Rodahl, and Fredrik Höök. Characterization of dna immobilization and subsequent hybridization on a 2d arrangement of streptavidin on a biotin-modified lipid bilayer supported on sio2. *Analytical Chemistry*, 75(19): 5080–5087, 2003. doi: 10.1021/ac034269n. URL `http://dx.doi.org/10.1021/ac034269n`. PMID: 14708781.

[105] Ilya Reviakine, Wilma Bergsma-Schutter, and Alain Brisson. Growth of protein 2-d crystals on supported planar lipid bilayers imagedin situby AFM. *Journal of Structural Biology*, 121(3):356 – 361, 1998. ISSN 1047-8477. doi: http://dx.doi.org/10.1006/jsbi.1998.4003. URL `http://www.sciencedirect.com/science/article/pii/S1047847798940035`.

[106] A A Brian and H M McConnell. Allogeneic stimulation of cytotoxic t cells by supported planar membranes. *Proceedings of the National Academy of Sciences*, 81 (19):6159–6163, 1984.

[107] Peter Lenz, Caroline M. Ajo-Franklin, and Steven G. Boxer. Patterned supported lipid bilayers and monolayers on poly(dimethylsiloxane). *Langmuir*, 20(25): 11092–11099, 2004. doi: 10.1021/la048450i. URL `http://dx.doi.org/10.1021/la048450i`. PMID: 15568862.

[108] Stefanie Goennenwein, Motomu Tanaka, Bin Hu, Luis Moroder, and Erich Sackmann. Functional incorporation of integrins into solid supported membranes on ultrathin films of cellulose: Impact on adhesion. *Biophysical Journal*, 85(1):646 – 655, 2003. ISSN 0006-3495. doi: http://dx.doi.org/10.1016/S0006-3495(03)74508-1. URL `http://www.sciencedirect.com/science/article/pii/S0006349503745081`.

[109] Michael L. Wagner and Lukas K. Tamm. Reconstituted syntaxin1a/snap25 interacts with negatively charged lipids as measured by lateral diffusion in planar supported bilayers. *Biophysical Journal*, 81(1):266 – 275, 2001. ISSN 0006-3495. doi: http://dx.doi.org/10.1016/S0006-3495(01)75697-4. URL `http://www.sciencedirect.com/science/article/pii/S0006349501756974`.

[110] Jeffrey C. Munro and Curtis W. Frank. In situ formation and characterization of poly(ethylene glycol)-supported lipid bilayers on gold surfaces. *Langmuir*, 20(24): 10567–10575, 2004. doi: 10.1021/la048378o. URL `http://dx.doi.org/10.1021/la048378o`. PMID: 15544386.

[111] Vitalii I. Silin, Herbert Wieder, John T. Woodward, Gintaras Valincius, A. Offenhausser, and Anne L. Plant. The role of surface free energy on the formation of hybrid bilayer membranes. *Journal of the American Chemical Society*, 124(49): 14676–14683, 2002. doi: 10.1021/ja026585+. URL `http://dx.doi.org/10.1021/ja026585+`. PMID: 12465979.

[112] Samuel Terrettaz, Michael Mayer, and Horst Vogel. Highly electrically insulating tethered lipid bilayers for probing the function of ion channel proteins. *Langmuir*, 19(14):5567–5569, 2003. doi: 10.1021/la034197v. URL `http://dx.doi.org/10.1021/la034197v`.

[113] Oliver Purrucker, Anton Förtig, Rainer Jordan, and Motomu Tanaka. Supported membranes with well-defined polymer tethers—incorporation of cell receptors. *ChemPhysChem*, 5(3):327–335, 2004. ISSN 1439-7641. doi: 10.1002/cphc.200300863. URL `http://dx.doi.org/10.1002/cphc.200300863`.

[114] Winfried Römer, Yuen H. Lam, Dahlia Fischer, Anthony Watts, Wolfgang B. Fischer, Petra Göring, Ralf B. Wehrspohn, Ulrich Gösele, and Claudia Steinem. Channel activity of a viral transmembrane peptide in micro-blms: vpu1-32 from hiv-1. *Journal of the American Chemical Society*, 126(49):16267–16274, 2004. doi: 10.1021/ja0451970. URL `http://dx.doi.org/10.1021/ja0451970`.

[115] Winfried Römer and Claudia Steinem. Impedance analysis and single-channel recordings on nano-black lipid membranes based on porous alumina. *Biophysical Journal*, 86(2):955 – 965, 2004. ISSN 0006-3495. doi: http://dx.doi.org/10.1016/S0006-3495(04)74171-5. URL `http://www.sciencedirect.com/science/article/pii/S0006349504741715`.

[116] Sofia Svedhem, Indriati Pfeiffer, Charlotte Larsson, Christer Wingren, Carl Borrebaeck, and Fredrik Höök. Patterns of dna-labeled and scfv-antibody-carrying lipid vesicles directed by material-specific immobilization of dna and

supported lipid bilayer formation on an au/sio2 template. *ChemBioChem*, 4 (4):339–343, 2003. ISSN 1439-7633. doi: 10.1002/cbic.200390055. URL `http://dx.doi.org/10.1002/cbic.200390055`.

[117] Chiaki Yoshina-Ishii and Steven G. Boxer. Arrays of mobile tethered vesicles on supported lipid bilayers. *Journal of the American Chemical Society*, 125(13): 3696–3697, 2003. doi: 10.1021/ja029783+. URL `http://dx.doi.org/10.1021/ja029783+`. PMID: 12656589.

[118] Marie-Paule Mingeot-Leclercq, Magali Deleu, Robert Brasseur, and Yves F Dufrene. Atomic force microscopy of supported lipid bilayers. *Nature Protocols*, 3(10):1654–1659, 2008. doi: http://dx.doi.org/10.1038/nprot.2008.149.

[119] Jay T. Groves, Nick Ulman, and Steven G. Boxer. Micropatterning fluid lipid bilayers on solid supports. *Science*, 275(5300):651–653, 1997. doi: 10.1126/science.275.5300.651. URL `http://www.sciencemag.org/content/275/5300/651.abstract`.

[120] Kevin C. Weng, Johan J.R. Stalgren, Subhash H. Risbud, and Curtis W. Frank. Planar bilayer lipid membranes supported on mesoporous aerogels, xerogels, and vycor® glass: an epifluorescence microscopy study. *Journal of Non-Crystalline Solids*, 350(0):46–53, 2004. ISSN 0022-3093. doi: http://dx.doi.org/10.1016/j.jnoncrysol.2004.06.053. URL `http://www.sciencedirect.com/science/article/pii/S0022309304008221`.

[121] L.K. Tamm and H.M. McConnell. Supported phospholipid bilayers. *Biophysical Journal*, 47(1):105 – 113, 1985. ISSN 0006-3495. doi: http://dx.doi.org/10.1016/S0006-3495(85)83882-0. URL `http://www.sciencedirect.com/science/article/pii/S0006349585838820`.

[122] T. Charitat, E. Bellet-Amalric, G. Fragneto, and F. Graner. Adsorbed and free lipid bilayers at the solid-liquid interface. *The European Physical Journal B - Condensed Matter and Complex Systems*, 8(4):583–593, 1999. ISSN 1434-6028. doi: 10.1007/s100510050725. URL `http://dx.doi.org/10.1007/s100510050725`.

[123] Edwin Kalb, Sammy Frey, and Lukas K. Tamm. Formation of supported planar bilayers by fusion of vesicles to supported phospholipid monolayers. *Biochimica et Biophysica Acta (BBA) - Biomembranes*, 1103(2):307 – 316, 1992. ISSN 0005-2736. doi: http://dx.doi.org/10.1016/0005-2736(92)90101-Q. URL `http://www.sciencedirect.com/science/article/pii/000527369290101Q`.

[124] Danielle Keller, Niels B. Larsen, Ian M. Møller, and Ole G. Mouritsen. Decoupled phase transitions and grain-boundary melting in supported phospholipid bilayers.

Phys. Rev. Lett., 94:025701, Jan 2005. doi: 10.1103/PhysRevLett.94.025701. URL `http://link.aps.org/doi/10.1103/PhysRevLett.94.025701`.

[125] A. Charrier and F. Thibaudau. Main phase transitions in supported lipid single-bilayer. *Biophysical Journal*, 89(2):1094 – 1101, 2005. ISSN 0006-3495. doi: http://dx.doi.org/10.1529/biophysj.105.062463. URL `http://www.sciencedirect.com/science/article/pii/S0006349505727570`.

[126] Z. Vivian Feng, Tighe A. Spurlin, and Andrew A. Gewirth. Direct visualization of asymmetric behavior in supported lipid bilayers at the gel-fluid phase transition. *Biophysical Journal*, 88(3):2154 – 2164, 2005. ISSN 0006-3495. doi: http://dx.doi.org/10.1529/biophysj.104.052456. URL `http://www.sciencedirect.com/science/article/pii/S000634950573277X`.

[127] S. Stanglmaier, S. Hertrich, K. Fritz, J.-F. Moulin, M. Haese-Seiller, J. O. Rädler, and B. Nickel. Asymmetric distribution of anionic phospholipids in supported lipid bilayers. *Langmuir*, 28(29):10818–10821, 2012. doi: 10.1021/la3019887. URL `http://dx.doi.org/10.1021/la3019887`. PMID: 22789026.

[128] Andrew P. Shreve, Michael C. Howland, Annapoorna R. Sapuri-Butti, Toby W. Allen, and Atul N. Parikh. Evidence for leaflet-dependent redistribution of charged molecules in fluid supported phospholipid bilayers. *Langmuir*, 24(23):13250–13253, 2008. doi: 10.1021/la802909c. URL `http://dx.doi.org/10.1021/la802909c`. PMID: 19007257.

[129] Fernanda F. Rossetti, Marcus Textor, and Ilya Reviakine. Asymmetric distribution of phosphatidyl serine in supported phospholipid bilayers on titanium dioxide. *Langmuir*, 22(8):3467–3473, 2006. doi: 10.1021/la053000r. URL `http://dx.doi.org/10.1021/la053000r`. PMID: 16584212.

[130] Gregory A. Voth. Coarse-graining of condensed phase and biomolecular systems. *CRC press*, 2008.

[131] Herman J. C. Berendsen. Simulating the physical world: Hierarchical modeling from quantum mechanics to fluid dynamics. *Cambridge University Pres*, 2007.

[132] B. Dunweg and A. J. C. Ladd. Advanced computer simulation approaches for soft matter sciences iii. *Springer-Verlag Berlin Heidelberg*, 2009.

[133] P. J. Hoogerbrugge and J. M. V. A. Koelman. Simulating microscopic hydrodynamic phenomena with dissipative particle dynamics. *EPL (Europhysics Letters)*, 19(3): 155, 1992. URL `http://stacks.iop.org/0295-5075/19/i=3/a=001`.

[134] Robert D. Groot and Patrick B. Warren. Dissipative particle dynamics: Bridging the gap between atomistic and mesoscopic simulation. *The Journal of Chemical Physics*, 107(11), 1997.

[135] William L. Jorgensen, David S. Maxwell, and Julian Tirado-Rives. Development and testing of the opls all-atom force field on conformational energetics and properties of organic liquids. *Journal of the American Chemical Society*, 118(45):11225–11236, 1996. doi: 10.1021/ja9621760. URL http://dx.doi.org/10.1021/ja9621760.

[136] George A. Kaminski, Richard A. Friesner, Julian Tirado-Rives, and William L. Jorgensen. Evaluation and reparametrization of the opls-aa force field for proteins via comparison with accurate quantum chemical calculations on peptides. *The Journal of Physical Chemistry B*, 105(28):6474–6487, 2001. doi: 10.1021/jp003919d. URL http://dx.doi.org/10.1021/jp003919d.

[137] Yong Duan, Chun Wu, Shibasish Chowdhury, Mathew C. Lee, Guoming Xiong, Wei Zhang, Rong Yang, Piotr Cieplak, Ray Luo, Taisung Lee, James Caldwell, Junmei Wang, and Peter Kollman. A point-charge force field for molecular mechanics simulations of proteins based on condensed-phase quantum mechanical calculations. *Journal of Computational Chemistry*, 24(16):1999–2012, 2003. ISSN 1096-987X. doi: 10.1002/jcc.10349. URL http://dx.doi.org/10.1002/jcc.10349.

[138] B. R. Brooks, C. L. Brooks, A. D. Mackerell, L. Nilsson, R. J. Petrella, B. Roux, Y. Won, G. Archontis, C. Bartels, S. Boresch, A. Caflisch, L. Caves, Q. Cui, A. R. Dinner, M. Feig, S. Fischer, J. Gao, M. Hodoscek, W. Im, K. Kuczera, T. Lazaridis, J. Ma, V. Ovchinnikov, E. Paci, R. W. Pastor, C. B. Post, J. Z. Pu, M. Schaefer, B. Tidor, R. M. Venable, H. L. Woodcock, X. Wu, W. Yang, D. M. York, and M. Karplus. Charmm: The biomolecular simulation program. *Journal of Computational Chemistry*, 30(10):1545–1614, 2009. ISSN 1096-987X. doi: 10.1002/jcc.21287. URL http://dx.doi.org/10.1002/jcc.21287.

[139] Bernard R. Brooks, Robert E. Bruccoleri, Barry D. Olafson, David J. States, S. Swaminathan, and Martin Karplus. Charmm: A program for macromolecular energy, minimization, and dynamics calculations. *Journal of Computational Chemistry*, 4(2):187–217, 1983. ISSN 1096-987X. doi: 10.1002/jcc.540040211. URL http://dx.doi.org/10.1002/jcc.540040211.

[140] Chris Oostenbrink, Alessandra Villa, Alan E. Mark, and Wilfred F. Van Gunsteren. A biomolecular force field based on the free enthalpy of hydration and solvation: The gromos force-field parameter sets 53a5 and 53a6. *Journal of Computational Chemistry*, 25(13):1656–1676, 2004. ISSN 1096-987X. doi: 10.1002/jcc.20090. URL http://dx.doi.org/10.1002/jcc.20090.

[141] R.W Hockney, S.P Goel, and J.W Eastwood. Quiet high-resolution computer models of a plasma. *Journal of Computational Physics*, 14(2):148 – 158, 1974. ISSN 0021-9991. doi: http://dx.doi.org/10.1016/0021-9991(74)90010-2. URL `http://www.sciencedirect.com/science/article/pii/0021999174900102`.

[142] Berk Hess, Henk Bekker, Herman J. C. Berendsen, and Johannes G. E. M. Fraaije. Lincs: A linear constraint solver for molecular simulations. *Journal of Computational Chemistry*, 18(12):1463–1472, 1997. ISSN 1096-987X. doi: 10.1002/(SICI)1096-987X(199709)18:12¡1463::AID-JCC4¿3.0.CO;2-H. URL `http://dx.doi.org/10.1002/(SICI)1096-987X(199709)18:12<1463::AID-JCC4>3.0.CO;2-H`.

[143] Jean-Paul Ryckaert, Giovanni Ciccotti, and Herman J.C Berendsen. Numerical integration of the cartesian equations of motion of a system with constraints: molecular dynamics of n-alkanes. *Journal of Computational Physics*, 23(3):327 – 341, 1977. ISSN 0021-9991. doi: http://dx.doi.org/10.1016/0021-9991(77)90098-5. URL `http://www.sciencedirect.com/science/article/pii/0021999177900985`.

[144] David van der Spoel and Paul J. van Maaren. The origin of layer structure artifacts in simulations of liquid water. *Journal of Chemical Theory and Computation*, 2(1):1–11, 2006. doi: 10.1021/ct0502256. URL `http://dx.doi.org/10.1021/ct0502256`.

[145] tagkey2002563. In Daan Frenkel and Berend Smit, editors, *Understanding Molecular Simulation (Second Edition)*, pages 563 – 571. Academic Press, San Diego, second edition edition, 2002. ISBN 978-0-12-267351-1. doi: http://dx.doi.org/10.1016/B978-012267351-1/50027-4. URL `http://www.sciencedirect.com/science/article/pii/B9780122673511500274`.

[146] M. Patra, M. Karttunen, M.T. Hyvönen, E. Falck, P. Lindqvist, and I. Vattulainen. Molecular dynamics simulations of lipid bilayers: Major artifacts due to truncating electrostatic interactions. *Biophysical Journal*, 84(6):3636 – 3645, 2003. ISSN 0006-3495. doi: http://dx.doi.org/10.1016/S0006-3495(03)75094-2. URL `http://www.sciencedirect.com/science/article/pii/S0006349503750942`.

[147] David Van Der Spoel, Erik Lindahl, Berk Hess, Gerrit Groenhof, Alan E. Mark, and Herman J. C. Berendsen. Gromacs: Fast, flexible, and free. *Journal of Computational Chemistry*, 26(16):1701–1718, 2005. ISSN 1096-987X. doi: 10.1002/jcc.20291. URL `http://dx.doi.org/10.1002/jcc.20291`.

[148] Berk Hess, Carsten Kutzner, David van der Spoel, and Erik Lindahl. Gromacs 4: algorithms for highly efficient, load-balanced, and scalable molecular simulation. *Journal of Chemical Theory and Computation*, 4(3):435–447, 2008. doi: 10.1021/ct700301q. URL `http://dx.doi.org/10.1021/ct700301q`.

[149] H.J.C. Berendsen, D. van der Spoel, and R. van Drunen. Gromacs: A message-passing parallel molecular dynamics implementation. *Computer Physics Communications*, 91(1–3):43 – 56, 1995. ISSN 0010-4655. doi: http://dx.doi.org/10.1016/0010-4655(95)00042-E. URL `http://www.sciencedirect.com/science/article/pii/001046559500042E`.

[150] M.K. Gilson, J.A. Given, B.L. Bush, and J.A. McCammon. The statistical-thermodynamic basis for computation of binding affinities: a critical review. *Biophysical Journal*, 72(3):1047–1069, 1997. doi: doi: 10.1016/S0006-3495(97)78756-3. URL `http://dx.doi.org/10.1016/S0006-3495(97)78756-3`.

[151] John G. Kirkwood. Statistical mechanics of fluid mixtures. *The Journal of Chemical Physics*, 3(5), 1935.

[152] Robert W. Zwanzig. Hightemperature equation of state by a perturbation method. i. nonpolar gases. *The Journal of Chemical Physics*, 22(8), 1954.

[153] G.N. Patey and J.P. Valleau. The free energy of spheres with dipoles: Monte carlo with multistage sampling. *Chemical Physics Letters*, 21(2):297 – 300, 1973. ISSN 0009-2614. doi: http://dx.doi.org/10.1016/0009-2614(73)80139-3. URL `http://www.sciencedirect.com/science/article/pii/0009261473801393`.

[154] Glenn M. Torrie and John P. Valleau. Monte carlo free energy estimates using non-boltzmann sampling: Application to the sub-critical lennard-jones fluid. *Chemical Physics Letters*, 28:578 – 581, 1974. ISSN 0009-2614. doi: http://dx.doi.org/10.1016/0009-2614(74)80109-0. URL `http://www.sciencedirect.com/science/article/pii/0009261474801090`.

[155] G.M. Torrie and J.P. Valleau. Nonphysical sampling distributions in monte carlo free-energy estimation: Umbrella sampling. *Journal of Computational Physics*, 23(2):187 – 199, 1977. ISSN 0021-9991. doi: http://dx.doi.org/10.1016/0021-9991(77)90121-8. URL `http://www.sciencedirect.com/science/article/pii/0021999177901218`.

[156] John C Shelley and Mee Y Shelley. Computer simulation of surfactant solutions. *Current Opinion in Colloid and Interface Science*, 5(12):101 – 110, 2000. ISSN 1359-0294. doi: http://dx.doi.org/10.1016/S1359-0294(00)00042-X. URL `http://www.sciencedirect.com/science/article/pii/S135902940000042X`.

[157] M. Mller, K. Katsov, and M. Schick. Coarse-grained models and collective phenomena in membranes: Computer simulation of membrane fusion. *Journal of Polymer Science Part B: Polymer Physics*, 41(13):1441–1450, 2003. ISSN 1099-0488. doi: 10.1002/polb.10456. URL `http://dx.doi.org/10.1002/polb.10456`.

[158] Siewert J. Marrink and D. Peter Tieleman. Perspective on the martini model. *Chem. Soc. Rev.*, 42:6801–6822, 2013. doi: 10.1039/C3CS60093A. URL `http://dx.doi.org/10.1039/C3CS60093A`.

[159] Siewert J. Marrink, H. Jelger Risselada, Serge Yefimov, D. Peter Tieleman, and Alex H. de Vries. The martini force field: coarse grained model for biomolecular simulations. *The Journal of Physical Chemistry B*, 111(27):7812–7824, 2007. doi: 10.1021/jp071097f. URL `http://dx.doi.org/10.1021/jp071097f`. PMID: 17569554.

[160] Siewert J. Marrink, Alex H. de Vries, and Alan E. Mark. Coarse grained model for semiquantitative lipid simulations. *The Journal of Physical Chemistry B*, 108 (2):750–760, 2004. doi: 10.1021/jp036508g. URL `http://dx.doi.org/10.1021/jp036508g`.

[161] Alexander E. Gorbalenya and Eugene V. Koonin. Helicases: amino acid sequence comparisons and structure-function relationships. *Current Opinion in Structural Biology*, 3(3):419 – 429, 1993. ISSN 0959-440X. doi: http://dx.doi.org/10.1016/S0959-440X(05)80116-2. URL `http://www.sciencedirect.com/science/article/pii/S0959440X05801162`.

[162] Narendra Tuteja and Renu Tuteja. Unraveling dna helicases. *European Journal of Biochemistry*, 271(10):1849–1863, 2004. ISSN 1432-1033. doi: 10.1111/j.1432-1033.2004.04094.x. URL `http://dx.doi.org/10.1111/j.1432-1033.2004.04094.x`.

[163] Christopher J. Fischer, Nasib K. Maluf, and Timothy M. Lohman. Mechanism of atp-dependent translocation of e.coli uvrd monomers along single-stranded dna. *Journal of Molecular Biology*, 344(5):1287 – 1309, 2004. ISSN 0022-2836. doi: http://dx.doi.org/10.1016/j.jmb.2004.10.005. URL `http://www.sciencedirect.com/science/article/pii/S0022283604012860`.

[164] Eric J. Tomko, Christopher J. Fischer, Anita Niedziela-Majka, and Timothy M. Lohman. A nonuniform stepping mechanism for e. coli uvrd monomer translocation along single-stranded dna. *Molecular Cell*, 26(3):335 – 347, 2007. ISSN 1097-2765. doi: http://dx.doi.org/10.1016/j.molcel.2007.03.024. URL `http://www.sciencedirect.com/science/article/pii/S1097276507002158`.

[165] Katherine M. Brendza, Wei Cheng, Christopher J. Fischer, Marla A. Chesnik, Anita Niedziela-Majka, and Timothy M. Lohman. Autoinhibition of escherichia coli rep monomer helicase activity by its 2b subdomain. *Proceedings of the National Academy of Sciences of the United States of America*, 102(29):10076–10081, 2005.

doi: 10.1073/pnas.0502886102. URL `http://www.pnas.org/content/102/29/10076.abstract`.

[166] Panos Soultanas, Mark S Dillingham, Sameer S Velankar, and Dale B Wigley. Dna binding mediates conformational changes and metal ion coordination in the active site of pcra helicase1. *Journal of Molecular Biology*, 290(1):137 – 148, 1999. ISSN 0022-2836. doi: http://dx.doi.org/10.1006/jmbi.1999.2873. URL `http://www.sciencedirect.com/science/article/pii/S0022283699928735`.

[167] Janid A. Ali and Timothy M. Lohman. Kinetic measurement of the step size of dna unwinding by escherichia coli uvrd helicase. *Science*, 275(5298):377–380, 1997. doi: 10.1126/science.275.5298.377. URL `http://www.sciencemag.org/content/275/5298/377.abstract`.

[168] Samuel G. Mackintosh and Kevin D. Raney. Dna unwinding and protein displacement by superfamily 1 and superfamily 2 helicases. *Nucleic Acids Research*, 34(15): 4154–4159, 2006. doi: 10.1093/nar/gkl501. URL `http://nar.oxfordjournals.org/content/34/15/4154.abstract`.

[169] Anita Niedziela-Majka, Marla A. Chesnik, Eric J. Tomko, and Timothy M. Lohman. Bacillus stearothermophilus pcra monomer is a single-stranded dna translocase but not a processive helicase in vitro. *Journal of Biological Chemistry*, 282(37): 27076–27085, 2007. doi: 10.1074/jbc.M704399200. URL `http://www.jbc.org/content/282/37/27076.abstract`.

[170] M. D. Betterton and Frank Jülicher. Opening of nucleic-acid double strands by helicases: Active versus passive opening. *Phys. Rev. E*, 71:011904, Jan 2005. doi: 10.1103/PhysRevE.71.011904. URL `http://link.aps.org/doi/10.1103/PhysRevE.71.011904`.

[171] Katherine Cox, Tim Watson, Panos Soultanas, and Jonathan D. Hirst. Molecular dynamics simulations of a helicase. *Proteins: Structure, Function, and Bioinformatics*, 52(2):254–262, 2003. ISSN 1097-0134. doi: 10.1002/prot.10400. URL `http://dx.doi.org/10.1002/prot.10400`.

[172] Alexander D MacKerell Jr. and Lennart Nilsson. Molecular dynamics simulations of nucleic acid–protein complexes. *Current Opinion in Structural Biology*, 18(2):194 – 199, 2008. ISSN 0959-440X. doi: http://dx.doi.org/10.1016/j.sbi.2007.12.012. URL `http://www.sciencedirect.com/science/article/pii/S0959440X0800002X`. Theory and simulation / Macromolecular assemblages.

[173] L. E. Bird, J. A. Brannigan, H. S. Subramanya, and D. B. Wigley. Characterisation of bacillus stearothermophilus pcra helicase: Evidence against an active rolling mechanism. *Nucleic Acids Research*, 26(11):2686–2693, 1998. doi: 10.1093/nar/26.11.2686. URL `http://nar.oxfordjournals.org/content/26/11/2686.abstract`.

[174] Helen M. Berman, John Westbrook, Zukang Feng, Gary Gilliland, T. N. Bhat, Helge Weissig, Ilya N. Shindyalov, and Philip E. Bourne. The protein data bank. *Nucleic Acids Research*, 28(1):235–242, 2000. doi: 10.1093/nar/28.1.235. URL `http://nar.oxfordjournals.org/content/28/1/235.abstract`.

[175] Sua Myong, Ivan Rasnik, Chirlmin Joo, Timothy M. Lohman, and Taekjip Ha. Repetitive shuttling of a motor protein on dna. *Nature*, 437(7063):1321–1325, 10 2005. URL `http://dx.doi.org/10.1038/nature04049`.

[176] Sergey Korolev, John Hsieh, George H. Gauss, Timothy M. Lohman, and Gabriel Waksman. Major domain swiveling revealed by the crystal structures of complexes of e. coli rep helicase bound to single-stranded dna and adp. *Cell*, 90(4):635–647, 8 1997. doi: http://dx.doi.org/10.1016/S0092-8674(00)80525-5. URL `http://www.sciencedirect.com/science/article/pii/S0092867400805255`.

[177] Ivan Rasnik, Sua Myong, Wei Cheng, Timothy M. Lohman, and Taekjip Ha. Dna-binding orientation and domain conformation of the e.coli rep helicase monomer bound to a partial duplex junction: Single-molecule studies of fluorescently labeled enzymes. *Journal of Molecular Biology*, 336(2):395 – 408, 2004. ISSN 0022-2836. doi: http://dx.doi.org/10.1016/j.jmb.2003.12.031. URL `http://www.sciencedirect.com/science/article/pii/S0022283603015353`.

[178] Kahled Toukan and Aneesur Rahman. Molecular-dynamics study of atomic motions in water. *Phys. Rev. B*, 31:2643–2648, 1985. doi: 10.1103/PhysRevB.31.2643. URL `http://link.aps.org/doi/10.1103/PhysRevB.31.2643`.

[179] P. Debye. Näherungsformeln für die zylinderfunktionen für große werte des arguments und unbeschränkt veränderliche werte des index. *Mathematische Annalen*, 67(4):535–558, 1909. ISSN 0025-5831. doi: 10.1007/BF01450097. URL `http://dx.doi.org/10.1007/BF01450097`.

[180] Giovanni Bussi, Davide Donadio, and Michele Parrinello. Canonical sampling through velocity rescaling. *The Journal of Chemical Physics*, 126(1):014101, 2007. doi: http://dx.doi.org/10.1063/1.2408420. URL `http://scitation.aip.org/content/aip/journal/jcp/126/1/10.1063/1.2408420`.

[181] H. J. C. Berendsen, J. P. M. Postma, W. F. van Gunsteren, A. DiNola, and J. R. Haak. Molecular dynamics with coupling to an external bath. *The Journal of Chemical Physics*, 81(8):3684–3690, 1984. URL http://scitation.aip.org/content/aip/journal/jcp/81/8/10.1063/1.448118.

[182] Prapasiri Pongprayoon, Oliver Beckstein, Chze Ling Wee, and Mark S. P. Sansom. Simulations of anion transport through oprp reveal the molecular basis for high affinity and selectivity for phosphate. *Proceedings of the National Academy of Sciences*, 106(51):21614–21618, 2009. doi: 10.1073/pnas.0907315106. URL http://www.pnas.org/content/106/51/21614.abstract.

[183] Camilo Aponte-Santamaria, Jochen S. Hub, and Bert L. de Groot. Dynamics and energetics of solute permeation through the plasmodium falciparum aquaglyceroporin. *Phys. Chem. Chem. Phys.*, 12:10246–10254, 2010. doi: 10.1039/C004384M. URL http://dx.doi.org/10.1039/C004384M.

[184] John D. Chodera, William C. Swope, Jed W. Pitera, Chaok Seok, and Ken A. Dill. Use of the weighted histogram analysis method for the analysis of simulated and parallel tempering simulations. *Journal of Chemical Theory and Computation*, 3(1):26–41, 2007. doi: 10.1021/ct0502864. URL http://dx.doi.org/10.1021/ct0502864.

[185] Jochen S. Hub, Bert L. de Groot, and David van der Spoel. g_wham—a free weighted histogram analysis implementation including robust error and autocorrelation estimates. *Journal of Chemical Theory and Computation*, 6(12):3713–3720, 2010. doi: 10.1021/ct100494z. URL http://dx.doi.org/10.1021/ct100494z.

[186] Justin A. Lemkul and David R. Bevan. Assessing the stability of alzheimer's amyloid protofibrils using molecular dynamics. *The Journal of Physical Chemistry B*, 114(4):1652–1660, 2010. doi: 10.1021/jp9110794. URL http://dx.doi.org/10.1021/jp9110794. PMID: 20055378.

[187] Arup K. Pathak and Tusar Bandyopadhyay. Unbinding free energy of acetyl-cholinesterase bound oxime drugs along the gorge pathway from metadynamics-umbrella sampling investigation. *Proteins: Structure, Function, and Bioinformatics*, 82(9):1799–1818, 2014. ISSN 1097-0134. doi: 10.1002/prot.24533. URL http://dx.doi.org/10.1002/prot.24533.

[188] Vivek Sinha, Bishwajit Ganguly, and Tusar Bandyopadhyay. Energetics of ortho-7 (oxime drug) translocation through the active-site gorge of tabun conjugated acetyl-cholinesterase. *PLoS ONE*, 7(7):e40188, 07 2012. doi: 10.1371/journal.pone.0040188. URL http://dx.doi.org/10.1371%2Fjournal.pone.0040188.

[189] Alexis De Angeli, Oscar Moran, Stefanie Wege, Sophie Filleur, Geneviève Ephritikhine, Sébastien Thomine, Hélène Barbier-Brygoo, and Franco Gambale. Atp binding to the c terminus of the arabidopsis thaliana nitrate/proton antiporter, at-clca, regulates nitrate transport into plant vacuoles. *Journal of Biological Chemistry*, 284(39):26526–26532, 2009. doi: 10.1074/jbc.M109.005132.

[190] Julia Contreras-García, Erin R. Johnson, Shahar Keinan, Robin Chaudret, Jean-Philip Piquemal, David N. Beratan, and Weitao Yang. Nciplot: A program for plotting noncovalent interaction regions. *Journal of Chemical Theory and Computation*, 7(3):625–632, 2011. doi: 10.1021/ct100641a. URL `http://dx.doi.org/10.1021/ct100641a`. PMID: 21516178.

[191] Tom Darden, Darrin York, and Lee Pedersen. Particle mesh ewald: An nlog(n) method for ewald sums in large systems. *The Journal of Chemical Physics*, 98(12): 10089–10092, 1993. URL `http://scitation.aip.org/content/aip/journal/jcp/98/12/10.1063/1.464397`.

[192] Yu Pan, Sabine Neuss, Annika Leifert, Monika Fischler, Fei Wen, Ulrich Simon, Günter Schmid, Wolfgang Brandau, and Willi Jahnen-Dechent. Size-dependent cytotoxicity of gold nanoparticles. *Small*, 3(11):1941–1949, 2007. ISSN 1613-6829. doi: 10.1002/smll.200700378. URL `http://dx.doi.org/10.1002/smll.200700378`.

[193] K Donaldson, V Stone, A Clouter, L Renwick, and W MacNee. Ultrafine particles. *Occupational and Environmental Medicine*, 58:211–216, 2001. ISSN 1613-6829. doi: 10.1136/oem.58.3.211. URL `http://www.ncbi.nlm.nih.gov/pmc/articles/PMC1740105/`.

[194] Leshuai W. Zhang, Jianzhong Yang, Andrew R. Barron, and Nancy A. Monteiro-Riviere. Endocytic mechanisms and toxicity of a functionalized fullerene in human cells. *Toxicology Letters*, 191(2–3):149 – 157, 2009. ISSN 0378-4274. doi: http://dx.doi.org/10.1016/j.toxlet.2009.08.017. URL `http://www.sciencedirect.com/science/article/pii/S0378427409014039`.

[195] Valeriy V. Ginzburg and Sudhakar Balijepalli. Modeling the thermodynamics of the interaction of nanoparticles with cell membranes. *Nano Letters*, 7(12):3716–3722, 2007. doi: 10.1021/nl072053l. URL `http://dx.doi.org/10.1021/nl072053l`. PMID: 17983249.

[196] Yang Li and Ning Gu. Thermodynamics of charged nanoparticle adsorption on charge-neutral membranes: A simulation study. *The Journal of Physical Chemistry B*, 114(8):2749–2754, 2010. doi: 10.1021/jp904550b. URL `http://dx.doi.org/10.1021/jp904550b`. PMID: 20146444.

[197] Kai Yang and Yu-Qiang Ma. Computer simulation of the translocation of nanoparticles with different shapes across a lipid bilayer. *Nat Nano*, 5(8):579–583, 2010. doi: 10.1038/nnano.2010.141. URL `http://www.nature.com/nnano/journal/v5/n8/abs/nnano.2010.141.html#supplementary-information`.

[198] Yusong Tu, Min Lv, Peng Xiu, Tien Huynh, Meng Zhang, Matteo Castelli, Zengrong Liu, Qing Huang, Chunhai Fan, Haiping Fang, and Ruhong Zhou. Destructive extraction of phospholipids from escherichia coli membranes by graphene nanosheets. *Nat Nano*, 8(8):594–601, 2013. doi: 10.1038/nnano.2013.125. URL `http://dx.doi.org/10.1038/nnano.2013.125`.

[199] Jirasak Wong-Ekkabut, Svetlana Baoukina, Wannapong Triampo, I-Ming Tang, D. Peter Tieleman, and Luca Monticelli. Computer simulation study of fullerene translocation through lipid membranes. *Nat Nano*, 3(6):363–368, 2008. doi: 10.1038/nnano.2008.130. URL `http://dx.doi.org/10.1038/nnano.2008.130`.

[200] Michael R. Rasch, Emma Rossinyol, Jose L. Hueso, Brian W. Goodfellow, Jordi Arbiol, and Brian A. Korgel. Hydrophobic gold nanoparticle self-assembly with phosphatidylcholine lipid: Membrane-loaded and janus vesicles. *Nano Letters*, 10 (9):3733–3739, 2010. doi: 10.1021/nl102387n. URL `http://dx.doi.org/10.1021/nl102387n`. PMID: 20731366.

[201] Geoffrey D Bothun. Hydrophobic silver nanoparticles trapped in lipid bilayers: Size distribution, bilayer phase behavior, and optical properties. *Journal of Nanobiotechnology*, 6, 2008. doi: doi:10.1186/1477-3155-6-13. URL `http://www.jnanobiotechnology.com/content/6/1/13`.

[202] Sung-Hee Park, Seong-Geun Oh, Ji-Young Mun, and Sung-Sik Han. Effects of silver nanoparticles on the fluidity of bilayer in phospholipid liposome. *Colloids and Surfaces B: Biointerfaces*, 44(2–3):117 – 122, 2005. ISSN 0927-7765. doi: http://dx.doi.org/10.1016/j.colsurfb.2005.06.002. URL `http://www.sciencedirect.com/science/article/pii/S0927776505001700`.

[203] Getahun Merga, Nuvia Saucedo, Laura C. Cass, James Puthussery, and Dan Meisel. "naked" gold nanoparticles: Synthesis, characterization, catalytic hydrogen evolution, and sers. *The Journal of Physical Chemistry C*, 114(35):14811–14818, 2010. doi: 10.1021/jp104922a. URL `http://dx.doi.org/10.1021/jp104922a`.

[204] David Zopes, Silke Kremer, Harald Scherer, Lhoussaine Belkoura, Ingo Pantenburg, Wieland Tyrra, and Sanjay Mathur. Hydrolytic decomposition of tetramethylammonium bis(trifluoromethyl)aurate(i), [nme4][au(cf3)2]: A route for the synthesis

of gold nanoparticles in aqueous medium. *European Journal of Inorganic Chemistry*, 2011(2):273–280, 2011. ISSN 1099-0682. doi: 10.1002/ejic.201000863. URL http://dx.doi.org/10.1002/ejic.201000863.

[205] Laura Caprile, Albano Cossaro, Ermelinda Falletta, Cristina Della Pina, Ornella Cavalleri, Ranieri Rolandi, Silvana Terreni, Riccardo Ferrando, Michele Rossi, Luca Floreano, and Maurizio Canepa. Interaction of l-cysteine with naked gold nanoparticles supported on hopg: a high resolution xps investigation. *Nanoscale*, 4: 7727–7734, 2012. doi: 10.1039/C2NR32741D. URL http://dx.doi.org/10.1039/C2NR32741D.

[206] David Poger and Alan E. Mark. On the validation of molecular dynamics simulations of saturated and cis-monounsaturated phosphatidylcholine lipid bilayers: A comparison with experiment. *Journal of Chemical Theory and Computation*, 6(1):325–336, 2010. doi: 10.1021/ct900487a. URL http://dx.doi.org/10.1021/ct900487a.

[207] Kai Simons and Derek Toomre. Lipid rafts and signal transduction. *Nat Rev Mol Cell Biol*, 1(1):31–39, 2000. URL http://dx.doi.org/10.1038/35036052.

[208] Elina Ikonen. Roles of lipid rafts in membrane transport. *Current Opinion in Cell Biology*, 13(4):470 – 477, 2001. ISSN 0955-0674. doi: http://dx.doi.org/10.1016/S0955-0674(00)00238-6. URL http://www.sciencedirect.com/science/article/pii/S0955067400002386.

[209] Jürgen Benting, Anton Rietveld, Iris Ansorge, and Kai Simons. Acyl and alkyl chain length of gpi-anchors is critical for raft association in vitro. {*FEBS*} *Letters*, 462 (1–2):47 – 50, 1999. ISSN 0014-5793. doi: http://dx.doi.org/10.1016/S0014-5793(99)01501-X. URL http://www.sciencedirect.com/science/article/pii/S001457939901501X.

[210] Einar K. Fridriksson, Petia A. Shipkova, Erin D. Sheets, David Holowka, Barbara Baird, and Fred W. McLafferty. Quantitative analysis of phospholipids in functionally important membrane domains from rbl-2h3 mast cells using tandem high-resolution mass spectrometry. *Biochemistry*, 38(25):8056–8063, 1999. doi: 10.1021/bi9828324. URL http://dx.doi.org/10.1021/bi9828324. PMID: 10387050.

[211] David Van Der Spoel, Erik Lindahl, Berk Hess, Gerrit Groenhof, Alan E. Mark, and Herman J. C. Berendsen. Gromacs: Fast, flexible, and free. *Journal of Computational Chemistry*, 26(16):1701–1718, 2005. ISSN 1096-987X. doi: 10.1002/jcc.20291. URL http://dx.doi.org/10.1002/jcc.20291.

[212] P.J. Davis and K.M.W. Keough. Scanning calorimetric studies of aqueous dispersions of bilayers made with cholesterol and a pair of positional isomers of 3-sn-phosphatidylcholine. *Biochimica et Biophysica Acta (BBA) - Biomembranes*, 778(2):305 – 310, 1984. ISSN 0005-2736. doi: http://dx.doi.org/10.1016/0005-2736(84)90373-0. URL `http://www.sciencedirect.com/science/article/pii/0005273684903730`.

[213] Hendrik Heinz, R. A. Vaia, B. L. Farmer, and R. R. Naik. Accurate simulation of surfaces and interfaces of face-centered cubic metals using 126 and 96 lennard-jones potentials. *The Journal of Physical Chemistry C*, 112(44):17281–17290, 2008. doi: 10.1021/jp801931d. URL `http://dx.doi.org/10.1021/jp801931d`.

[214] Sung-Hee Park, Seong-Geun Oh, Ji-Young Mun, and Sung-Sik Han. Loading of gold nanoparticles inside the {DPPC} bilayers of liposome and their effects on membrane fluidities. *Colloids and Surfaces B: Biointerfaces*, 48(2):112 – 118, 2006. ISSN 0927-7765. doi: http://dx.doi.org/10.1016/j.colsurfb.2006.01.006. URL `http://www.sciencedirect.com/science/article/pii/S092777650600035X`.

[215] William J. Allen, Justin A. Lemkul, and David R. Bevan. Gridmat-md: A grid-based membrane analysis tool for use with molecular dynamics. *Journal of Computational Chemistry*, 30(12):1952–1958, 2009. ISSN 1096-987X. doi: 10.1002/jcc.21172. URL `http://dx.doi.org/10.1002/jcc.21172`.

[216] C. A. Poland, R. Duffin, I. Kinloch, A. Maynard, W. A. H. Wallace, A. Seaton, V. Stone, S. Brown, W. MacNee, and K. Donaldson. Carbon nanotubes introduced into the abdominal cavity of mice show asbestos-like pathogenicity in a pilot study. *Nat Nanotechnol*, 3(7):423–428, 2008. doi: 10.1021/nl061025k. URL `http://dx.doi.org/10.1038/nnano.2008.111`.

[217] Pilar Rivera Gil, Günter Oberdörster, Alison Elder, Víctor Puntes, and Wolfgang J. Parak. Correlating physico-chemical with toxicological properties of nanoparticles: The present and the future. *ACS Nano*, 4(10):5527–5531, 2010. doi: 10.1021/nn1025687. URL `http://dx.doi.org/10.1021/nn1025687`. PMID: 20973573.

[218] Chunbai He, Yiping Hu, Lichen Yin, Cui Tang, and Chunhua Yin. Effects of particle size and surface charge on cellular uptake and biodistribution of polymeric nanoparticles. *Biomaterials*, 31(13):3657 – 3666, 2010. ISSN 0142-9612. doi: http://dx.doi.org/10.1016/j.biomaterials.2010.01.065. URL `http://www.sciencedirect.com/science/article/pii/S0142961210000979`.

[219] Wen Jiang, KimBetty Y. S., James T. Rutka, ChanWarren C. W., and and. Nanoparticle-mediated cellular response is size-dependent. *Nat Nano*, 3:145 – 150,

2008. doi: 10.1038/nnano.2008.30. URL `http://dx.doi.org/10.1038/nnano.2008.30`.

[220] Rüdiger Goetz and Reinhard Lipowsky. Computer simulations of bilayer membranes: Self-assembly and interfacial tension. *The Journal of Chemical Physics*, 108(17): 7397–7409, 1998. URL `http://scitation.aip.org/content/aip/journal/jcp/108/17/10.1063/1.476160`.

[221] Rüdiger Goetz, Gerhard Gompper, and Reinhard Lipowsky. Mobility and elasticity of self-assembled membranes. *Phys. Rev. Lett.*, 82:221–224, Jan 1999. doi: 10.1103/PhysRevLett.82.221. URL `http://link.aps.org/doi/10.1103/PhysRevLett.82.221`.

[222] Michel Rossignol, Thierry Uso, and Pierre Thomas. Relationship between fluidity and ionic permeability of bilayers from natural mixtures of phospholipids. *The Journal of Membrane Biology*, 87(3):269–275, 1985. doi: 10.1007/BF01871227. URL `http://dx.doi.org/10.1007/BF01871227`.

[223] M B Lande, J M Donovan, and M L Zeidel. The relationship between membrane fluidity and permeabilities to water, solutes, ammonia, and protons. *The Journal of General Physiology*, 106(1):67–84, 1995. URL `http://jgp.rupress.org/content/106/1/67.abstract`.

[224] Toshinori Shimanouchi, Haruyuki Ishii, Noriko Yoshimoto, Hiroshi Umakoshi, and Ryoichi Kuboi. Calcein permeation across phosphatidylcholine bilayer membrane: Effects of membrane fluidity, liposome size, and immobilization. *Colloids and Surfaces B: Biointerfaces*, 73(1):156 – 160, 2009. ISSN 0927-7765. doi: http://dx.doi.org/10.1016/j.colsurfb.2009.05.014. URL `http://www.sciencedirect.com/science/article/pii/S0927776509001982`.

[225] O Bakouche, D Gerlier, J M Letoffe, and P Claudy. Phase separation of miscible phospholipids by sonication of bilayer vesicles. *Biophysical Journal*, 50(1):1–4, 07 1986. URL `http://www.ncbi.nlm.nih.gov/pmc/articles/PMC1329652/`.

[226] J. J. López Cascales, T. F. Otero, A. J. Fernández Romero, and L. Camacho. Phase transition of a dppc bilayer induced by an external surface pressure: from bilayer to monolayer behavior. a molecular dynamics simulation study. *Langmuir*, 22(13): 5818–5824, 2006. doi: 10.1021/la0602315. URL `http://dx.doi.org/10.1021/la0602315`. PMID: 16768513.

[227] Andrzej J. Rzepiela, Lars V. Schäfer, Nicolae Goga, H. Jelger Risselada, Alex H. De Vries, and Siewert J. Marrink. Reconstruction of atomistic details from coarse-grained structures. *Journal of Computational Chemistry*, 31(6):1333–1343, 2010.

ISSN 1096-987X. doi: 10.1002/jcc.21415. URL `http://dx.doi.org/10.1002/jcc.21415`.

[228] Indira Chandrasekhar, Mika Kastenholz, RobertoD. Lins, Chris Oostenbrink, LukasD. Schuler, D.Peter Tieleman, and WilfredF. van Gunsteren. A consistent potential energy parameter set for lipids: dipalmitoylphosphatidylcholine as a benchmark of the gromos96 45a3 force field. *European Biophysics Journal*, 32 (1):67–77, 2003. ISSN 0175-7571. doi: 10.1007/s00249-002-0269-4. URL `http://dx.doi.org/10.1007/s00249-002-0269-4`.

[229] David Poger, Wilfred F. Van Gunsteren, and Alan E. Mark. A new force field for simulating phosphatidylcholine bilayers. *Journal of Computational Chemistry*, 31(6):1117–1125, 2010. ISSN 1096-987X. doi: 10.1002/jcc.21396. URL `http://dx.doi.org/10.1002/jcc.21396`.

[230] Ling Miao and Jorge M. Seminario. Molecular dynamics simulations of the vibrational signature transfer from a glycine peptide chain to nanosized gold clusters. *The Journal of Physical Chemistry C*, 111(23):8366–8371, 2007. doi: 10.1021/jp068797p. URL `http://dx.doi.org/10.1021/jp068797p`.

[231] Joseph Hautman and Michael L. Klein. Simulation of a monolayer of alkyl thiol chains. *The Journal of Chemical Physics*, 91(8):4994–5001, 1989. URL `http://scitation.aip.org/content/aip/journal/jcp/91/8/10.1063/1.457621`.

[232] Lou Strong and George M. Whitesides. Structures of self-assembled monolayer films of organosulfur compounds adsorbed on gold single crystals: electron diffraction studies. *Langmuir*, 4(3):546–558, 1988. doi: 10.1021/la00081a009. URL `http://dx.doi.org/10.1021/la00081a009`.

[233] Wen Mar and Michael L. Klein. Molecular dynamics study of the self-assembled monolayer composed of s(ch2)14ch3 molecules using an all-atoms model. *Langmuir*, 10(1):188–196, 1994. doi: 10.1021/la00013a028. URL `http://dx.doi.org/10.1021/la00013a028`.

[234] Jaspreet K. Vasir and Vinod Labhasetwar. Quantification of the force of nanoparticle-cell membrane interactions and its influence on intracellular trafficking of nanoparticles. *Biomaterials*, 29:4244 – 4252, 2008. ISSN 0142-9612. doi: http://dx.doi.org/10.1016/j.biomaterials.2008.07.020. URL `http://www.sciencedirect.com/science/article/pii/S0142961208004791`.

[235] Robert Vcha, Francisco J. Martinez-Veracoechea, and Daan Frenkel. Receptor-mediated endocytosis of nanoparticles of various shapes. *Nano Letters*, 11(12):

5391–5395, 2011. doi: 10.1021/nl2030213. URL `http://dx.doi.org/10.1021/nl2030213`. PMID: 22047641.

[236] Hiroshi Noguchi and Masako Takasu. Adhesion of nanoparticles to vesicles: A brownian dynamics simulation. *Biophysical Journal*, 83(1):299 – 308, 2002. ISSN 0006-3495. doi: http://dx.doi.org/10.1016/S0006-3495(02)75170-9. URL `http://www.sciencedirect.com/science/article/pii/S0006349502751709`.

[237] Benedict J. Reynwar, Gregoria Illya, Vagelis A. Harmandaris, Martin M. Muller, Kurt Kremer, and Markus Deserno. Aggregation and vesiculation of membrane proteins by curvature-mediated interactions. *Nature*, 447:461–464, 2007. ISSN 7143. doi: 10.1038/nature05840. URL `http://dx.doi.org/10.1038/nature05840`.

[238] Matthias Schulz, Adekunle Olubummo, and Wolfgang H. Binder. Beyond the lipid-bilayer: interaction of polymers and nanoparticles with membranes. *Soft Matter*, 8:4849–4864, 2012.

[239] P.-L. CHAU and A. J. HARDWICK. A new order parameter for tetrahedral configurations. *Molecular Physics*, 93(3):511–518, 1998. doi: 10.1080/002689798169195. URL `http://dx.doi.org/10.1080/002689798169195`.

[240] D.P Tieleman, S.J Marrink, and H.J.C Berendsen. A computer perspective of membranes: molecular dynamics studies of lipid bilayer systems. *Biochimica et Biophysica Acta (BBA) - Reviews on Biomembranes*, 1331(3):235 – 270, 1997. ISSN 0304-4157. doi: http://dx.doi.org/10.1016/S0304-4157(97)00008-7. URL `http://www.sciencedirect.com/science/article/pii/S0304415797000087`.

[241] Hung W.C., Lee M.T., Chen F.Y., and Huang H.W. The condensing effect of cholesterol in lipid bilayers. *Biophysical Journal*, 92:3960–3967, 2007.

[242] Ipsen J.H., Mouritsen O.G., and Bloom M. Relationships between lipid membrane area, hydrophobic thickness, and acyl-chain orientational order. the effects of cholesterol. *Biophysical Journal*, 57:405–412, 1990.

[243] William J. Allen, Justin A. Lemkul, and David R. Bevan. Gridmat-md: A grid-based membrane analysis tool for use with molecular dynamics. *Journal of Computational Chemistry*, 30(12):1952–1958, 2009. ISSN 1096-987X. doi: 10.1002/jcc.21172. URL `http://dx.doi.org/10.1002/jcc.21172`.

[244] Ralf P. Richter, Rémi Bérat, and Alain R. Brisson. Formation of solid-supported lipid bilayers: an integrated view. *Langmuir*, 22(8):3497–3505, 2006. doi: 10.1021/la052687c. URL `http://dx.doi.org/10.1021/la052687c`. PMID: 16584220.

[245] Chenyue Xing and Roland Faller. Interactions of lipid bilayers with supports: A coarse-grained molecular simulation study. *The Journal of Physical Chemistry B*, 112(23):7086–7094, 2008. doi: 10.1021/jp077305l. URL `http://dx.doi.org/10.1021/jp077305l`. PMID: 18461982.

[246] TaeWoon Cha, Athena Guo, and X.-Y. Zhu. Formation of supported phospholipid bilayers on molecular surfaces: Role of surface charge density and electrostatic interaction. *Biophysical Journal*, 90(4):1270 – 1274, 2006. ISSN 0006-3495. doi: http://dx.doi.org/10.1529/biophysj.105.061432. URL `http://www.sciencedirect.com/science/article/pii/S0006349506723189`.

[247] Xubo Lin, Changling Wang, Meng Wang, Kun Fang, and Ning Gu. Computer simulation of the effects of nanoparticles' adsorption on the properties of supported lipid bilayer. *The Journal of Physical Chemistry C*, 116(33):17960–17968, 2012. doi: 10.1021/jp305784z. URL `http://dx.doi.org/10.1021/jp305784z`.

[248] Hwankyu Lee and Hyungsu Kim. Self-assembly of lipids and single-walled carbon nanotubes: Effects of lipid structure and pegylation. *The Journal of Physical Chemistry C*, 116(16):9327–9333, 2012. doi: 10.1021/jp3010663. URL `http://dx.doi.org/10.1021/jp3010663`.

[249] Matthew A. Cooper, Andrew C. Try, Joe Carroll, David J. Ellar, and Dudley H. Williams. Surface plasmon resonance analysis at a supported lipid monolayer. *Biochimica et Biophysica Acta (BBA) - Biomembranes*, 1373(1):101 – 111, 1998. ISSN 0005-2736. doi: http://dx.doi.org/10.1016/S0005-2736(98)00091-1. URL `http://www.sciencedirect.com/science/article/pii/S0005273698000911`.

[250] Peter Lenz, Caroline M. Ajo-Franklin, , and Steven G. Boxer. Patterned supported lipid bilayers and monolayers on poly-dimethylsiloxane. *Langmuir*, 20(25): 11092–11099, 2004. doi: 10.1021/la048450i. URL `http://dx.doi.org/10.1021/la048450i`.

[251] Jin-Won Park and Gil U. Lee. Properties of mixed lipid monolayers assembled on hydrophobic surfaces through vesicle adsorption. *Langmuir*, 22(11):5057–5063, 05 2006. doi: 10.1021/la060688e. URL `http://dx.doi.org/10.1021/la060688e`.

[252] Tammy E. Starr, , and Nancy L. Thompson. Formation and characterization of planar phospholipid bilayers supported on tio2 and srtio3 single crystals. *Langmuir*, 16(26):10301–10308, 2000. doi: 10.1021/la000992m. URL `http://dx.doi.org/10.1021/la000992m`.

[253] Erik Reimhult, Fredrik Hook, and Bengt Kasemo. Vesicle adsorption on sio2 and tio2: Dependence on vesicle size. *The Journal of Chemical Physics*, 117(16): 7401–7404, 2002. doi: http://dx.doi.org/10.1063/1.1515320.

[254] Erik Reimhult, Fredrik Hook, and Bengt Kasemo. Intact vesicle adsorption and supported biomembrane formation from vesicles in solution: influence of surface chemistry, vesicle size, temperature, and osmotic pressure, 2003. URL `http://dx.doi.org/10.1021/la0263920`.

[255] Yang Li and Ning Gu. Thermodynamics of charged nanoparticle adsorption on charge-neutral membranes: A simulation study. *The Journal of Physical Chemistry B*, 114(8):2749–2754, 2010. doi: 10.1021/jp904550b. URL `http://dx.doi.org/10.1021/jp904550b`. PMID: 20146444.

[256] Mehrnaz Shaali, Samuel Lara-Avila, Paul Dommersnes, Alar Ainla, Sergey Kubatkin, and Aldo Jesorka. Nanopatterning of mobile lipid monolayers on electron-beam-sculpted teflon af surfaces. *ACS Nano*, 9(2):1271–1279, 02 2015. doi: 10.1021/nn5050867. URL `http://dx.doi.org/10.1021/nn5050867`.

[257] Babak Sanii and Atul N. Parikh. Surface-energy dependent spreading of lipid monolayers and bilayers. *Soft Matter*, 3:974–977, 2007. doi: 10.1039/B704827K. URL `http://dx.doi.org/10.1039/B704827K`.

[258] John T. Elliott, Daniel L. Burden, John T. Woodward, Amit Sehgal, and Jack F. Douglas. Phospholipid monolayers supported on spun cast polystyrene films. *Langmuir*, 19(6):2275–2283, 03 2003. doi: 10.1021/la0260640. URL `http://dx.doi.org/10.1021/la0260640`.

[259] Steffen Lingler, Israel Rubinstein, Wolfgang Knoll, and Andreas Offenhäusser. Fusion of small unilamellar lipid vesicles to alkanethiol and thiolipid self-assembled monolayers on gold. *Langmuir*, 13(26):7085–7091, 12 1997. doi: 10.1021/la970600k. URL `http://dx.doi.org/10.1021/la970600k`.

[260] Sandra V. Bennun, Allison N. Dickey, Chenyue Xing, and Roland Faller. Simulations of biomembranes and water: Important technical aspects. *Fluid Phase Equilibria*, 261(1–2):18 – 25, 2007. ISSN 0378-3812. doi: http://dx.doi.org/10.1016/j.fluid.2007.07.056. URL `http://www.sciencedirect.com/science/article/pii/S0378381207004414`. Properties and Phase Equilibria for Product and Process Design 11th International Conference on Properties and Phase Equilibria for Product and Process Design.

[261] Antti Lamberg and Takashi Taniguchi. Coarse-grained computational studies of supported bilayers: Current problems and their root causes. *The Journal of*

Physical Chemistry B, 118(36):10643–10652, 2014. doi: 10.1021/jp5053419. URL `http://dx.doi.org/10.1021/jp5053419`.

[262] Pradeep Kumar, Sergey V. Buldyrev, Francis W. Starr, Nicolas Giovambattista, and H. Eugene Stanley. Thermodynamics, structure, and dynamics of water confined between hydrophobic plates. *Phys. Rev. E*, 72:051503–051514, Nov 2005. doi: 10.1103/PhysRevE.72.051503. URL `http://link.aps.org/doi/10.1103/PhysRevE.72.051503`.

[263] Magdalena Przybylo, Jan Sýkora, Jana Humpolíčková, Aleš Benda, Anna Zan, and Martin Hof. Lipid diffusion in giant unilamellar vesicles is more than 2 times faster than in supported phospholipid bilayers under identical conditions. *Langmuir*, 22(22):9096–9099, 2006. doi: 10.1021/la061934p. URL `http://dx.doi.org/10.1021/la061934p`. PMID: 17042516.

[264] James R. Sheats and Harden M. McConnell. A photochemical technique for measuring lateral diffusion of spin-labeled phospholipids in membranes. *Proceedings of the National Academy of Sciences*, 75(10):4661–4663, 1978. URL `http://www.pnas.org/content/75/10/4661.abstract`.

[265] An Li Kuo and Charles G. Wade. Lipid lateral diffusion by pulsed nuclear magnetic resonance. *Biochemistry*, 18(11):2300–2308, 1979. doi: 10.1021/bi00578a026. URL `http://dx.doi.org/10.1021/bi00578a026`.

[266] Nicolas D. Winter and George C. Schatz. Coarse-grained molecular dynamics study of permeability enhancement in dppc bilayers by incorporation of lysolipid. *The Journal of Physical Chemistry B*, 114(15):5053–5060, 2010. doi: 10.1021/jp911309s. URL `http://dx.doi.org/10.1021/jp911309s`.